Doctoral Dissertation
Doctoral Program in Energy Engineering (36^{th}cycle)

Monte Carlo modeling and variance reduction technique applications for heavily shielded geometries in the decommissioning of nuclear power plants

By

Simone Bleynat

******

Supervisor(s):
Prof. S. Dulla
Prof. R. Zanino

Doctoral Examination Committee:
Dr. P. Cosgrove , Referee, University of Cambridge
Prof. L. Snoj, Referee, Jozef Stefan Institute
Prof. D. Mostacci, Referee, University of Bologna
Dr. C. Rusconi, Referee, Sogin S.p.A

Politecnico di Torino
2024

Declaration

I hereby declare that, the contents and organization of this dissertation constitute my own original work and does not compromise in any way the rights of third parties, including those related to the security of personal data.

Simone Bleynat
2024

* This dissertation is presented in partial fulfillment of the requirements for **Ph.D. degree** in the Graduate School of Politecnico di Torino (ScuDo).

"I would like to dedicate this work to my dad, whose spirit will always be with me"

Acknowledgements

I would like to acknowledge the support provided by Sogin SpA, specially for what concerns data selection and management. More in detail, I would like to thank Federica Pancotti, my company supervisor at the beginning of the project, Luca Ricci, who shared extremely valuable insights on the calculation setup and Carlo Vicini who supported and coordinated the project on the company side.

Abstract

An in-depth study is presented addressing the challenges associated with the residual activation in nuclear power plants, specifically focusing on their decommissioning processes in scenarios characterized by heavily shielded geometries, exemplified by the reactor pressure vessel of a pressurized water reactor.

More in detail, the main topic is the development of a 3D calculation scheme for the evaluation of the residual activation generated by neutron interactions within the structural material of the vessel and internal components of a pressurized water reactor. The focus of the scheme is primarily the analysis of the Enrico Fermi nuclear power plant in Trino, Italy, which is currently undergoing decommissioning.

The scheme is initially developed to analyze the thermal shield of the reactor, and benefits from measurement campaigns conducted in 1969 and 1992: these campaigns provide crucial data for scheme validation, enabling testing across the shield and for various isotopes, with a focus on key isotopes such as ^{60}Co, ^{59}Ni, and ^{63}Ni, significant in waste classification and as powerful gamma emitters. The scheme exhibits robust performance, offering accurate estimates of the residual activation of the thermal shield.

The scheme is later expanded to analyse the vessel's internal liner, considering that the vessel itself is usually the largest and most complex component to dismantle and the internal stainless steel liner is quite prone to activation. In order to do so, a few modifications are introduced and the scheme is applied a second time to perform a detailed analysis of the irradiation history of several points at different heights and angular coordinates along the entire life of the reactor. It became clear after a few preliminary calculations that most of the vessel exhibits a uniform angular distribution of the neutron flux, therefore many regions can be treated as uniformly irradiated. The scheme envisions the analysis of four different core configurations representing the entire operating life of the reactor and the modifications introduced

both in terms of geometry and in terms of power produced. Two separate sets of measurements are used to validate the scheme results, the first one coming from the analysis of a liner sample and the second coming from a set of dosimeters used in the framework of the vessel surveillance program. The scheme performs well, and is able to correctly assess the residual activation in many different points along the vessel liner and in agreement with the measurements. It also proves flexible enough to consider different combinations of materials, irradiation history, spectra and geometric position.

The scheme undergoes then a final modification to test the Representative Operating Cycle (ROC) hypothesis. This hypothesis, suggested for the analysis of nuclear reactors with relatively constant operation and geometry, is assessed for its applicability to the Trino reactor. The ROC approach shows promising results, yielding a slightly conservative estimate of residual activations and contact dose rates compared to the hybrid model, validating its suitability for a reactor characterised by a rather complex history. This approach is particularly convenient in decommissioning studies, considering its simplified implementation and reduced computational cost.

Considering that activation calculations are just the initial step of the complex process required for a successful decommissioning project, with the actual dismantling coming afterwards, an additional contribution to the engineering studies is carried out in collaboration with the Department of Mechanical and Aerospace Engineering (DIMEAS). The aim of this contribution is to provide a more complete overview of the issue of nuclear decommissioning and offer insights on the multidisciplinary nature of the process. The topic addressed is the development of a methodology designed for selecting the optimal cutting technique for the decommissioning of a nuclear power plant, as this is one of the most difficult choices the stakeholders involved in the process have to make. Tailored to align with site-specific requirements inherent in diverse decommissioning projects, this methodology addresses challenges associated with dismantling such complex facilities.

Contents

List of Figures

List of Tables

Chapter 1

Introduction

1.1 The role of nuclear energy in the world energy mix

Nuclear energy stands as a significant contributor to the global low-carbon energy landscape, accounting for approximately 9% of the worldwide electricity supply: it is currently the second-largest source of carbon-free power, second only to hydropower, which fulfills approximately 15% of the world's electricity needs [1]. In contrast to hydropower, nuclear energy exhibits more scalability and an independence from specific geographical terrains; this distinctive attribute grants significant potential for addressing growing energy demands, while concurrently minimizing adverse environmental repercussions, encompassing both carbon dioxide (CO_2) emissions and land utilization. Such characteristics are particularly important for industrialized nations with aspirations of mitigating their carbon footprint, while safeguarding economic growth and ensuring the continuity of baseload electricity production, which is presently dominated by fossil fuel combustion.

It is noteworthy that all seven of the world's most advanced economies, collectively represented as the G7 (comprising the United States, France, Canada, the United Kingdom, Japan, Germany, and Italy), have either operated or presently operate nuclear power facilities. In the United States, the major G7 economy, the existing configuration comprises 93 nuclear reactors—the highest number within a single nation—constituting nearly a quarter of the global nuclear reactor population. Meanwhile, France stands as the most notable example in terms of nuclear energy integration within its electricity mix, with the nuclear source generating approximately 70% of its electricity. France's nuclear fleet comprises 56 reactors, an impressive ratio of nearly one reactor per million inhabitants. Consequently, owing to its substantial nuclear energy production, France further distinguishes itself by exporting surplus electricity to neighboring nations. Canada, the United Kingdom and Japan operate 19, 9, and 10 reactors, respectively. Japan, prior to the catastrophic Fukushima-Daiichi nuclear power plant incident in 2011, relied upon nuclear energy to provide approximately 30% of its electricity requisites. Subsequently, the government mandated a complete stop of reactor operation, although with subsequent reactivation of selected facilities following rigorous safety inspections and enhancements. Presently, the proportion of nuclear energy within Japan's electricity composition approximates a modest 6%.

In contrast to their G7 counterparts, Germany and Italy have embarked upon different trajectories regarding nuclear power. Germany maintained a limited number of operational reactors, but ordered the closure of its last nuclear plants in April 2023. This decision was underpinned by Germany's longstanding commitment to the Energiewende, a comprehensive energy policy with the ambitious goal of sourcing 100% of the nation's electricity from renewable resources encompassing solar, wind, and hydropower. This trajectory gained momentum following the Fukushima-Daiichi accident. Conversely, Italy's stance on nuclear energy has predated the actions of Germany by several decades. Italy, in 1987, decided to discontinue nuclear energy production, after a national referendum held in the aftermath of the Chernobyl disaster. Public apprehensions and disfavorable perceptions of nuclear power, exacerbated by fears of radioactive contamination, prompted the population to advocate for the immediate end of nuclear energy production. More details on the Italian framework will be presented in Section 1.6.

The present-day global landscape of nuclear power is characterized by the operation of 413 nuclear power reactors. However, it is necessary to highlight that a substantial proportion of these installations, approximately 65%, was built before 1990 [2]. Currently, roughly 200 reactors have been permanently shut down, and a significant challenge looms as a large number of reactors approach the culmination of their prescribed operational lifespan within the forthcoming decades. While some reactors have undergone or are currently undergoing refurbishment projects aimed at extending their operational longevity, a practice denoted as Long Term Operation

(LTO), it is important to recognize that not all nuclear facilities possess the necessary attributes to make them eligible for such a procedure. Consequently, a considerable cohort of reactors will face end of operations and subsequent decommissioning. Notably, this scenario foresees an increase in decommissioning activities, particularly in those nations that ventured early into the nuclear industry and are currently reliant upon aging reactor infrastructure. Concomitant with the expansion of decommissioning obligations is the growth in the generation of radioactive waste, necessitating the adoption of well-planned strategies for their appropriate disposal. Abiding to the local regulations governing the management of radioactive waste is of paramount significance, thereby mandating the construction of designated disposal facilities, whether situated on the surface or underground depending on the kind of waste to be disposed of.

1.2 Main reactor design

The landscape of nuclear reactors across the globe predominantly comprises Light Water Reactors (LWRs), where conventional water serves dual roles as both a coolant and moderator [2].

Within this classification, Pressurized Water Reactors (PWRs) are the most prevalent design [3], [4], and necessitate adequate consideration during the decommissioning process, primarily due to the substantial effort required for the disassembly of large components within the primary cooling circuit and the reactor core. These components encompass the Reactor Pressure Vessel (RPV), Reactor Vessel Internals (RVIs), bioshield, steam generators, pumps, pressurizer, and circuit pipes. One of the primary concern in this context is the potential radioactive contamination, which can affect most of the mentioned components. Structural material activation, conversely, remains a phenomenon exclusive to the RPV, RVIs, and the concrete bioshield around the core. The activation process occurs only in the presence of an intense neutron flux, with its effects diminishing as distance increases from the reactor core. Consequently, the dismantling of the RPV, RVIs, and bioshield constitutes a particularly challenging activity, driven by a confluence of factors, in particular the nature of thick steel and concrete structures and the hazardous radioactive environments that frequently require the utilization of remote technologies. Additionally, the limited space within these environments, exemplified by the reactor pit, highlights the complexity of decommissioning efforts.

Boiling Water Reactors (BWRs), similar in many ways to PWRs in terms of materials and design, exhibit certain distinctions, notably a larger RPV, attributable to a lower power density and operating pressure. BWRs additionally feature steam separators, steam dryers, and recirculation pumps among other internal components, which are absent in PWRs. The upper regions of BWRs, owing to the reactor's substantial size, remain less susceptible to activation phenomena, although contamination is a plausible concern. Significantly, BWRs differ fundamentally from PWRs in that the steam generator is an integral component of the reactor itself, eliminating the need for an external primary circuit [5], [4].

Pressurized Heavy Water Reactors (PHWRs) introduce a distinct paradigm by employing heavy water as both neutron moderator and coolant, in contrast with LWRs that are moderated and cooled by light water. The lower neutron absorption properties of heavy water allows the possibility of operating the reactor with natural uranium, in contrast to enriched uranium. The PHWR design diverges substantially from LWRs, with the widely adopted CANadian Deuterium Uranium (CANDU) configuration notably lacking a pressure vessel. Fuel bundles are instead inserted into pressure tubes, which, within the reactor core, are contained within a much larger (but not pressurized) vessel filled with heavy water. This design choice stemmed from the technological constraints of the Canadian heavy industry during the 1950s and 1960s, when design was ongoing and the forging of large pressure vessels presented significant challenges [6], [4].

Gas Cooled Reactors (GCRs) stand apart from water reactors in terms of their operational principles. While they saw deployment during the initial stages of commercial nuclear power development, LWRs ultimately became dominant within the industry, relegating GCRs to relative unimportance, with the majority of remaining GCRs located in the United Kingdom. GCRs employ gases such as helium or CO_2 for cooling and rely on graphite as a moderator. Due to their lower energy density, GCR vessels tend to be voluminous, similarly to BWRs [7], [4]. In addition, graphite exhibits significant activation when exposed to intense neutron flux, characteristic of the reactor core environment. Consequently, the decommissioning of GCRs presents significant challenges, mainly due to concerns surrounding activated graphite. This challenge is shared with graphite-moderated, water-cooled reactors (RBMKs), a design that underwent progressive phasing out in the aftermath of the Chernobyl disaster.

The early stages of the nuclear industry's development witnessed the emergence and deployment of several reactor designs. This initial period, characterized by a lack of standardization concerning geometrical configurations and materials, created a situation where aging nuclear facilities assumed distinctive attributes. These characteristics encompass atypical structural features, unconventional layouts and operational histories, or, in some instances, a confluence of these factors. Consequently, the decommissioning of such old plants can prove to be a challenging undertaking, and the necessity of developing a comprehensive decommissioning strategy is profoundly influenced by these aspects. It follows that a thorough evaluation of each reactor's characteristics is a prerequisite to commencing the dismantling process. Despite the complications posed by the diverse technical challenges, the global nuclear decommissioning sector stands at the threshold of notable expansion. Projections indicate the allocation of substantial financial resources, amounting to several hundred billion dollars, across the international landscape between the present day and the year 2050 [8]. This anticipated growth is also influenced by strategic political determinations that advocate for the gradual phase-out of nuclear power. This transition is particularly evident in nations such as Germany, Switzerland, and Italy, where policy decisions impacted the future trajectory of this sector.

1.3 Dominant activation mechanisms in nuclear fission reactors

In the context of a nuclear reactor, it is important to acknowledge that not all neutrons engage in interactions with fissile materials that result in fission events and the consequential production of energy. The neutron-matter interactions include various types, encompassing elastic scattering - a process where kinetic energy remains conserved during a collision - inelastic scattering, which deviates from energy conservation during a collision - and radiative capture, characterized by the assimilation of a neutron by a nucleus, subsequently leading to the emission of gamma rays. The probability of such interactions, quantified as cross sections, exhibits a pronounced dependence on the energy of the incident neutron. Furthermore, there are many other possible interactions, including neutron-α (n,α), neutron-induced two-neutron emission (n,2n), neutron-proton (n,p), and neutron-deuteron (n,d) reactions. However, in the framework of activation phenomena in nuclear reactors, these interactions tend to be relatively rare, requiring the presence of high-energy neutrons for their appearance. Most fission reactions occur in the thermal energy range, where fission cross sections reach greater magnitudes. Consequently, thermal nuclear reactors are engineered systems aimed at decreasing the energy of high-energy neutrons, primarily through the phenomenon of elastic scattering with hydrogen atoms. The thermal energy range assumes significance in the framework of activation phenomena as well, largely due to the notable population of thermalized neutrons and the higher cross sections characterizing neutron-matter interactions within this energy range. Cross sections within the thermal region of the energy spectrum typically surpass those associated with interactions involving high-energy neutrons by several orders of magnitude. As an example, cross sections governing the interactions of fast neutrons with matter generally assume values on the order of few millibarns, while, conversely, the radiative capture cross section of thermal neutrons' interaction with ^{54}Fe, the most common isotope in structural steels, reaches values up to the order of 1-10 barns. Such disparities highlight the role played by interactions within the thermal range as a primary source of residual activity [9].

The phenomenon of radiative capture in structural materials often results in the formation of unstable, and consequently radioactive, nuclei. This process of transmutation is the fundamental mechanism underlying the activation of structural materials. While the configuration of the reactor core and the disposition of fuel elements have influence over neutron leakage rates from the system, it is necessary to acknowledge that complete elimination of neutron leakage is unattainable. As such, a certain proportion of neutrons will inevitably escape from the reactor core. In response to this challenge, low-leakage loading patterns have been developed over the past several decades. These patterns have been devised with two primary objectives in mind: firstly, to enhance the neutron economy of the core, thereby increasing the availability of neutrons for fission reactions or plutonium production, and secondly, to mitigate the activation phenomena and radiation damage occurring within the surrounding structural components. This latter phenomenon is relevant specially for the RPV, as it impacts the component's lifetime. Of particular significance within the group of structural materials are stable isotopes that exhibit a predisposition to transform into radioactive isotopes after exposure to a neutron flux, usually known as *precursors*, such as ^{58}Ni or ^{62}Ni. The resultant radioactive isotopes may be significant in waste classification or present concerns due to the substantial gamma radiation fields they generate.

1.4 Relevant materials in decommissioning activities and most relevant isotopes

Within nuclear power plants, the main supporting structures predominantly consist of carbon steel, stainless steel, or concrete. Apart from the fuel itself and potential coolants, the only additional material that significantly presents activation concerns —although without serving a structural role — is graphite. As previously mentioned, graphite is employed within GCRs as a neutron moderator. While steels share some similarities in terms of the potential radioisotopes generation due to their elemental composition, the considerable diversity among possible alloys results in varying degrees of susceptibility to activation. Typically, stainless steels exhibit a higher predisposition to activation as compared to carbon steels. Concrete and graphite, on the other hand, possess different compositions, both when compared to each other and when compared with steels. Consequently, they yield a different spectrum of activation products, although with partial overlap with those characterizing steel materials. In a broader context, many of these materials suffer the presence of impurities, i.e. trace amounts of stable nuclei that tend to undergo activation with exceptional ease, such as ^{59}Co, which easily transmutes into the radioactive ^{60}Co, frequently exerting a significant influence on the material's behavior when exposed to irradiation.

The careful management of impurities within structural materials constitutes a principal focus of the contemporary nuclear industry. Presently, there is an effort to advance the development of reduced activation materials, strategically designed to reduce the challenges associated with the eventual decommissioning of future nuclear facilities, either based on fission or fusion reactions. A noteworthy example of such materials is *EUROFER*, an alloy of steel that has been formulated within the context of fusion reactor development, in projects such as the International Thermonuclear Experimental Reactor (ITER) [10]. *EUROFER* distinguishes itself through its enhanced resilience to radiation-induced damage and a greater attention towards impurity regulation. The latter attribute, in particular, increases its resistance to neutron activation phenomena [11], [12]. Sections 1.4.1, 1.4.2 and 1.4.3 list a set of nuclides relevant in decommissioning activities due to a combination of different parameters, such as:

- Abundance of their precursors, in significant amounts or as impurities, in structural material widely used in NPPs construction, such as steels or concrete;
- Abundance of their precursors, in significant amounts or as impurities, in other types of material used in NPPs, such as graphite or the Ag-In-Cd alloy often used for control rods;
- Gamma rays generation rate and corresponding intensity, required for shielding design during dismantling operations;
- Impact of long term activation;
- Relevance in waste characterization according to the Italian regulation;
- Amount expected during dismantling operations.

1.4.1 Main activated nuclides in steels

The main nuclides causing the long-term activation of steels encompass the following: ^{60}Co, ^{59}Ni, ^{63}Ni, ^{14}C, ^{55}Fe, ^{93}Mo, ^{94}Nb, ^{99}Tc, and ^{108m}Ag. During irradiation, a few additional isotopes may be generated, including ^{51}Cr, ^{54}Mn, ^{59}Fe, and ^{58}Co. These latter isotopes exhibit relatively short half-lives, ranging from a few dozen to few hundred days. Given the long and articulated nature of decommissioning procedures, typically taking place at the earliest some years following reactor shutdown, these isotopes are generally deemed of lesser significance. Their short half-lives, indeed, result in a fast decline in their contribution to the overall residual activity of the material. In the subsequent Section 1.4.1, a brief description of the long-lived isotopes is thus provided [9]. The cross section values reported in the following sections are taken from [13] and [14].

Cobalt-60

Among the activation products, ^{60}Co stands out as one of the most important. Its primary production occurs predominantly through radiative neutron capture — both thermal and epithermal — of ^{59}Co, the only stable cobalt isotope in nature. While alternative pathways for ^{60}Co production, such as (n,p) reactions with ^{60}Ni, do exist, their significance remains lower. This disparity in significance arises from the relative abundance of ^{59}Co as an impurity in steel and the considerable neutron capture cross section of this isotope, which, at 0.025 eV, attains approximately 37 barns.

The decay process of ^{60}Co involves the emission of a medium-energy electron (0.32 MeV), as it transforms into ^{60}Ni. However, the daughter nucleus resides in an excited state, subsequently transitioning to its ground state through the emission of gamma rays of 1.173 and 1.332 MeV. The decay of ^{60}Co, thus, generates a strong gamma radiation field, a factor of great significance in dismantling operations. Moreover, the intermediate half-life of this radioisotope, standing at 5.27 years, designates it as the main contributor to the dose rate within the time span encompassing a few decades post-shutdown, precisely when most decommissioning activities usually occur. The main concern pertaining to steels revolves around the concentration of trace cobalt, which exhibits unexpected variability. An analysis of stainless-steel samples sourced from multiple U.S. nuclear reactors, for instance, unveiled a fluctuation spanning an order of magnitude, with the mean concentration being sevenfold higher than the lowest recorded value [9]. This variance can be attributed to the limited impact of cobalt impurities on the structural characteristics of the material. Indeed, the industry implementation of impurity control to reduce trace cobalt content only occurred with a deeper comprehension of its role in residual activation. In contrast, carbon steels typically manifest lower trace cobalt content and exhibit reduced variability. The presence of cobalt in steels is likely more closely associated with the origin of the utilized ore body rather than specific manufacturing procedures.

Nickel-59 and Nickel-63

Naturally occurring nickel is formed by five stable isotopes: ^{58}Ni, ^{60}Ni, ^{61}Ni, ^{62}Ni, and ^{64}Ni. Among these, ^{58}Ni stands as the most prevalent, constituting approximately 68% of natural nickel content. Following closely is ^{60}Ni, representing approximately

26%, while ^{62}Ni accounts for roughly 3.6% of the elemental composition, while the residual isotopes collectively contribute to the remaining part. ^{59}Ni is generated by thermal neutron capture from ^{58}Ni, which shows a moderately high capture cross section of 4.2 barns at 0.025 eV, and it assumes significance in decommissioning due to the substantial nickel content within stainless steel and the abundance of its precursor isotope. ^{59}Ni exclusively decays by electron capture; these decays are accompanied by the emission of low-energy X-rays, with the bulk of the transition energy carried away by a neutrino. Notably, ^{59}Ni exhibits a considerably high transition energy of 1.07 MeV relative to its half-life. In a minority of decays, the transition energy is divided between a neutrino and a gamma ray—a phenomenon recognized as inner bremsstrahlung. While typically a minor branch, this implies that ^{59}Ni produces a continuous spectrum of gamma rays, some with energies reaching up to 1.07 MeV in approximately one out of every thousand decays. Given this gamma emission characteristic and the substantial prevalence of this isotope within various regions of the reactor, careful consideration is required for dose limitations, particularly after the decay of stronger gamma emitters like ^{60}Co, as ^{59}Ni has a half-life of approximately 80000 years.

^{63}Ni is the other prominent concern in nickel activation. With a half-life of approximately 100 years, ^{63}Ni ranks among the most abundant activation products within the timeframe typical of deferred decommissioning. Its genesis stems from thermal neutron capture by the relatively scarce ^{62}Ni, featuring a cross section of 14.9 barns at 0.025 eV. While its cross section is moderate and its relative abundance within nickel alloys is limited, this is somehow offset by the substantial quantity of nickel present in numerous nuclear-grade alloys. The decay process of ^{63}Ni involves the emission of a 66 keV electron, rendering bremsstrahlung radiation negligible for this isotope. The reactor internals, constructed primarily from stainless steel and situated in close proximity to the neutron source, experience significant neutron activation. A considerable portion of the long-term residual activation can be attributed to ^{59}Ni, due to its long half-life, therefore components rich in nickel necessitate disposal within geological formations. This same concern extends to the internal liner of the reactor pressure vessel, necessitating meticulous consideration during the planning of dismantling procedures.

Iron-55

^{55}Fe is primarily generated by thermal neutron capture from ^{54}Fe, which constitutes approximately 5.85% of natural iron. The reaction cross section is approximately 2.25 barns at 0.025 eV. An alternative, although minor, production mechanism involves (n,2n) reactions on ^{56}Fe, the most abundant naturally occurring iron isotope, which forms 91.8% of iron. Virtually all ^{55}Fe generated through activation in a reactor results from neutron capture, as the (n,2n) reactions necessitate substantially higher neutron energies, typically beyond the attainable range with fission, with a threshold energy of approximately 11 MeV. The decay process of ^{55}Fe, with a half-life of 2.74 years, is electron capture, which leads to the formation of ^{55}Mn. This transmutation is accompanied by the emission of 5.9 keV X-rays, originating from electron rearrangements within atomic shells. Due to its intermediate half-life and low radiation energy, ^{55}Fe is generally considered less significant in dismantling operations, especially when deferred decommissioning is planned. It often assumes a relatively smaller role compared to other isotopes, such as ^{60}Co.

Carbon-14

^{14}C generation in a reactor primarily occurs through (n,p) reactions involving fast neutrons and ^{14}N, an element found abundantly in air and thus a trace impurity present in virtually all materials, including steel and concrete. The reaction cross section at 1 MeV stands at approximately 0.03 barns. Given the variable concentration of ^{14}N, the quantity of ^{14}C produced also exhibits variability. However, due to its relatively low cross section, it is not generated in substantial amounts. ^{14}C is characterized by a protracted half-life of roughly 5730 years and undergoes decay to ^{14}N by emitting a 156 keV electron. The primary concern associated with this isotope revolves around its long half-life.

Molybdenum-93

The relevance of ^{93}Mo may stem from its prevalence in certain alloys employed for reactor internals. Unlike other relevant isotopes, the production mechanism of ^{93}Mo is somewhat unique, primarily arising from epithermal neutron capture on ^{92}Mo, which accounts for 14.8% of the natural element. In theory, it could also be generated via (n,2n) reactions involving the 9.3% abundant ^{94}Mo, but this process necessitates 10 MeV neutrons. Similarly to the previously discussed ^{56}Fe (n,2n) ^{55}Fe reaction, this energy threshold exceeds the attainable levels within a reactor; consequently, ^{93}Mo tends to assume a relatively less important role as an activation product in comparison to others described in this section. With a half-life of approximately 4000 years, ^{93}Mo decays predominantly via electron capture, with 90% of occurrences resulting in the formation of ^{93m}Nb, which in itself represents a long-lived activation product, featuring a half-life of 13.6 years.

Niobium-94

^{94}Nb, characterized by a half-life of approximately 20,000 years, is primarily created through thermal neutron capture on the 100% naturally occurring ^{93}Nb. This production process exhibits a cross section of 1.14 barns at 0.025 eV. Subsequent to its formation, ^{94}Nb undergoes decay, emitting an electron with a maximum energy of 471 keV to yield ^{94}Mo. Notably, ^{94}Mo releases excess energy in the form of two gamma rays, measuring 703 and 871 keV, respectively. In cases where materials comprising reactor internals contain substantial quantities of ^{93}Nb, this isotope may assume the role of the primary gamma emitter in the decades following the decay of a significant portion of ^{60}Co.

Technetium-99

^{99}Tc, is predominantly significant within the context of nuclear reactors as a fission product, stemming from its proximity to one of the peaks of the fission yield curve of ^{235}U, resulting in an abundance of 6.1%. Concerning waste disposal, this isotope presents a significant challenge owing to its extraordinarily long half-life of approximately 211,000 years and its capacity for high environmental mobility. Nevertheless, ^{99}Tc can also be produced via thermal capture on ^{98}Mo, which constitutes 24% of the natural element composition. ^{98}Mo may be present in certain alloys in substantial quantities. Following neutron capture, ^{99}Mo undergoes decay with a half-life of roughly 66 hours, emitting an electron and transmuting into the considerably longer-lived ^{99}Tc. Eventually, ^{99}Tc further decays into ^{99}Ru by discharging a beta particle with a maximum energy of 295 keV. The capture cross section of ^{98}Mo stands at around 0.13 barns at 0.025 eV, featuring also a non-negligible resonance integral contributing to isotope production. In a manner similar to nickel, molybdenum is incorporated into certain materials to enhance their mechanical properties.

Silver-108m

^{108m}Ag, while more conventionally associated with the disposal of used control rods—owing to the frequent usage of silver within Ag-In-Cd alloys for these components—may also manifest due to the presence of trace silver in steels. This isotope occurs as a consequence of neutron activation on the 52% naturally abundant ^{107}Ag, which exhibits a cross section of 37 barns at 0.025 eV. With a half-life of roughly 438 years, ^{108m}Ag primarily decays to ^{108}Pa through electron capture in 91.3% of occurrences, although in 8.7% of instances, it undergoes an internal transition to ^{108}Ag. The decay to ^{108}Pa yields a series of gamma rays characterized by energies measuring 434, 614, and 723 keV, respectively.

1.4.2 Main activated nuclides in concrete

Concrete possesses a much different composition as compared to steels, giving rise to some unique activation products. Its predominant use lies in shielding applications, particularly in the construction of the bioshield encompassing the reactor. This robust structure, characterized by thick walls, blocks gamma radiation effectively. Notable radioactive isotopes that may be generated within concrete are the following: ^{3}H, ^{41}Ca, ^{152}Eu, and ^{154}Eu. The cross section values reported in the following sections are taken from [13] and [14].

Tritium

^{3}H primarily originates in concrete as a result of the (n,t) reaction with ^{6}Li, a relatively common trace element within the material. This reaction has a significant cross section of 938 barns at 0.025 eV. ^{3}H exhibits a half-life of 12.32 years, with beta decay leading to the formation of ^{3}He with the emission of an electron with a maximum energy of 18.6 keV. The low-energy radiation emitted by ^{3}H results in a comparatively lower risk. However, it is noteworthy to acknowledge that ^{3}H is a gas, and displays high environmental mobility, capable of permeating concrete structures through fissures. Consequently, its diffusion and potential accumulation in inadequately ventilated environments may have to be considered under specific circumstances.

Calcium-41

Within bioshield concrete, ^{41}Ca stands as the predominant activation product, mainly owing to the substantial presence of its precursor, ^{40}Ca, which constitutes approximately 97% of natural calcium. ^{41}Ca is produced exclusively through thermal neutron capture on ^{40}Ca, a reaction with a cross section of 0.41 barns at 0.025 eV. Despite the significant abundance of ^{40}Ca in both natural calcium and the concrete material itself, the overall impact is somewhat lowered by the relatively low cross section associated with the nuclear configuration and the diminished neutron flux reaching the bioshield from the reactor core. Nevertheless, it is expected that dismantling operations will yield a substantial quantity of mildly activated concrete, given the volume of the bioshield within the reactor structure. ^{41}Ca exclusively undergoes decay via electron capture, with the bulk of the energy carried away by a neutrino, while Auger electrons and low-energy X-rays account for the remaining part. Notably, ^{41}Ca features an extraordinarily long half-life of approximately 100,000 years, making it the primary source of activity several millennia following reactor shutdown. Although it does not appear to be generated in significant amounts, it is important to recognize its long biological half-life of 44 years, reflecting the time required for the body to eliminate half of the substance. This retention primarily occurs in the bones. While the potential hazards associated with this isotope merit consideration, its relatively low specific activity, as observed in samples of PWR and BWR bioshield concrete [9], suggests that it does not pose a substantial biohazard. Nevertheless, materials rich in calcium content should be isolated from regions characterized by high neutron fluxes.

Europium-152 and Europium-154

Over the course of several decades following reactor shutdown, ^{152}Eu and ^{154}Eu are anticipated to be the principal activation products in bioshield concrete due to their respective half-lives of 13.5 and 8.6 years. These isotopes stem from thermal neutron capture on their precursors, ^{151}Eu and ^{153}Eu, representing approximately 48% and 52% of natural europium. The reaction cross sections can be quite high, around

9182 barns and 358 barns at 0.025 eV for ^{151}Eu and ^{153}Eu, respectively. Both ^{152}Eu and ^{154}Eu exhibit relatively complex decay patterns. In the case of ^{152}Eu, decay occurs through a combination of beta emission and electron capture, a somewhat unconventional behavior. Beta decays yield the production of ^{152}Gd approximately 28% of the time, with the remaining decays involving electron capture, resulting in the generation of ^{152}Sm. This complex decay sequence gives rise to a gamma cascade spanning from 122 keV to 1.408 MeV, necessitating appropriate consideration. The decay scheme for ^{154}Eu is slightly less intricate, primarily involving decay to various excited states of ^{154}Gd, accompanied by electron emission. Subsequent to this emission, the excess energy is dissipated via a gamma ray cascade ranging from 123 keV to 1.278 MeV.

1.4.3 Main activated nuclides in graphite

Graphite has historically been employed as a neutron moderator in water-cooled, graphite-moderated reactors (RBMK), and it continues to find application in certain contemporary gas-cooled reactor designs. Comprised primarily of carbon, graphite can harbor impurities, resulting in the generation of previously mentioned isotopes such as ^{3}H, ^{14}C, ^{60}Co, ^{152}Eu, and ^{154}Eu. The sole additional isotope necessitating consideration in graphite activation processes is **^{36}Cl**. Cross sections from [13] and [14].

Chlorine-36

The potential for ^{36}Cl generation arises from thermal neutron capture within graphite, attributed to the presence of ^{35}Cl, as chlorine plays a role in the material's production process. If residual chlorine is not effectively removed after manufacturing, a significant quantity of ^{36}Cl can be produced. This isotope exhibits a notable extended half-life of approximately 300000 years and its production cross section stands at 44 barns at 0.025 eV. However, the potential hazard associated with this isotope is somewhat mitigated by the relatively weak beta radiation it emits (710 keV) during decay to ^{36}Ar, coupled with its extended half-life. Roughly 2% of the time, ^{36}Cl decays to ^{36}S via electron capture, accompanied by the emission of a positron.

A summary of the discussed isotopes and their main characteristics is provided in Table 1.1.

Table 1.1 Relevant isotopes in nuclear reactor decommissioning. The half-life $t_{1/2}$ is expressed in years.

Isotope	Precursor	Reaction	Decays into	Decay mode	$t_{1/2}$/y
^{60}Co	^{59}Co,^{60}Ni	n,γ / n,p	^{60}Ni	$\beta-/\gamma$	5.27
^{59}Ni	^{58}Ni	n,γ	^{59}Co	EC / X / γ	80000
^{63}Ni	^{62}Ni	n,γ	^{63}Cu	$\beta-$	100
^{55}Fe	^{54}Fe, ^{56}Fe	n,γ / n,2n	^{55}Mn	EC / X	2.74
^{14}C	^{14}N	n,p	^{14}N	$\beta-$	5730
^{93}Mo	^{92}Mo, ^{94}Mo	n,γ / n,2n	^{93m}Nb	EC	4000
^{94}Nb	^{93}Nb	n,γ	^{94}Mo	$\beta-/\gamma$	200000
^{99}Tc	^{98}Mo	n,γ	^{99}Ru	$\beta-$	211000
^{108m}Ag	^{107}Ag	n,γ	^{108}Pa, ^{108}Ag	EC / IT / γ	438
^{3}H	^{6}Li	n,t	^{3}He	$\beta-$	12.32
^{41}Ca	^{40}Ca	n,γ	^{41}K	EC / X	100000
^{152}Eu	^{151}Eu	n,γ	^{152}Gd, ^{152}Sm	$\beta-$ / EC / γ	13.5
^{154}Eu	^{153}Eu	n,γ	^{154}Gd	$\beta-/\gamma$	8.6
^{36}Cl	^{35}Cl	n,γ	^{36}Ar, ^{36}S	$\beta-$ / EC / $\beta+$	300000

The plots of the cross sections for the reactions of interest described in these sections are available in Figures 1.1, 1.2 and 1.3.

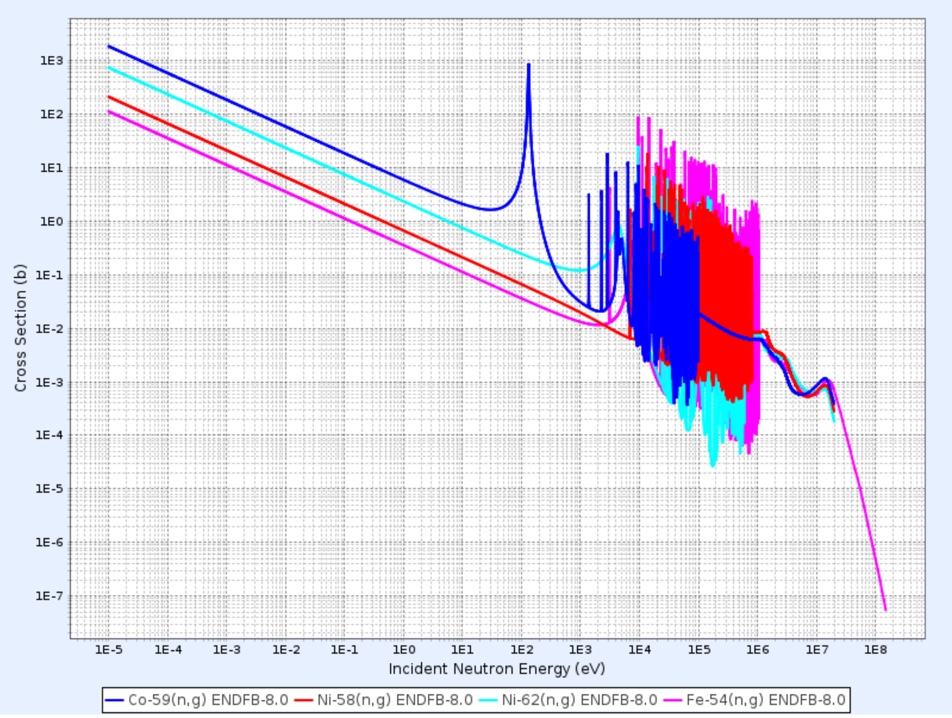

Fig. 1.1 Cross sections of the reaction of interest involving ^{59}Co, ^{58}Ni, ^{62}Ni and ^{54}Fe.

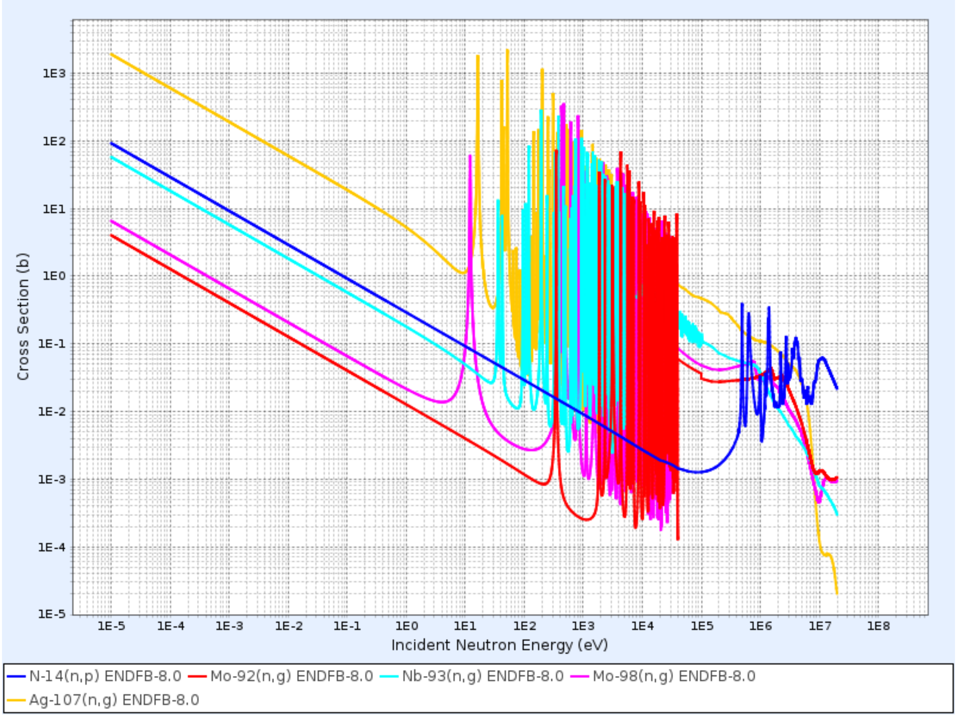

Fig. 1.2 Cross sections of the reaction of interest involving ^{14}N, ^{92}Mo, ^{93}Nb, ^{98}Mo and ^{107}Ag.

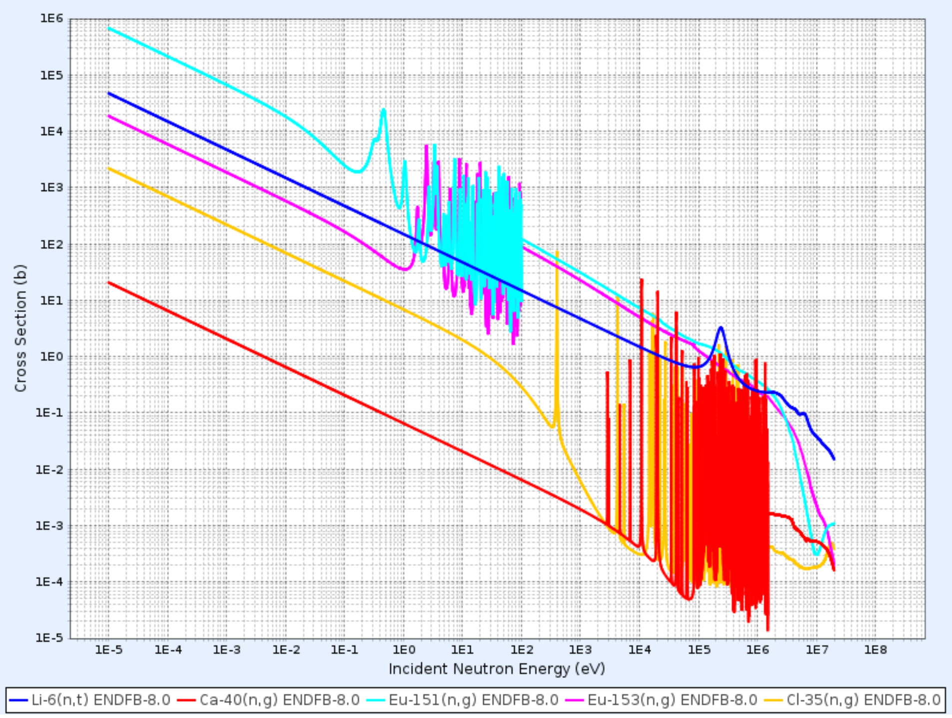

Fig. 1.3 Cross sections of the reaction of interest involving ^{6}Li, ^{40}Ca, ^{151}Eu, ^{153}Eu and ^{35}Cl.

Further, more detailed information on the many complex parameters that concur to the activation phenomenon is available in literature, such as for instance in [15].

1.5 Examples of successful decommissioning projects

The decommissioning of nuclear plants, although not a widely common industrial activity yet, has seen a notable increase in the past few decades. This surge can be attributed to the retirement of many research facilities and power plants. Consequently, there is now a growing repository of successfully completed projects that offer valuable insights into best practices and the proper development of dismantling plans. In the subsequent section, short descriptions of three such successful projects are provided.

1.5.1 Yankee Rowe

The first example of a completed decommissioning project is the case of the Yankee Rowe reactor, a 167 MW_e net PWR constructed between 1957 and 1960 that remained operational until 1991. It represented one of the earliest PWRs to be built in the USA, it generated approximately 34 TWh of electricity throughout its operational life, and at the end of it it was decommissioned by Westinghouse.

In terms of decommissioning strategy, the internals were segmented using underwater plasma cutting, in order to shield workers from gamma radiation [16]. This method, while effective for cutting, had the drawback of significantly reducing the shielding effect of the water, which resulted from the lifting effect caused by the hot gases generated by the cutting torch. The experience gained from the decommissioning of Yankee Rowe led Westinghouse to shift its focus toward mechanical cutting techniques, which, although slower, offer enhanced protection from radiation. Subsequently, many of Westinghouse's decommissioning efforts, including those at the Spanish José Cabrera reactor and the Swedish Barsebäck 1 and 2 reactors, were conducted using mechanical cutting tools.

1.5.2 José Cabrera (Zorita)

The Zorita reactor, a 141 MW_e net PWR, was built between 1964 and 1968, and operated until 2006. Over its operational lifespan, the plant generated approximately 34 TWh of electricity. In particular, the plant featured a single cooling circuit and, consequently, a single steam generator. This configuration expedited the dismantling of the primary circuit due to the reduced volume of material that needed to be removed.

Initially, waste mass, volume, and specific activity limits were established in accordance with disposal site requirements. The choice of available containers and their dimensions were considered alongside the selection of cutting techniques. These decisions considered the geometry of the cut pieces necessary to minimize the number of containers used.

Three-dimensional models of the reactor components and cavity were created to identify the optimal cutting geometry and arrangement of pieces, thereby minimizing congestion in the work area. In 2006-2007, shortly after the plant's closure, the primary circuit, including the vessel, underwent surface decontamination. Other preparatory activities, such as the removal of a section of the wall separating the reactor cavity from the spent fuel pool and the installation of a new working bridge, were conducted to facilitate dismantling. This process also included characterizing the internals and strengthening the floor of the spent fuel pool.

The dismantling of the Zorita reactor was completed relatively fast and is considered a success. The careful selection and application of specific decommissioning techniques, combined with detailed spatial and temporal planning, contributed to reduced execution times and minimized unforeseen challenges during the process [17], [18].

1.5.3 Barsebäck 1 and 2

The Barsebäck 1 and 2 reactors were 600 MW_e net BWRs constructed in Sweden between 1971 and 1975 and between 1973 and 1977, respectively. The first reactor ceased operations definitively in 1999, with the second following suit in 2005. Collectively, these reactors generated approximately 94 and 108 TWh of electricity during their operational lives.

Initially, three strategies were considered for the decommissioning of the large activated components of both reactors:

1. Segmentation of the vessel and internals;
2. Segmentation of the internals and removal of the vessel as a single unit;
3. Removal of the vessel as a single piece, including the internals.

Feasibility studies were conducted to assess the advantages, drawbacks, and handling techniques associated with removing the entire vessel. Of the six preliminary removal techniques considered, three appeared promising:

1. Lifting the vessel and removing it in a vertical position through the reactor building's roof using a crane;
2. Lifting the vessel through the reactor building's roof, positioning it horizontally, and removing it using an overhead crane;
3. Removing the vessel through an opening created in the lower part of the reactor building.

All three techniques relied on established technologies, although the second option was excluded as it required the temporary installation of rather complex components. The third technique, in particular, stood out because the opening at the bottom of the containment building could serve as a conduit for removing other large components, such as steam generators. Furthermore, it did not necessitate the removal of the internal crane, and its radiological impact was relatively low.

However, adjustments to Swedish regulations and modifications to the final repository for activated material were required to apply this technique. Specifically, appropriate transport licenses needed to be obtained, and the repository entrances had to be adapted to accommodate large components. This underscores the importance of designing decommissioning activities with consideration for the availability of repositories and their acceptance criteria.

The segmentation of the internals was carried out by Westinghouse using mechanical cutting, similar to what had been done at numerous other facilities. This task was completed in October 2017 for unit 2, and the equipment was subsequently moved to unit 1 for similar work [19], [20].

1.6 The Italian framework

1.6.1 Facilities and history

Italy's current framework for the nuclear industry is characterized by a certain peculiarity, owing to its early investment in nuclear power, followed by a complete abandonment in 1990. Consequently, the country is now home to numerous nuclear facilities scattered throughout its territory, which have been involved in various aspects of the nuclear fuel cycle or are currently serving as storage sites for radioactive waste. More in detail, Italy invested in the construction and operation of four nuclear power plants: a PWR in Trino, two BWRs in Sessa Aurunca (Garigliano) and Caorso, and a GCR in Latina. Among these, the Latina and Garigliano plants are the oldest, commencing operations in 1963 and 1964, respectively [21].

The Latina GCR, with a design based on the MAGNOX concept, produced 200 MW_e of power and was shut down in 1987. Its decommissioning poses significant challenges, primarily due to the substantial volumes of irradiated graphite it contains. Currently, the international experience in treating such large quantities of irradiated graphite is limited. However, countries like the UK and Russia face similar challenges, promising an increase in knowledge and expertise on this subject.

The Garigliano plant, a 160 MW_e BWR, operated until 1982 when restarting the plant was deemed prohibitively expensive compared to its remaining potential lifespan. The Caorso reactor, also a BWR but with a nominal power of 860 MW_e, was completed in 1978 and operated until 1986. Due to its relatively short operational life, the large reactor components at Caorso are expected to have lower levels of activation as compared to similar BWRs with longer lifespans.

The Enrico Fermi power plant in Trino was a Westinghouse PWR, based on the design of the earlier Yankee Rowe plant in the United States. A third plant following the same design was built in France, at Chooz. Trino's nominal power output was 260 MW_e, and it started operations in 1964, briefly holding the world record as the most powerful commercial reactor. This reactor and its operational history will be further detailed in Section 4.5.2, as it holds particular significance in the context of this thesis work.

Beyond the power plants, Italy houses a former fuel fabrication complex and a reprocessing plant in Bosco Marengo, in addition to several temporary radioactive waste storage sites distributed across the Italian peninsula. Currently, Italy is in the initial stages of selecting a location for the National Repository, which will be responsible for receiving a stream of radioactive waste resulting from the decommissioning efforts at various nuclear facilities [22].

1.6.2 Challenges in dismantling plants

The decommissioning endeavors in Italy present a host of unique challenges, primarily stemming from the utilization of various early reactor designs. These reactors not only differ significantly from each other but also stand apart from most decommissioned plants worldwide in terms of size, materials, geometric configurations, and available workspace. For instance, addressing the decommissioning of the GCR in Latina requires the development of specialized tools for cutting and handling irradiated graphite blocks. These tools must contend with the dual challenges of radioactivity and the fragility induced by neutron damage. Ensuring minimal dust generation and reducing the risk of block breakage during maneuvering constitutes a significant technical hurdle [21].

Additionally, some reactors exhibit distinctive features, such as the external steam generator in Garigliano, an unusual component for a BWR-designed reactor. In the case of the Trino PWR, cruciform control rods with fuel followers introduce another unique characteristic. Due to spatial constraints around these reactors, specific cutting tools may need to be inserted into the pressure vessel for dismantling, thereby requiring an additional level of effort.

Moreover, the diverse spectrum of residual activation and contamination levels, combined with a wide range of materials and intricate geometries, further complicates the overall decommissioning landscape. The absence of a dedicated final repository for radioactive waste and the presence of stringent regulations only serve to increase the complexities of the decommissioning process.

1.6.3 Waste classification

In Italy, the classification of radioactive waste is established based on the DIM 7 agosto 2015 [23], which categorizes waste into distinct classes according to parameters such as specific activity, half-life, and the type of emitted radiation. These categories are defined as follows:

- **Very Short-Lived Waste** (VSLW): This category encompasses waste materials with half-lives shorter than 100 days and that naturally decay to background radiation levels within a maximum of 5 years. VSLW is primarily generated by medical procedures, research activities, and industrial processes;
- **Very Low-Level Waste** (VLLW): Waste falling under this classification should exhibit a specific activity lower than 100 Bq/g overall and less than 10 Bq/g in terms of long-lived alpha emitters;
- **Low-Level Waste** (LLW): This category includes waste materials with a specific activity exceeding 100 Bq/g but lower than 5 MBq/g overall. Furthermore, the activity originating from long-lived nickel isotopes should be below 40 kBq/g, and the activity related to long-lived alpha emitters should not exceed 400 Bq/g. Waste up to this category can be disposed of in surface or shallow repositories;
- **Intermediate Level Waste** (ILW): ILW involves waste materials with specific activity levels higher than those allowed for LLW but without generating sufficient heat to necessitate specialized engineering solutions for heat dissipation. This category is typically associated with waste produced during decommissioning activities, especially when certain reactor components become significantly activated and require extended isolation periods;
- **High-Level Waste** (HLW): Waste materials in this category surpass the specific activity limits for LLW and require specific measures for heat dissipation, as opposed to ILW. Essentially, only spent nuclear fuel and vitrified waste resulting from fuel reprocessing are classified as HLW. The disposal of these materials demands geological repositories tailored to their unique characteristics.

1.7 Collaboration with Sogin

This research project emerged from the collaboration between CIRTEN (Intra-University Consortium for Nuclear Technology Research [24]), which includes

Politecnico di Torino, and Sogin (Società Gestione Impianti Nucleari [25]), the Italian company responsible for the decommissioning of the Italian nuclear facilities. In 2019, both partners entered into an agreement that allowed Sogin to sponsor a temporary research fellow position at Politecnico. The primary objective of this collaboration was to develop innovative methods for the characterization and dismantling of large components within nuclear reactors. Initially, the project entailed exploring available dismantling technologies and developing computational schemes to support characterization efforts. Over time, the focus shifted more toward the modeling aspect, and the Trino reactor was chosen as a test case. The selection of the Trino reactor was influenced by both its proximity to Turin and the availability of specific activity measurements, which proved valuable for validating the computational model developed during the project. Specifically, the goal of this research project was to create a 3D multi-step calculation scheme for assessing the residual activation in various components of the Trino reactor.

As previously introduced, the Trino reactor was Italy's sole PWR. Completed in 1964 and situated between Turin and Vercelli with cooling provided by the Po river, this reactor represented Italy's response to a growing energy demand driven by significant industrial development during those years. The reactor operated initially at 825 MW_{th} and later at 870 MW_{th}, although its original design specified a lower nominal power of 615 MW_{th}. The power increase was achieved through a novel industrial practice, the chemical control of long-term reactivity that employed boric acid dissolved in the coolant as a homogeneous neutron sink. The reactor featured four primary loops and operated from 1964 to 1987, spanning nine operating cycles. The first cycle differed substantially from the subsequent ones, with the presence of a thermal shield around the core to reduce the irradiation of the RPV and fuel followers attached to the control rods. Starting from the second operating cycle, the thermal shield was removed, and eight corner fuel assemblies were replaced with dummy zircaloy elements to compensate for the shield's absence. The loading pattern was altered from high-leakage to low-leakage to reduce neutron leaks and enhance overall neutron economy. The reactor operated at 825 MW_{th} for the first three cycles, reaching its full nominal power of 870 MW_{th} from the fourth cycle onwards. After the fourth cycle, the fuel followers were deemed too depleted for further use and were replaced with dummy zircaloy followers. Subsequent cycles maintained the core geometry and nominal power without modifications, but average enrichment increased, and the reactor briefly experimented with some MOX fuel assemblies as well [26], [27].

Distinct from most nuclear reactors, the Trino reactor had a complex history characterized by numerous geometry changes, enrichment variations, and inconsistent operation. These unique factors pose a particular challenge when assessing residual activation. Earlier activation studies, conducted in the 1990s, mainly employed 1D and 2D computational tools [27]. However, Sogin sought to expand these studies and explore different modeling approaches for a more comprehensive evaluation of the reactor's residual activation.

Simultaneously with the modeling activity, a collaborative research project was undertaken in partnership with the Department of Mechanical and Aerospace Engineering (DIMEAS) to establish a methodology for the selection of cutting techniques applicable to the dismantling of large, activated components within a nuclear power plant. This constituted another primary goal of the temporary research fellowship. The devised methodology considered multiple performance parameters to enable effective comparisons among various cutting techniques. These parameters encompassed factors such as cutting speed, industrial safety considerations, and the generation of secondary waste. Additionally, the methodology incorporated site-specific requirements, including the nature of materials to be cut and the available workspace. More details and findings from this research effort will be explained in Appendix A.

Chapter 2

Modeling in support to decommissioning plans: neutron activation analysis

2.1 Role of modeling activities for decommissioning

Among the several aspects that should be considered when planning the decommissioning of a nuclear facility, neutron activation requires particular attention. This peculiar characteristic is, in fact, the main difference between nuclear and other conventional thermal power plants. Since it represents a potential significant health hazard for workers, it is the main source of many of the complexities revolving around dismantling operations and it has to be carefully addressed to optimize the process. Neutron activation studies, on which this work is focused, represent a supporting tool to address this issue, as various modeling approaches can be combined to accurately describe the problem.

The role of modeling activities in decommissioning studies holds significant value. Computational models offer a degree of flexibility in analyzing distinct components of the reactor, making them invaluable in estimating parameters crucial to the dismantling process, such as specific activities and contact dose rates. Various models serve different purposes, with some designed to simulate neutron transport away from the source, while others focus predominantly on activation phenomena.

Certain models are dedicated to examining the gamma fields generated by specific activation products, making them necessary for radiation protection considerations.

Models, in general, serve several functions: they can validate hypotheses, provide insights into irradiated regions that are inaccessible for sampling due to geometric constraints, and offer adaptability to different configurations. For instance, different modeling choices can be compared to discover which configuration is the best at replicating experimental results. Models can be validated using various means, including flux measurements from different reactor regions or specific activity measurements. Flux measurements, often gathered through vessel surveillance programs aimed at collecting neutron fluence data to better understand material aging processes, are beneficial for validating calculation schemes that center on the study of neutron transport. Specific activity measurements may result from experimental activities, such as the planned irradiation of activation foils made from specific materials, or stem from measurements conducted for industrial purposes.

A comprehensive radiological characterization of a reactor typically relies on the combined contributions of both sampling and modeling activities, as sampling is often constrained to specific areas due to logistics and regulation. Developing a 3D residual activation map can be beneficial in optimizing the segmentation plan, should it be part of the strategy, ultimately reducing costs by minimizing the production of higher-level waste. Furthermore, transport/activation models can be adapted to represent different reactors, provided the geometrical model is adjusted accordingly.

2.2 Challenge of validating computational models using legacy data

The case study of the Trino reactor is somewhat unique, as it comes with an additional challenge. Most of the measurements taken at the plant were initially collected for industrial purposes and were not derived from experiments with well-defined boundary conditions. This legacy data, while still valuable, can pose difficulties in model validation due to the limited description of the measuring setup or the lack of a detailed account of the overall analysis procedure.

In some instances, sample locations may not be adequately described, especially in terms of spatial coordinates, which complicates efforts to make precise comparisons with calculations, particularly in regions characterized by steep neutron flux gradients. Some data might be incomplete or entirely missing, while certain measurements may lack associated error bars, further complicating the comparison process. The older the reactor, the more challenging it becomes to gather valuable information about its operation, geometry, or any modifications introduced during its operational life. A good example would be the nominal power, which was modified twice: initially the reactor was designed to operate at a maximum of 615 MW_{th}, since power control was planned to be performed using only the control rods. This value was increased to 825 MW_{th} before startup, as long term reactivity control was introduced. Finally the power was increased to 870 MW_{th} after the fourth cycle. The only information initially available on the nominal power was the last one, which was used until further information was discovered and allowed to update the power when necessary.

Before the widespread use of digitalization, many documents may have become old, damaged, lost, or difficult to read, often stored in extensive, poorly organized archives. In essence, there is a significant amount of "*archeology*" involved in the quest for the necessary information to construct a computational model. In addition to documentation, another exceptionally valuable source of information, particularly in similar cases, is the former and current plant workers who often serve as living repositories of precious knowledge.

2.3 The neutron transport equation and the calculation of reaction rates

The neutron source in a nuclear reactor is the result of fission reactions. These fissions produce heat and a variable number of secondary neutrons, which continue the chain reaction and enable power generation. As previously introduced, residual activation in supporting structures occurs due to the interaction between the neutron flux and the atoms in the material, therefore, the reaction rates between neutrons and these target nuclei are the primary parameters that need to be calculated [28].

Let us consider an arbitrary volume, dV, around the point, $\bar{r}$, in the system, with energies, dE, around E. The reaction rate in $dVdE$ is expressed as:

$$\mathrm{v}\Sigma(\bar{r},E)N(\bar{r},E) = \Sigma(\bar{r},E)\Psi(\bar{r},E) \tag{2.1}$$

Here, v is the neutron speed, $\Sigma(E)$ is the macroscopic cross section of the reaction of interest, and $N(\bar{r},E)$ is the neutron density. The product of neutron speed and neutron density is commonly referred to as the *neutron flux*, which plays a fundamental role in calculating reaction rates. It is important to emphasize that the reaction cross section strongly depends on the energy of incoming neutrons, therefore understanding the energy distribution of incoming particles in regions susceptible to activation phenomena is critical. This energy distribution of neutrons is known as the energy spectrum and significantly influences material activation.

To estimate the residual activation, the general objective in transport calculations is to compute neutron flux values in various parts of the reactor and their associated energy spectra. The model should consider not only the neutron source but also the regions of interest, which may be located far away from it, as well as all the material in between, which can interact with neutrons.

The neutron flux calculation is mathematically governed by the Boltzmann transport equation, originally derived to describe the kinetic theory of gases, a problem that shares some similarities with neutron behavior. The Boltzmann transport equation for the neutron angular flux is essentially a particle balance in a specific region of the phase space that describes gains and losses of neutrons due to various interactions, such as fission, neutron scattering, or absorption. Considering that the general form of the equation can be quite complex, as it depends on space, energy, flight direction, and time, it is often more useful to consider specific cases. A particularly valuable form is the integro-differential version in its time-independent form, as activation mainly occurs during steady-state operation:

$$\begin{aligned}\hat{\Omega}\cdot\nabla\psi(\bar{r},\hat{\Omega},E) + \Sigma_t(\bar{r},E)\psi(\bar{r},\hat{\Omega},E)\\ = \int_0^\infty \oint_{4\pi} \Sigma(\bar{r},E')f(\bar{r};\hat{\Omega}',E' \to \hat{\Omega},E)\psi(\bar{r},\hat{\Omega}',E')d\hat{\Omega}'dE' + q(\bar{r},\hat{\Omega},E)\end{aligned} \tag{2.2}$$

In this equation, $\bar{r}$ represents the spatial variable, $\hat{\Omega}$ is the flight direction, and E is the energy. ψ is the angular neutron flux, while the scalar neutron flux, which can be computed by integrating the angular neutron flux over the solid angle, is another parameter of interest. Σ_t is the total macroscopic cross section, representing the probability of interaction per unit length. The product $\Sigma(\bar{r},E')f(\bar{r};\hat{\Omega}',E' \rightarrow \hat{\Omega},E)$ represents the total probability of neutron transfer from Ω',E' to Ω,E, which considers all the possible interactions that modify the direction and energy of the incoming neutron. The term can be further broken down to separate the contributions of fission (Σ_f) and collision (Σ_x) reactions, as reported in Equation (2.3):

$$\begin{gathered}\Sigma(\bar{r},E')f(\bar{r};\hat{\Omega}',E' \rightarrow \hat{\Omega},E) = \\ \frac{1}{4\pi}\Sigma_f(\bar{r},E')\nu(\bar{r},E' \rightarrow E) + \sum_{x \neq f} \Sigma_x(\bar{r},E')f_x(\bar{r};\hat{\Omega}',E' \rightarrow \hat{\Omega},E)\end{gathered} \tag{2.3}$$

$\nu(\bar{r},E' \rightarrow E)$ is the spectrum of the fission neutrons, i.e. the probability that a fission caused by a neutron at $\bar{r}$ with energy E' will lead to a neutron with energy about E within dE. The summation over $x \neq f$ identifies all non-fission reactions from which neutrons emerge, such as scattering or (n,2n). q represents a generic external source of neutrons in the analyzed phase space. This source in activation calculations is provided by neutrons incoming from the reactor core, since no neutrons are generated by external sources in the supporting materials of the reactor. Any reader interested in more details on neutron transport theory could refer to the many books that cover this topic available in literature, such as [29], [30], [31], [32], [33].

2.3.1 Forward and adjoint transport in operator form

A more concise version of the time independent transport equation can be written in operator form [32], also known as the *forward* equation:

$$\mathbf{L}\psi(\bar{r},\hat{\Omega},E) + q(\bar{r},\hat{\Omega},E) = 0 \tag{2.4}$$

In this equation, **L** is the transport operator:

$$\begin{aligned}\mathbf{L}\psi(\bar{r},\hat{\Omega},E) &= -\hat{\Omega}\cdot\nabla\psi(\bar{r},\hat{\Omega},E) - \Sigma_t(\bar{r},E)\psi(\bar{r},\hat{\Omega},E) \\ &+ \int_0^\infty \oint_{4\pi} \Sigma(\bar{r},E')f(\bar{r};\hat{\Omega}',E' \rightarrow \hat{\Omega},E)\psi(\bar{r},\hat{\Omega}',E')d\hat{\Omega}'dE'\end{aligned} \tag{2.5}$$

Once ψ is known, it can be used to determine the reaction rates of interest, since the reaction rate can be defined as the product of the angular flux ψ and the probability of the desired interaction (e.g. the cross section for (n,γ) reactions) integrated over the arbitrary volume belonging to the selected phase space of interest:

$$R = \int_V \oint_{4\pi} \int_E \Sigma_{n,\gamma}(\bar{r},E)\,\psi(\bar{r},\hat{\Omega},E)\,dE\,d\hat{\Omega}\,dV \tag{2.6}$$

It is also possible to derive the mathematical *adjoint* to the transport equation. It will be later shown that the solutions of this equation have a clear physical significance, known as "*importance*" of the neutrons inside a system [32]. These solutions are generally used in several applications such as perturbation theory and variance reduction in MC calculations, and this latter application is the one used in the framework of this work.

In order to derive the adjoint equation, it is necessary to define certain quantities and their inner product. Let $f(\xi)$ and $g(\xi)$ be two functions of the same variable ξ. The inner product of these functions is defined as:

$$\langle f,g\rangle \equiv \int f(\xi)g(\xi)d\xi \tag{2.7}$$

with the integration performed over the entire range of variables, i.e. the whole system volume, all possible energies and directions. If both the functions are "well-behaved", i.e. they are suitable in terms of continuity and boundary conditions, then a self-adjoint operator $\mathbf{M}$ would allow to state the following equivalence between the two inner products:

$$\langle f,\mathbf{M}g\rangle = \langle g,\mathbf{M}f\rangle \tag{2.8}$$

In the framework of neutron transport theory, both the operators and the functions on which they are applied (e.g. the neutron angular flux) are real, therefore no complex conjugates are necessary in the definition of the inner product, as it occurs, for instance, in the framework of quantum mechanics. The operator associated with the transport equation $\mathbf{L}$, however, is not self-adjoint, and for this reason it is possible to define a second operator $\mathbf{L}^{\dagger}$ which is adjoint to $\mathbf{L}$. This second operator $\mathbf{L}^{\dagger}$ will operate on the adjoint functions $f^{\dagger}$, which can have different boundary conditions compared to the ones satisfied by the functions g on which the original operator $\mathbf{L}$ operates, and is defined by the following requirement:

$$\left\langle f^{\dagger},\mathbf{L}g\right\rangle = \left\langle g,\mathbf{L}^{\dagger}f^{\dagger}\right\rangle \tag{2.9}$$

for any "acceptable" functions $f^\dagger$ and g. The eigenfunctions of the adjoint operator $\mathbf{L}^\dagger$ are then orthogonal to the eigenfunctions of the operator $\mathbf{L}$. Therefore, if g is an eigenfunction of the transport operator $\mathbf{L}$ such that:

$$\mathbf{L}g = \lambda g \tag{2.10}$$

and $f^\dagger$ is an eigenfunction of the adjoint transport operator $\mathbf{L}^\dagger$ such that:

$$\mathbf{L}^\dagger f^\dagger = \eta f^\dagger \tag{2.11}$$

then Equation (2.9) would result in:

$$(\lambda - \eta)\left\langle f^\dagger, g\right\rangle = 0 \tag{2.12}$$

Consequently, if $\lambda \neq \eta$, then $\left\langle f^\dagger, g\right\rangle = 0$, which means that the eigenfunctions of the two operators $\mathbf{L}$ and $\mathbf{L}^\dagger$ corresponding to different eigenvalues λ and η, are orthogonal. If the eigenvalues were equal, the inner product would differ from 0.

It can be demonstrated that the transport operator $\mathbf{L}$ is not self-adjoint, as previously introduced, i.e.:

$$\langle f, \mathbf{L}g\rangle \neq \langle g, \mathbf{L}f\rangle \tag{2.13}$$

Let us consider, for instance, Equation (2.5), where the transport operator $\mathbf{L}$ is applied to the angular neutron flux ψ. If it was applied to the generic functions f or g, the gradient term, in $\langle f, \mathbf{L}g\rangle$, would be equal to:

$$\int_V \int_0^\infty \oint_{4\pi} -f[\hat{\Omega} \cdot \nabla g]\, d\hat{\Omega} dE dV \tag{2.14}$$

but the same term in $\langle g, \mathbf{L}f\rangle$ would be:

$$\int_V \int_0^\infty \oint_{4\pi} -g[\hat{\Omega} \cdot \nabla f]\, d\hat{\Omega} dE dV \tag{2.15}$$

and in general terms, these quantities are different. A similar consideration is valid for the integral term, therefore, it follows that the two inner products are not equal, and the transport operator is not self-adjoint.

Let us consider now the angular neutron flux ψ and its adjoint angular flux $\psi^\dagger$. The transport operator $\mathbf{L}$ will operate on the former and the adjoint operator $\mathbf{L}^\dagger$ will operate on the latter, such that:

$$\left\langle \psi^{\dagger}, \mathbf{L}\psi \right\rangle = \left\langle \psi, \mathbf{L}^{\dagger}\psi^{\dagger} \right\rangle \tag{2.16}$$

These two functions both satisfy the appropriate boundary and continuity conditions for the angular and adjoint flux. More in detail, the angular flux satisfies the condition $\psi(\bar{r},\hat{\Omega},E) = 0$ for all incoming neutron directions, i.e. for $\hat{n}\cdot\hat{\Omega} < 0$, and the adjoint flux satisfies the condition $\psi^{\dagger}(\bar{r},\hat{\Omega},E) = 0$ for all outgoing neutron directions, i.e. for $\hat{n}\cdot\hat{\Omega} > 0$. Therefore, in accordance with the definition of the adjoint transport operator $\mathbf{L}^{\dagger}$:

$$\begin{aligned} \mathbf{L}^{\dagger}\psi^{\dagger}(\bar{r},\hat{\Omega},E) &= \hat{\Omega}\cdot\nabla\psi^{\dagger}(\bar{r},\hat{\Omega},E) - \Sigma_t(\bar{r},E)\psi^{\dagger}(\bar{r},\hat{\Omega},E) \\ &+ \int_0^{\infty}\oint_{4\pi}\Sigma(\bar{r},E)f(\bar{r};\hat{\Omega},E\rightarrow\hat{\Omega}',E')\psi^{\dagger}(\bar{r},\hat{\Omega}',E')d\hat{\Omega}'dE' \end{aligned} \tag{2.17}$$

There are two notable differences between $\mathbf{L}^{\dagger}$ as given by Equation (2.17) and $\mathbf{L}$ from Equation (2.5):

- the gradient (or streaming) terms have opposite signs;
- in the scattering functions the before and after parts have been switched.

It can be demonstrated that $\mathbf{L}^{\dagger}$ is, in fact, the adjoint operator and satisfies Equation (2.16), i.e.:

$$\begin{aligned} &\int_V\int_0^{\infty}\oint_{4\pi}\psi^{\dagger}(\bar{r},\hat{\Omega},E)\mathbf{L}\psi(\bar{r},\hat{\Omega},E)d\hat{\Omega}dEdV = \\ &\int_V\int_0^{\infty}\oint_{4\pi}\psi(\bar{r},\hat{\Omega},E)\mathbf{L}^{\dagger}\psi^{\dagger}(\bar{r},\hat{\Omega},E)d\hat{\Omega}dEdV \end{aligned} \tag{2.18}$$

It is clear from the expressions used to define $\mathbf{L}\psi$ and $\mathbf{L}^{\dagger}\psi^{\dagger}$ in Equations (2.5) and (2.17) respectively that each one is formed by three terms: a gradient (streaming) term, a removal term and a scattering term. The removal terms are the same, and the same consideration is valid for the scattering term, provided the exchange of the integration variables on one side. Only the two streaming terms have to be proven equal in order for Equation (2.16) to be satisfied, and this can be done analyzing the difference between the two streaming terms. This difference Δ can be written as:

$$\begin{aligned} \Delta = \int_V\int_0^{\infty}\oint_{4\pi}&[\psi^{\dagger}(\bar{r},\hat{\Omega},E)(\hat{\Omega}\cdot\nabla\psi(\bar{r},\hat{\Omega},E)) \\ &+\psi(\bar{r},\hat{\Omega},E)(\hat{\Omega}\cdot\nabla\psi^{\dagger}(\bar{r},\hat{\Omega},E))]d\hat{\Omega}dEdV \end{aligned} \tag{2.19}$$

If Δ can be proved to be equal to 0, then Equation (2.16) is satisfied. Considering that ∇ does not operate on directions, it is possible to rewrite $\hat{\Omega} \cdot \nabla \psi$ as $\nabla \cdot \hat{\Omega} \psi$ and $\hat{\Omega} \cdot \nabla \psi^\dagger$ as $\nabla \cdot \hat{\Omega} \psi^\dagger$. The two terms of Equation (2.19) can therefore be combined and the Equation can be rewritten as:

$$\Delta = \int_V \int_0^\infty \oint_{4\pi} \nabla \cdot \hat{\Omega} \psi^\dagger(\bar{r}, \hat{\Omega}, E) \psi(\bar{r}, \hat{\Omega}, E) d\hat{\Omega} dE dV \tag{2.20}$$

By using the divergence theorem this volume integral can be transformed into a surface integral, resulting in:

$$\Delta = \int_A \int_0^\infty \oint_{4\pi} \hat{n} \cdot \hat{\Omega} \psi^\dagger(\bar{r}, \hat{\Omega}, E) \psi(\bar{r}, \hat{\Omega}, E) d\hat{\Omega} dE dA \tag{2.21}$$

and the integration is performed on the boundary surface A, where the boundary conditions are imposed. On the surface, the product between the angular neutron flux and its adjoint, however, is always equal to 0, due to the boundary conditions listed before. For this reason $\Delta = 0$ and Equation (2.16) is satisfied.

As previously introduced, the solutions to the adjoint equation have a physical meaning, known as neutron *importance*, that can be better understood with an example.

Let us consider a subcritical, steady state system with an arbitrary steady source $q(\bar{r}, \hat{\Omega}, E)$. In the system there is also a neutron detector, whose response is proportional to the reaction of interest (e.g. the ^{10}B(n,α) reaction) characterized by the macroscopic cross section $\Sigma_d(\bar{r}, E)$. The angular neutron flux in the system satisfies the Equation (2.4), therefore:

$$\mathbf{L} \psi(\bar{r}, \hat{\Omega}, E) = -q(\bar{r}, \hat{\Omega}, E) \tag{2.22}$$

or

$$\begin{gathered} \hat{\Omega} \cdot \nabla \psi(\bar{r}, \hat{\Omega}, E) + \Sigma_t(\bar{r}, E) \psi(\bar{r}, \hat{\Omega}, E) = \\ + \int_0^\infty \oint_{4\pi} \Sigma(\bar{r}, E') f(\bar{r}; \hat{\Omega}', E' \rightarrow \hat{\Omega}, E) \psi(\bar{r}, \hat{\Omega}', E') d\hat{\Omega}' dE' + q(\bar{r}, \hat{\Omega}, E) \end{gathered} \tag{2.23}$$

with the boundary condition of no incoming neutrons. Let us now consider the adjoint equation with source $\Sigma_d(\bar{r}, E)$:

$$\mathbf{L}^\dagger \psi^\dagger(\bar{r}, \hat{\Omega}, E) = -\Sigma_d(\bar{r}, E) \tag{2.24}$$

or, in its extended form:

$$\begin{aligned}-\hat{\Omega}\cdot\nabla\psi^{\dagger}(\bar{r},\hat{\Omega},E)+\Sigma_t(\bar{r},E)\psi^{\dagger}(\bar{r},\hat{\Omega},E)=\\+\int_0^{\infty}\oint_{4\pi}\Sigma(\bar{r},E)f(\bar{r};\hat{\Omega},E\rightarrow\hat{\Omega}',E')\psi^{\dagger}(\bar{r},\hat{\Omega}',E')d\hat{\Omega}'dE'+\Sigma_d(\bar{r},E)\end{aligned} \tag{2.25}$$

with the boundary condition of no outgoing adjoint flux. Equation (2.23) is then multiplied by $\psi^{\dagger}(\bar{r},\hat{\Omega},E)$ and Equation (2.25) is multiplied by $\psi(\bar{r},\hat{\Omega},E)$. The resulting expressions are subtracted, and this difference is then integrated over all variables. Using then the definition of the adjoint operator in Equation (2.16), it is possible to discover that:

$$\int_V\int_0^{\infty}\oint_{4\pi}q(\bar{r},\hat{\Omega},E)\psi^{\dagger}(\bar{r},\hat{\Omega},E)d\hat{\Omega}dEdV=\int_V\int_0^{\infty}\oint_{4\pi}\Sigma_d(\bar{r},E)\psi(\bar{r},\hat{\Omega},E)d\hat{\Omega}dEdV \tag{2.26}$$

It is possible to notice that the right side of the equation is proportional to the detector response to the source $q(\bar{r},\hat{\Omega},E)$, but the source itself, is arbitrary. It could be, for instance, a unit source with particular values of $\bar{r}_0,\hat{\Omega}_0,E_0$, in which case:

$$\psi^{\dagger}(\bar{r}_0,\hat{\Omega}_0,E_0)=\int_V\int_0^{\infty}\oint_{4\pi}\Sigma_d(\bar{r},E)\psi(\bar{r},\hat{\Omega},E)d\hat{\Omega}dEdV \tag{2.27}$$

The adjoint flux is therefore proportional to the detector response. It is, in fact, a measure of the neutron importance in contributing to that specific detector, and this aspect is also in line with the boundary conditions previously defined, as neutrons leaving the system have "no importance", in the sense that they cannot return and are, therefore, essentially useless. Clearly, not all neutrons are equal in terms of relevance to the desired score (e.g. if they are moving in the wrong direction). The concept of neutron importance is widely used in numerical methods, specially in techniques used to accelerate the convergence of simulations. This topic will be further discussed in Section 2.4.2. More information on the topic of adjoint transport is available in literature, for instance at [32], [34] and [35].

2.4 Neutron transport modeling approaches

The numerical modeling of the neutron flux in the reactor core, essential for determining the activation source, can be approached through deterministic or stochastic methods.

Deterministic methods are typically employed to solve approximations of the transport equation, involving the discretization of various transport process variables, such as space, energy, flight direction, and time [36]. In deterministic methods, each cell within the generated mesh is characterized by constant properties, like cross sections. These methods have historically been favored due to their relatively modest computational requirements, particularly when considering the limitations of neutron diffusion approximations and the computer technology available in the 1990s.

In contrast, the Monte Carlo (MC) method relies on aggregated information obtained through the statistical sampling of numerous particle histories. It simulates neutron propagation and interaction phenomena by accessing continuous-energy cross section libraries. The geometry complexity can be retained at a high level of detail, eliminating the approximation introduced by the spatial discretization process employed in deterministic methods. For these reasons, MC codes enable a more realistic representation of the transport mechanism [37]. They have been effectively utilized in the past for investigating activation phenomena in structural components [38], [19], [39], [40], [36], [41]. It is worth noting that running a large number of neutron histories may be necessary to obtain statistically significant results, which can have an impact on the processing power required.

2.4.1 Deterministic methods

The absence of exact solutions for the transport equation, except for very simplified and specific cases, necessitates the use of numerical solutions. To numerically solve the steady-state transport equation, at least three variables must be discretized: *energy*, *angle*, and *space* (in steady state operation) plus *time* (if transient phenomena are investigated).

The *energy* variable is discretized using the multi-group approach, where the range of possible energies is divided into a set of finite energy groups. Parameters dependent on energy (e.g., cross sections) are defined by a single value for each specific energy interval. Assuming G energy groups, the discretized multi-group equation takes the form:

$$\begin{aligned}&\hat{\Omega}\cdot\nabla\psi^{g}(\bar{r},\hat{\Omega})+\Sigma_{t}^{g}(\bar{r})\psi^{g}(\bar{r},\hat{\Omega})\\ &=\sum_{g'=1}^{G}\int_{4\pi}\Sigma_{s}^{gg'}(\bar{r},\hat{\Omega}'\cdot\hat{\Omega})\psi^{g'}(\bar{r},\hat{\Omega})d\hat{\Omega}'+q^{g}(\bar{r},\hat{\Omega})\end{aligned}\tag{2.28}$$

In this equation, ψ^g represents the flux integrated over the energy group g. The total flux, mathematically expressed as $\Psi = \int \psi(E)dE$, becomes a discrete sum of contributions, with $\psi = \psi^g$ for each energy group. The number of energy groups can vary depending on the nature of the problem, ranging from a basic division into two groups for fast and thermal neutrons to several hundred groups.

The *angular* variable is usually treated using either the projection on spherical harmonics (P_n) or the discretization in a finite set of ordinates (S_n) [35] [42]. Between these two, S_n is comparatively more common, as it provides solutions for a larger range of practical problems much more cheaply than P_n. This method replaces the angular dependence $\hat{\Omega}$ with a discrete set of ordinates Ω_m, and then integrates the transport equation across homogeneous regions. The index N, an even number, determines the number of discrete directions, given in a 3D geometry by the formula $N(N+2)$. For instance, in S_8 ($N = 8$), the total number of directions is 80, equating to 10 directions per octant. Higher N values result in more directions and greater accuracy, but very high N values are uncommon due to increased computational costs. Each direction corresponds to a specific cone on the unit sphere with an associated weight, which contributes to the calculation within that direction through the use of quadrature sets, as the integrals become discrete contributions that have to be summed. A third method that recently gained popularity among users of deterministic techniques for the solution of the transport equation is the method of characteristics (*MoC*) [43] [44] [45], [46]. This method is based on the solution of the transport equation in its characteristic form following the neutron path along specific directions Ω_m. It is a a powerful and flexible method implemented in many deterministic solvers (e.g. APOLLO2 [47]), although for large problems it can be affected by memory issues. The scattering cross section $\Sigma_s(\bar{r},\hat{\Omega}'\cdot\hat{\Omega},E'\to E)$ is another parameter that requires numerical treatment, and is typically expanded using Legendre polynomials with the desired scattering order l. If μ_0 is defined as the cosine of the scattering angle $\hat{\Omega}'\cdot\hat{\Omega}$ for a more compact notation, the expansion of

$\Sigma_s(\bar{r},\mu_0,E' \to E)$ can be expressed as:

$$\Sigma_s(\bar{r},\mu_0,E' \to E) = \sum_{l=0}^{\infty}(2l+1)\Sigma_{sl}(\bar{r},E' \to E)P_l(\mu_0) \tag{2.29}$$

The Legendre polynomials $P_l(\mu_0)$ are a complete set of polynomials which satisfy the orthogonality relationship on the interval $-1 \leqslant \mu_0 \leqslant 1$ such that:

$$\frac{1}{2}\int_{-1}^{1} P_l(\mu_0)P_{l'}(\mu_0)d\mu_0 = \frac{\delta_{ll'}}{2l+1} \tag{2.30}$$

where $\delta_{ll'}$ is the Kroenecker delta, equal to 1 if $l = l'$ and equal to 0 otherwise [35]. In Equation (2.29), these polynomials can be used to ensure the positivity of the angular flux expansion. The orthogonality property of the polynomials allows to evaluate the Legendre moments of the cross section $\Sigma_{sl}(\bar{r},E' \to E)$:

$$\Sigma_{sl}(\bar{r},E' \to E) = \int_{-1}^{1} \frac{1}{2}\Sigma_s(\bar{r},\mu_0,E' \to E)P_l(\mu_0)d\mu_0 \tag{2.31}$$

with the expansion truncated consistently to the anisotropy level considered.

The final variable to be discretized is *space*. Traditional discretization methods rely on well-known techniques such as finite differences, finite elements, or nodal methods. These methods perform well for thin cells, but coarser cells can produce oscillatory results, especially when employing schemes like the diamond difference, therefore careful consideration of cell size is essential.

There are several deterministic methods to solve the transport equation, and while an overview of the problem was deemed interesting, in the framework of this thesis most of the calculations were performed using Monte Carlo methods. Any reader interested in a more detailed analysis of deterministic methods for the solution of the transport equation can consult the available literature for instance at [35], [46], [42], [44], [43].

2.4.2 The Monte Carlo method

As previously introduced, the Monte Carlo (MC) method is grounded in statistics. It involves describing the life of a single neutron in terms of probabilities. Each neutron has a certain probability of being born in the analyzed phase space, then traveling without interaction and eventually interacting. These interaction probabilities correspond to macroscopic cross sections and are used to describe real-world physics without making any approximations to the transport equation. The MC method does not require discretization of the spatial domain or division of energies into groups since energy is treated as a continuous variable in many state-of-the-art codes.

The code chosen for the analyses in the framework of this work is Serpent 2, which stands as a versatile three-dimensional continuous energy MC particle transport code, originally crafted by the VTT Technical Research Centre of Finland [48]. It can be used for a wide range of transport applications, using neutrons, photons or both in coupled neutron-photon simulations. Some of the possible applications are, for instance, reactor modeling, criticality studies, group constant generation to provide input data for deterministic simulations, fuel depletion and accelerated particle transport. This latter capability in particular has been extensively exploited to evaluate neutron fluxes impacting on the structures of the Trino reactor, and led to the results reported in Chapters 3, 4 and 5.

Analog MC

Despite its many advantages, MC methods are inherently statistical, which means simulations are subject to statistical errors. This error is related to the number of neutron histories simulated, and it can be reduced by increasing the number of simulated neutrons. However, this also demands more computing power, and if the computational demands become too high, MC simulations may become impractical compared to deterministic methods. Therefore, a balance must be found between available resources and desired accuracy.

The relevance of MC methods in neutron transport stems from the possibility to evaluate integrals [37]. Let us assume we are interested in evaluating the definite integral:

$$I = \int_a^b f(x)dx \tag{2.32}$$

This integral could be rewritten as:

$$I = \int_a^b f(x)dx = \int_a^b h(x)\varphi(x)dx \tag{2.33}$$

where $h(x)$ is a weight function that needs to be chosen correctly and $\varphi(x)$ is a *probability density function* (pdf), defined as follows:

$$\int_a^b \varphi(x)dx = 1, \varphi(x) \geq 0, x \in [a,b] \tag{2.34}$$

It is possible to sample N random variables according to the pdf on the interval $[a,b]$:

$$P(x_i < x) = \int_a^x \varphi(x)dx \tag{2.35}$$

and obtain an estimation of the value of the finite integral I:

$$\bar{I} = \frac{1}{N}\sum_{i=1}^{N} h(x_i) \tag{2.36}$$

In fact I is the expected value based on the probability distribution of the random variables:

$$\langle \bar{I} \rangle = \frac{1}{N}\sum_{i=1}^{N}\int_a^b h(x_i)\varphi(x_i)dx_i = \frac{1}{N}\sum_{i=1}^{N}\int_a^b f(x_i)dx_i = I \tag{2.37}$$

Going back to the original problem:

$$I = \int_a^b f(x)dx \tag{2.38}$$

the easiest choice for $h(x)$ would be the ratio between $f(x)$ and $\varphi(x)$:

$$h(x) = \frac{f(x)}{\varphi(x)} \tag{2.39}$$

and the most trivial choice for $\varphi(x)$ would be an even distribution on the interval $[a,b]$:

$$\varphi(x) = \begin{cases} \frac{1}{b-a}, x \in [a,b] \\ 0, x \notin [a,b] \end{cases} \tag{2.40}$$

The estimator of the original integral would therefore be:

$$\left\langle \int_a^b f(x)dx \right\rangle = \frac{1}{N}\sum_{i=1}^{N} f(x_i)(b-a) = \bar{f}(b-a) \tag{2.41}$$

It is clear that the average of the function multiplied by the interval length is the integral itself. It is also possible to define the variance σ^2 of x [37]:

$$\begin{aligned}\sigma^2 &= \left\langle (h(x)-I)^2 \right\rangle = \left\langle h^2(x) \right\rangle - 2I\left\langle h(x) \right\rangle + I^2 \\ &= \left\langle h^2(x) \right\rangle - I^2 = [\int_a^b h^2(x)\varphi(x)dx] - I^2\end{aligned} \tag{2.42}$$

and an estimate of σ^2 is the empirical variance $\overline{\sigma^2}$:

$$\overline{\sigma^2} = \frac{1}{N-1}\sum_{i=1}^{N}(h(x_i)-\bar{I})^2 \tag{2.43}$$

It can also be demonstrated that $\overline{\sigma^2}$ is an unbiased estimator of σ^2, i.e.:

$$\left\langle \overline{\sigma^2} \right\rangle = \sigma^2 \tag{2.44}$$

and from this definition of the variance σ^2 it is possible to notice that the standard deviation σ is inversely proportional to $\sqrt{N}$. These MC simulations, also known as analog simulations, are quite slow to converge. It would be useful therefore to compare it with common numerical quadrature formulas used for numerical integration, such as the Newton-Cotes formulas, that select the points according to the following definition:

$$x_i = a + i\frac{b-a}{N} \tag{2.45}$$

As shown in Table 2.1, these quadrature formulas converge quickly, but only for problems with a limited number of dimensions. The convergence of MC methods on the other hand does not depend on the dimensionality of the problem, and for this reason they are typically useful for solving high-dimensionality problems where deterministic solvers also experience long calculation times. Neutron transport problems, which involve discretizing multiple variables (three for space, two for

Table 2.1 Newton-Cotes numerical quadrature formulas [37].

Quadrature	Points	Order	Convergence (k dimensions)
Trapezoid rule	2	1	$\frac{1}{\sqrt[k]{N^2}}$
Simpson's rule	3	2	$\frac{1}{\sqrt[k]{N^4}}$

direction, energy, and possibly time), fall into this category, making MC calculations competitive [37].

Another issue with MC methods is the challenge of simulating particles that travel far from the neutron source. In these cases, it is unlikely for a single particle to survive the random walk and score exactly where desired, therefore a large number of histories must be simulated to achieve reasonable statistical errors. However, in *analog* MC simulations (i.e. *unbiased* simulations), many of the generated particles may not contribute significantly to the desired outcome because they move further from the region of interest, or scatter to different energies. This issue is common in activation studies because some large, possibly activated components are far from the core, and therefore the neutron source. Components such as the head and bottom of the RPV or some internals may be too distant for the analog MC simulation to produce statistically significant results.

Non-Analog MC and Variance Reduction techniques

To address the issue previously described, *non-analog* MC calculations have been developed [49], [50], [51]. These involve the biased sampling of certain quantities while ensuring that the contributions are correctly weighted and do not compromise the physical validity of the results. In order to explain non-analog MC, let us assume the objective is the evaluation of the average value $< M >$ of the response function $M(\bar{r},E)$, which is non zero only for a specific region of the reactor. In analog MC, $< M >$ would be calculated in the following way:

$$\langle M \rangle = \int \int P(\bar{r},E)M(\bar{r},E)d\bar{r}dE \tag{2.46}$$

with $P(\bar{r},E)$ probability density function of the neutron distribution. In this case the analog game would sample particles according to the probabilities that characterize the physics of the system. In non-analog games, particles that contribute more to the response function $M(\bar{r},E)$ are sampled more frequently than particles that do not score where desired. An example is the vessel head: if the objective is the evaluation of the neutron flux at the top of the reactor, particles moving downwards would still consume computational resources without contributing to the response function i.e. scoring in the right place. In this same example, a non-analog game could be biased to enhance the transport of particles in the correct direction and progressively hinder it in the opposite one.

In order to maintain the physical meaning of the game, nevertheless, a weight W associated to a particle has to be introduced. This weight can be thought of as the number of physical neutrons represented by the simulated one. By adjusting the weights it is possible to bias the MC game in the desired way, achieving the same mean of the analog game.

Let us assume to be interested in the evaluation of the neutron flux in a certain volume V of the phase space and in a certain energy group g. For each group the average neutron flux in V would be calculated as:

$$\bar{\Psi}_{V,g} = \frac{1}{V}\int_g \int_\Omega \int_V \psi(\bar{r}, \hat{\Omega}, E) dV d\hat{\Omega} dE \tag{2.47}$$

In a biased MC game, this integral quantity would be approximated by the sum of the weighted contributions of the particles. For i particles entering V, the approximated flux would be:

$$\bar{\Psi}_{V,g} \approx \frac{\sum_i (W_i \cdot T_{l,g})}{V} \tag{2.48}$$

where $T_{l,g}$ is the path length traveled by the neutron in V in the energy group of interest (i.e. its track length contribution), while W_i is the previously introduced particle weight.

There are several variance reduction (VR) techniques based on the manipulation of statistical weights. One of the most common is known as *Weight-Window* (WW) [52], [53], [54]. This acceleration technique is a standard method frequently used in MC simulations, particularly for handling shielding problems. It is integrated into many software's internal routines and leverages the concept of importance previously introduced, which defines the relative weight of a particle's contribution to a specific response, in this case the neutron flux. The accelerated MC simulation is strategically adjusted to favor particle movement in regions characterized by increasing importance, thereby increasing their likelihood of contributing to the desired response.

Each particle is initially assigned a statistical weight, which is modified as the simulation progresses. When a particle enters a new region characterized by different importance, its weight is compared to the upper and lower limits associated with it. If the particle's statistical weight falls below the lower limit, its history may be terminated with a probability calculated as follows:

$$P = 1 - \frac{W}{W_{lo}} \tag{2.49}$$

where P is the probability of terminating the particle's history, W is the statistical weight of the particle and W_{lo} is the lower threshold for weight. If the particle survives, it continues its path, and its weight is recalculated as:

$$W_{new} = \frac{W_{old}}{1 - P} \tag{2.50}$$

where W_{new} is the new statistical weight, W_{old} is the old statistical weight and P is the probability of terminating the particle's history, calculated using (2.49). This process, known as "*Russian roulette*", allows the gradual removal of particles traveling in regions with low importance while maintaining the average statistical weight of the simulation.

When particles have a weight greater than the upper limit, they are divided into multiple histories through a second population control mechanism known as "*splitting*". The number of particles generated through splitting is calculated as follows:

$$a = \frac{W}{W_{hi}} \tag{2.51}$$

Where a is the theoretical number of particles resulting from the splitting procedure, W is the initial particle's weight and W_{hi} is the upper weight threshold.

As it is typically impossible for a to be an integer, the number of generated neutrons is the truncated integer value, with an additional particle potentially added with a probability expressed as follows:

$$P = a - trunc(a) \tag{2.52}$$

where P is the probability of generating an extra particle, a is again the theoretical number of particles resulting from the splitting procedure and $trunc(a)$ is the truncated integer. The weights assigned to the particles after the splitting operation are set to the maximum threshold W_{hi}.

While this process may appear complex for a single event, and the statistical weight of the single particle is altered, the average statistical weight is conserved. For instance, consider a scenario where there is a neutron with a statistical weight of 3 and an upper weight limit of 2. In this situation, the calculated value of a is 3/2, which results in 1.5. Since it is not possible to have fractional particles, the outcome of the splitting process would be one particle with the maximum allowed weight (in this case, 2), along with a second particle that has a 50% chance of being generated (1.5 - 1 = 0.5). If the second particle is indeed generated, its weight matches the upper limit as well. The same principle applies when dealing with a more extensive group of N neutrons, each with a weight of 3. The outcome of the splitting process in this case would be N neutrons, each with a weight of 2, and an additional $N/2$ neutrons, also with the maximum weight. Thus, the total number of resulting particles would be 1.5 times N, all having the maximum weight permitted. The minimum and maximum weight thresholds are determined based on the inverse of importance, which is usually calculated by internal software routines based on user input that defines the region toward which neutrons have to be accelerated. Some coefficients are often applied to the thresholds to create a "weight window" within which the technique operates. In Serpent 2, the MC code used in the framework of this thesis, the default weight window is set to $0.5I^{-1}$ - $2I^{-1}$, where I^{-1} represents the inverse of the previously calculated importance [55], [37]. This window ensures that the limits are not overly restrictive.

In Serpent 2, three methods for generating importance are envisioned and described in [55]:

1. Single detector
2. Multi detector
3. Global Variance Reduction

They can be effectively combined to achieve optimal results. The first two methods, single detector and multi detector, are quite similar in their approach. They enable the creation of regions with increased importance as defined by the user's selection of detectors. Particles are then accelerated in the direction of one or more detectors and gradually removed from opposing directions using the Russian roulette and splitting mechanisms as mentioned earlier. However, it is important to note that both single and multi-detector techniques have a requirement where a minimum number of particles must reach the detectors before the acceleration begins [55]. If the regions defined by the detectors are shielded or distant from the neutron source, it is possible that this minimum threshold may not be met, or that no particles reach the detectors at all, leading to a critical error and simulation failure. To address this challenge, an initial step may be introduced in the process, employing the Global Variance Reduction (GVR) technique. GVR is used to generate importance maps that progressively populate the entire geometry with particles [56]. After this global step, detector-specific acceleration may be implemented for the final transport calculation.

Variance reduction techniques based on the calculation of importance can be quite effective at accelerating the MC simulation convergence. The internal routine for the calculation of neutron importance in Serpent 2 is based on the solution of the adjoint transport problem using the Response Matrix Method, a deterministic technique which requires the subdivision of the analyzed geometry into spatially discretized subzones. Cellwise coupling coefficients between the subzones defined by the mesh are obtained from a conventional forward MC simulation instead.

The solution is based on the preservation of the particle balance in each cell along with the interface currents between each confining mesh cell, in order to couple the results. The mesh can be either regular or uneven, as the only prerequisites are that it covers the whole geometry and connectivity between the adjacent cells can be determined. This is essential to evaluate the cellwise inward and outward current vectors ($\mathbf{J}_n^{in}$ and $\mathbf{J}_n^{out}$), which consider the contribution of all the N_b connected boundary surfaces for the cell n.

$$\mathbf{J}_n^{in} = \begin{pmatrix} J_{n,1}^{in} \\ J_{n,2}^{in} \\ \dots \\ J_{n,N_b}^{in} \end{pmatrix} \tag{2.53}$$

$$\mathbf{J}_n^{out} = \begin{pmatrix} J_{n,1}^{out} \\ J_{n,2}^{out} \\ \dots \\ J_{n,N_b}^{out} \end{pmatrix} \tag{2.54}$$

These cellwise vectors are then used to determine the global inward and outward current vectors ($\hat{\mathbf{J}}_n^{in}$ and $\hat{\mathbf{J}}_n^{out}$), which contain information on currents for each of the N_c cells of the mesh.

$$\hat{\mathbf{J}}^{in} = \begin{pmatrix} \mathbf{J}_1^{in} \\ \mathbf{J}_2^{in} \\ \dots \\ \mathbf{J}_{N_c}^{in} \end{pmatrix} \tag{2.55}$$

$$\hat{\mathbf{J}}^{out} = \begin{pmatrix} \mathbf{J}_1^{out} \\ \mathbf{J}_2^{out} \\ \dots \\ \mathbf{J}_{N_c}^{out} \end{pmatrix} \tag{2.56}$$

Continuity of the currents at the cell interface is expressed using a topology matrix $\hat{\mathbf{T}}$ made of zeros and ones that maps the cellwise outward currents to the inward currents of the proper neighboring cell and essentially defines the geometry of the system, as its structure depends on the mesh type used.

$$\hat{\mathbf{J}}^{in} = \hat{\mathbf{T}}\hat{\mathbf{J}}^{out} \tag{2.57}$$

The coupling coefficients preserve the intracell particle balance and capture the physics of particle interactions in the cell, and are obtained via a forward MC simulation. They allow to solve for the interface currents between cells, coupling the local reaction rates to the global distribution. The intracell solution depends on two components. The first component is $J_{i,g,j,h}$, i.e. the current entering the cell through the boundary surface i and in the energy group g and exiting the same cell through a different surface j and in a different group h due to the interactions occurred in the cell. The second component is $J_{s,g,j,h}$, i.e. the current formed by source particles emitted in the cell in group g and that exit from the border surface j in group h after interacting. Many of the coupling coefficients depend on more than one index, therefore the following, more compact notation will be used: $k = N_g(i-1)+g$ and $k' = N_g(j-1)+h$, with N_g number of energy groups considered. The movement of particles through the cell is described by a matrix $\mathbf{A}$ of current transfer coefficients $\alpha_{k,k'}$, which are defined as the ratio between the outward current formed by particles that enter the cell in group g through surface i and exit in group h through surface j and the total inward current in group g through surface i, as expressed in Equation

(2.58):

$$\alpha_{k,k'} = \frac{J_{k,k'}}{J_k^{in}} \tag{2.58}$$

A essentially contains the probabilities of particle passing through the cell. In a similar way, source coefficients $\gamma_{g,k'}$ representing the probabilities that particles emitted in the cell in group g exit through surface j in group h are defined by the ratio between the appropriate current component and the total source of particles in group g in the cell, as expressed in Equation (2.59) and collected in a dediacted matrix Γ:

$$\gamma_{g,k'} = \frac{J_{s,g,k'}}{S_g} \tag{2.59}$$

The local cellwise response F is formed by two contributions, corresponding to the particles that entered the cell in group g through surface i (F_k) and those that were emitted in the cell in group g ($F_{s,g}$), as expressed in Equation (2.60).

$$F = \sum_k F_k + \sum_g F_{s,g} \tag{2.60}$$

The inward currents and source particles are coupled to the response by the ratios r between the response component considered, and either the total inward current in group g through surface i or the total source in group g, as shown in Equations (2.61) and (2.62):

$$r_k = \frac{F_k}{J_k^{in}} \tag{2.61}$$

$$r_{s,g} = \frac{F_{s,g}}{S_g} \tag{2.62}$$

The adjoint solution provides the contribution of inward currents and sources components with respect to user defined responses. The contributions are associated to the source and current importances that are used to determine the WW boundaries for the variance reduction scheme. The solution requires to determine additional cellwise coupling coefficients, that are obtained from the MC tallies. For example, inverse current response coefficients $r_k^\dagger$ are defined as the ratio between the contribution to the response given by particles entering in group g through surface i (F_k) and total result contribution in group g (F_g) minus the direct source contribution in the same group ($F_{s,g}$), as shown in Equation (2.63).

$$r_k^\dagger = \frac{F_k}{F_g - F_{s,g}} \tag{2.63}$$

These coefficients represent which fraction of the cellwise result contribution in group g comes form the inward currents from surface i in group g. These coefficients are stored in a matrix $\mathbf{R}^\dagger$ and are used to initialize the calculation for the adjoint current, similarly to what would be done with source coefficients for a forward calculation. The passage of particles through the mesh cell is described using inverse current transfer coefficients $\alpha^\dagger_{k,k'}$, i.e. the ratio between the outgoing current formed by particles that entered through surface i in group g and exited through j in group h ($J_{k,k'}$) and the total outward current component through surface j in group h ($J^{out}_{k'}$).

$$\alpha^\dagger_{k,k'} = \frac{J_{k,k'}}{J^{out}_{k'}} \tag{2.64}$$

These coefficients are stored in a matrix $\mathbf{A}^\dagger$ which describes the fraction of existing current components that originated from the inward currents. Similarly, a matrix $\Gamma^\dagger$ with the inverse source coefficients is created, representing the fractions of the outward currents that originated from the source.

The adjoint iteration is then initialized by the result scores distribution and inward current components are obtained using the inverse response coefficient matrices and the global responses previously calculated, as shown in Equation (2.65)

$$[\hat{\mathbf{J}}^{\dagger,in}]^{(l=0)} = \hat{\mathbf{R}}^\dagger(\hat{\mathbf{F}} - \hat{\mathbf{F}}_s) \tag{2.65}$$

Where $\hat{\mathbf{F}}$ is the array of the cellwise total result contributions and $\hat{\mathbf{F}}_s$ the array of the source contributions. Inward adjoint currents are mapped into the neighboring cells via multiplication with the inverse topology matrix $\hat{\mathbf{T}}^{-1}$, forming a distribution of outward adjoint currents as expressed in Equation (2.66)

$$[\hat{\mathbf{J}}^{\dagger,out}]^{(l+1)} = \hat{\mathbf{T}}^{-1}[\hat{\mathbf{J}}^{\dagger,in}]^{(l)} \tag{2.66}$$

which are subsequently passed through the cells using the matrix of inverse current transfer coefficients, as shown in Equation (2.67).

$$[\hat{\mathbf{J}}^{\dagger,in}]^{(l+1)} = \hat{\mathbf{A}}^\dagger[\hat{\mathbf{J}}^{\dagger,out}]^{(l+1)} \tag{2.67}$$

The resulting, new inward adjoint current distribution represents the starting point for the next iteration, until the convergence of the global solution. Once convergence is reached, the contribution per single particle, i.e. the importance, can be obtained for each group and incoming surface dividing the converged solution by the corresponding forward current, as expressed in Equation (2.68)

$$I_k = \frac{J_k^{\dagger,in}}{J_k^{in}} \tag{2.68}$$

although for most applications in VR the cell averaged importance is sufficient. The result contribution of sources are calculated with a similar procedure, considering both direct contributions to the tally from particles that never left the cells and contributions of source particles to the adjoint currents useful for the result, as expressed in Equation (2.69).

$$\hat{\mathbf{S}}^{\dagger} = \hat{\mathbf{F}}_s + \hat{\Gamma}^{\dagger}\hat{\mathbf{J}}^{\dagger,out} \tag{2.69}$$

The importances are then calculated dividing the source contributions with the corresponding source terms, as reported in Equation (2.70).

$$I_{s,g} = \frac{S_g^{\dagger}}{S_g} \tag{2.70}$$

This latter importance is the one used to evaluate the WW boundaries for Russian roulette and splitting for particles emitted inside the cells.

The methodology can be applied to one-, two- or three-dimensional problems considering the multigroup subdivision of the energy as well, and can be applied to either neutrons or photons. More details on the VR technique implemented in the software are available at [55] and [57].

2.5 Modeling approach for activation calculations

As previously introduced, activation calculations are necessary for evaluating the impact of the neutron flux on structural materials. The specific activity of these materials plays a significant role in waste classification and dose rate calculations. In principle, activation calculations can be performed using MC techniques, as the generation of radioactive nuclides results from reactions between neutrons and parent nuclides, therefore, the process can be described in terms of reaction rates. However, a more common and efficient approach is to use deterministic methods.

This approach involves solving sets of *Bateman's equations*, which describe the production and decay of radioactive nuclides.

The production of a specific isotope primarily occurs due to interactions between a parent nuclide and the neutron flux, such as neutron capture, or it can result from the decay of other species. Similarly, the removal of isotopes can be due to decay or transmutation caused by interactions with neutrons. Therefore, a coupled set of equations can be constructed to describe the overall changes in various isotope populations exposed to a neutron flux over a specific period of time. In the absence of a neutron flux, it is possible to observe the evolution of the material composition, which is solely governed by radioactive decay. This capability allows for the prediction of the future specific activity of certain components, facilitating better planning of decommissioning operations, especially if deferred dismantling is the chosen strategy.

For the activation calculations in the context of this thesis, the software used is *FISPACT-II*. FISPACT-II serves as a multi-physics, inventory, and source-term code developed by the UK Atomic Energy Authority (UKAEA). It encompasses an extensive array of sophisticated predictive simulation techniques, offering temporal and spectral capabilities for various nuclear particles, including neutrons and charged particles such as electrons or protons. Much akin to ORIGEN [58], FISPACT-II finds its primary utility in solving sets of Bateman equations, addressing inventory calculations, and encompassing phenomena like material activation, transmutation, fuel depletion, and radioactive decay. FISPACT-II reads modern data libraries in ENDF format and certain legacy libraries like EAF. The current version utilizes the latest TALYS-based TENDL evaluated nuclear data libraries. Additional information on these computational tools is available in [59].

FISPACT-II models materials as homogeneous and infinite, eliminating the need for spatial discretization, making the model essentially dimensionless. The mathematical treatment reduces to solving a set of ordianary differential equations (*ODE*), which have the following form:

$$\frac{dN_i}{dt} = \sum_j (\lambda_i^j + \gamma \sigma_i^j \Psi(t)) N_j \tag{2.71}$$

in cases where $j \neq i$. N_i is the number of nuclides i at time t, Ψ is the total neutron flux, λ_i^j represents the decay constant of nuclide j producing i, γ represents the yield if needed, e.g. in case of fission, and σ_i^j represents the reaction cross section for reactions on j producing i. In the case of $j = i$, Equation (2.71) assumes the following form:

$$\frac{dN_i}{dt} = (-\lambda_j^j - \sigma_j^j \Psi(t))N_j \tag{2.72}$$

where λ_j^j represents the total decay constant of nuclide j and σ_j^j represents the sum of the cross sections that induce transmutations on j, such as absorption or (n,2n), for instance.

As reaction cross sections are dependent on the energy of incoming neutrons, and FISPACT employs the multigroup approximation requiring multigroup fluxes and cross sections, with this computational tool it becomes necessary to compute an *effective cross section* that accurately represents the physics of the transmutation process [4], [32]. This procedure is commonly referred to as "*collapsing*", and it involves the weighting of the original cross section contributions with the energy spectrum of incoming particles [60]. This allows for the determination of a single average value for each energy group:

$$\sigma_i^j = \frac{\sum_k \tilde{\sigma}_i^j(E_k)\Psi_n(E_k)}{\sum_k \Psi_n(E_k)} \tag{2.73}$$

where $\tilde{\sigma}_i^j(E_k)$ is the cross section for the reaction on j producing i in the energy group k and $\Psi_n(E_k)$ is the integrated flux in the same energy group. To consider the whole spectrum, both sums are over all the k energy groups considered. It is important to note that in this modeling approach the imposed neutron flux is not modified by the changing composition of the material. This approximation implies that the cross sections and decay rates in (2.71) do not depend on the nuclide number, allowing to rewrite the equation as:

$$\frac{d\mathbf{N}}{dt} = A\mathbf{N} \tag{2.74}$$

The size of matrix A depends on the amount of possible nuclides considered, i.e. the nuclide index used in the calculation. If, for example, the index from EAF-2010 [61] is used, A would have dimensions 2234 x 2234, as the index is formed by 2233 nuclides, plus the "sink" nuclide which accounts for reactions that generate daughters not present in the index. A is independent of N and is piecewise constant in time, as it assumes a constant flux within each time interval. This is required by the solution method employed by FISPACT, although in general Equation (2.74) does not require these assumptions. Furthermore, it is sparse, facilitating rapid calculations due to the limited number of non-zero elements out of the almost 5 million possible, which depends on the specific problem under analysis. In cases where actinides are not significant and fission can be disregarded, such as in the activation calculations of structural materials, the maximum number of non-zero elements is approximately 42,000, a considerable reduction from the 120,000 that includes actinides. During cooling periods, when the primary transmutation mechanism is radioactive decay, this number is further reduced to 5,000.

It is important to note that the subdivision of the neutron flux in different energy bins when performing the transport calculations should be treated carefully, as the energy subdivision should match the one of the available libraries used by FISPACT-II in the activation calculation. It would be possible to convert the neutron flux computed with any energy subdivision into the correct grid, but the user manual advises against this procedure. For instance, neutron flux energy spectra calculated with lower resolution than required, although maybe easier to compute, would not be able to provide the same amount of information as a spectrum with the correct amount of energy bins. The conversion procedure for low resolution spectra, essentially, cannot generate any new piece of physical information compared to the original spectrum, and higher resolution spectra are more useful employed as they are. The suggestion is therefore to use an appropriate energy bin density, comparable to the one of the nuclear data library employed. For this reason, and to assure a reasonable level of accuracy, the neutron flux energy spectra were all evaluated using 709 energy groups, matching the TENDL libraries used in the framework of this study.

FISPACT, using the pathway analysis, is able to provide an estimate of the uncertainties related to the calculated quantities, such as decay heat or dose rate for example, the latter of which has been evaluated in some cases in the framework of this thesis [60] [62].

Let Q be a radiological quantity and S_t a set of target nuclides, where

$$Q = \sum_{t \in S_t} q_t \tag{2.75}$$

The uncertainty ΔQ is given by

$$(\Delta Q)^2 = \sum_{t \in S_t} \left(\frac{\Delta N_t}{N_t} \right)^2 q_t^2 \tag{2.76}$$

where N_t is the number of atoms of the target nuclide t generated from the initial inventory and ΔN_t is the error in N_t. ΔN_t can be computed using the inventory of pathways that lead to nuclide t and the fractional squared error Δ_{tp}^2 in the number of atoms of the target nuclide t that formed along the pathway p to that target. It is possible to write the set of pathways leading to target t as

$$S_p = (\cup_{a \in S_{sa}} S_a) \cup S_o \tag{2.77}$$

where S_a is the subset of the pathways where the pathway begins from the fission of an actinide a, S_o is the set of all other pathways and S_{sa} represents the subset of source nuclides that are actinides inside the larger source set S_s. The formula used to evaluate ΔN_t is

$$(\Delta N_t)^2 = \sum_{p \in S_o} \Delta_{tp}^2 N_{tp}^2 + \sum_{a \in S_{sa}} \left(\sum_{p \in S_a} |\Delta_{tp}| N_{tp} \right)^2 \tag{2.78}$$

where N_{tp} is the number of atoms of target t that are formed along the path p to that target. Δ_{tp}^2, i.e. the fractional squared errors, are calculated using the formula

$$\Delta_{tp}^2 = \sum_{e \in S_e} \sum_{r \in S_r} \left[\frac{R_r (\frac{\Delta \sigma_r}{\sigma_r})}{R_e} \right]^2 + \sum_{e \in D_e} \left[\frac{\Delta \tau_e}{\tau_e} \right]^2 \tag{2.79}$$

where S_e is the set of edges on the pathway p, S_r is the set of reactions on the edge e, R_r is the pulse averaged reaction rate of reaction r and R_e is the total pulse averaged reaction rate on edge e. The ratio $\frac{\Delta \sigma_r}{\sigma_r}$ is the fractional uncertainty in the cross section for the reaction r and the ratio $\frac{\Delta \tau_e}{\tau_e}$ is the fractional uncertainty in the half-life of the parent nuclide on the edge e. D_e is the set of edges on pathway p where the parent nuclide is long-lived or where the parent is short-lived and the daughter nuclide is the target nuclide of the path. More in detail, a nuclide is considered short-lived if its half-life is less than the time interval of the irradiation pulse sequences. For each edge, the total reaction rate R_e is expressed as

$$R_e = \sum_{r \in S_r} R_r \tag{2.80}$$

For the evaluation of R_r let us consider J time intervals in the irradiation phase and let Δt_j be the time interval $j \in [1,J]$ characterized by a neutron flux Ψ_j. Moreover, there are I collapsed cross sections, with cross section $i \in [1,I]$ being the value used in pulses $j = J_i \dots J_i + 1$ ($J_1 = 1$ and $J_{I+1} = J$). R_r can therefore be written as

$$R_r = \left(\sum_{i=1}^{I} \sigma_r^i \sum_{j=J_i}^{J_i+1} \Psi_j \Delta t_j \right) / T_J \tag{2.81}$$

with

$$T_J = \sum_{j=1}^{J} \Delta t_j \tag{2.82}$$

In case of fission, the cross section σ_r^i is replaced by the product $\sigma_r^i f_r$ where f_r is the fission yield for the reaction product corresponding to the daughter nuclide on the edge considered.

To summarize, FISPACT-II relies on five key pieces of information to perform an activation calculation effectively:

- The precise material composition, accounting for the presence of impurities that exert a notable influence;
- The energy-integrated neutron flux, conveying information about neutron density;
- The flux spectrum, which provides information on the energy distribution of the neutron flux and is essential for the collapsing procedure;
- The irradiation time and, if applicable, the subsequent cooling time;
- Nuclear data sourced from external libraries.

The neutron flux value and its energy spectrum represent the primary outcomes of the MC calculations. Combining these results with the missing information enables the assessment of residual activation in various sections of the Trino reactor.

2.6 Simulation approach adopted for the residual activation assessment

The approach chosen in this work for assessing the residual activation of the Trino reactor combines different techniques. Similar schemes have been developed in the past to analyse activation phenomena [63], [64], [65], [66]. Recognizing that activation phenomena result from a complex interplay of factors, the problem has been divided into three, potentially four separate steps:

1. **MC Simulation in Criticality Mode**: in the first step, a MC simulation is performed in *criticality mode*, whose primary objective is to generate the neutron source term required for the subsequent steps. This phase involves creating a high-fidelity geometrical and neutronic model of the reactor, which will be used in the second step as well;
2. **MC Simulations with Variance Reduction**: in the second set of MC simulations, executed in *external source mode* and employing VR techniques, the previously computed neutron source is employed. These simulations accelerate neutron transport toward the selected regions under analysis, where integral neutron fluxes (i.e., neutron fluxes integrated over the entire energy range) and/or neutron flux energy spectra are computed;
3. **Activation Calculations**: the final set of calculations - activation - is conducted using a deterministic approach. The objective is to evaluate the residual activation and/or contact dose rates in the chosen points;
4. **Validation (optional)**: if specific activity measurements are available, a fourth step can be defined comparing them with computational results. This additional phase allows for the validation of the calculation scheme.

A schematic view of the calculation scheme proposed is reported in Figure 2.1. Each step will be presented and discussed more in detail in Chapter 3.

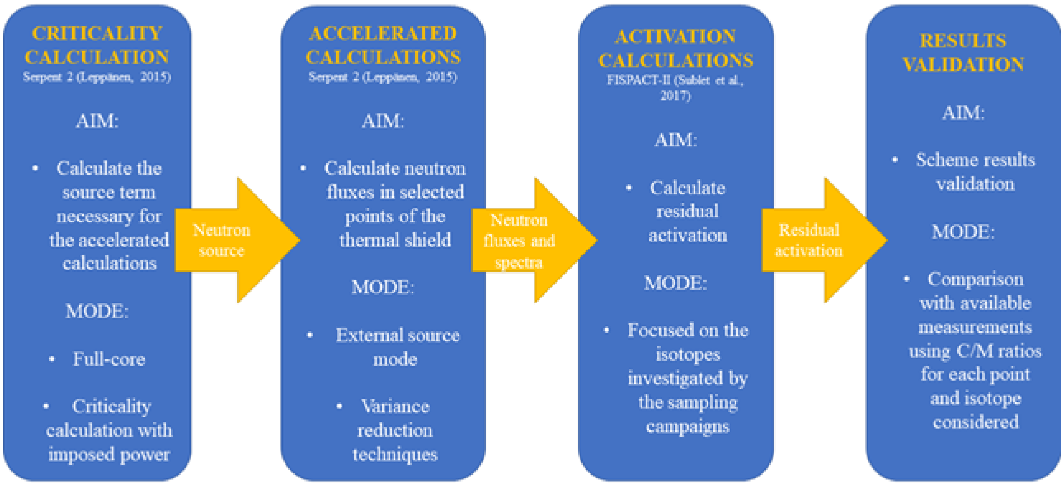

Fig. 2.1 Proposed calculation scheme.

The proposed methodology has been developed and applied initially to analyze the thermal shield of the Trino PWR, a component that was removed from the reactor at the conclusion of its first operating cycle. A limited number of residual activation measurements were obtained from the shield, and these measurements have played a crucial role in validating the computational model. This validation step is especially valuable due to the complex nature of residual activation and the long computational chain, where uncertainties may be notably significant. The ultimate objective, following this initial validation phase, was to expand the residual activation analysis to the RPV, which will be discussed in Chapter 4. It is worth noting that the RPV has a more complex irradiation history, spanning all nine operational cycles, which contributes to its residual activation, encompassing all modifications introduced in terms of geometry and power levels, therefore the scheme required a few adaptations which will be presented in Chapter 4 as well. Using this combination of continuous MC transport simulations followed by FISPACT activation calculations is a modelling choice, as in principle the same kind of analysis could be performed using different combinations of tools. It would be possible, for instance, to calculate the neutron flux energy spectra and the neutron fluxes using deterministic tools. Another strategy that could be used is to perform all calculations using MC, evaluating the reaction rates in the structural material. The choice of FISPACT stemmed also from the fact that the tool was already known in Sogin.

Chapter 3

Monte Carlo calculation scheme to support the decommissioning of PWRs

In this Chapter, the development of the calculation scheme is discussed. While its general concept can be applied to any component facing the neutron flux, it was initially designed to assess the residual activation of the thermal shield, as previously introduced. Notably, there are two separate datasets available comprising measurements of residual activation sampled from the shield, therefore in this case, the valuable fourth validation step could be included. The validation was conducted by calculating the C/M ratio, which represents the ratio between the calculated specific activity and the measured one. The closer the ratio is to 1, the more accurate the comparison.

The first dataset, dating back to 1969, reports mainly the residual activation due to ^{60}Co and ^{54}Mn in specific locations along the vertical z-axis of the component's internal surface (13 points), with 2 more points sampled on the external surface. Samples were collected around two years after reactor shutdown, so the contribution of ^{54}Mn, which decays rather quickly with a half-life of just 312 days, remains significant.

The second dataset, from 1992, focuses on two points at a different angular coordinate, one on the internal and one on the external surface, and considers contributions to the specific activity from ^{60}Co, ^{55}Fe, ^{59}Ni, and ^{63}Ni, expanding the range of analyzed isotopes. Focusing solely on the thermal shield also allows for a reduction in the operating history that needs to be reconstructed, limited to the first operating cycle.

3.1 Step 1: Critical simulation for neutron source generation

The first Monte Carlo simulation, conducted in *criticality mode*, is intended to assess the neutron source term. The source file generated by this initial step contains all the pertinent information regarding the neutron source points, encompassing spatial coordinates, energy, flight direction, and statistical weights. This file is used in the second step to compute the accelerated transport of neutrons generated at the source points, directing them towards the regions of interest by applying the previously discussed VR techniques. It is worth noting that in Serpent 2, these techniques are designed to be used exclusively in external source mode [55].

A comprehensive 3D geometrical and neutronic model of the reactor was created using the plant data provided by Sogin. This model encompasses the RPV, the internal stainless-steel liner of the RPV, and all the RVIs, as depicted in Figure 3.1. Each component is modeled with detailed information sourced from technical drawings, even including unique features of this early 1960s design, such as the cruciform fuel followers of the control rods. The control rods are represented in their extracted state from the core, with the followers modeled as inserted, simulating nominal full power operation at 870 MW$_{th}$. This nominal power has been chosen as, at the time of the analysis, no other information on the operating power of the reactor for the first few cycles was available. It is also the reference one used in Sogin's previous calculations. It was found only much later during the project that the reactor operated at 825 MW$_{th}$ until the fourth cycle, therefore the power was updated for evaluations made after the thermal shield analysis. This is the good example of the difficulties encountered working with legacy data, as previously mentioned in Section 2.2. The thermal shield, formed by a stainless-steel hollow cylinder approximately 7.5 cm thick, is positioned in the region between the core barrel and the RPV at core height. Fuel enrichments and structural material compositions were provided by Sogin, with the latter originally obtained through a combination of neutron activation analyses of unirradiated samples, data from literature, and certifications from the materials producer, as detailed in Appendix B. No boron is assumed to be dissolved in the coolant, as a representative concentration proved to be difficult to determine. For the analysis of the thermal shield, the fuel was considered fresh, i.e. no burnup calculations were performed. This is an approximation, as during fuel depletion the fission source may flatten radially, causing increased neutron production in the periphery of the core towards the end of the cycle. On the other hand, the depleted fuel tends to be more absorbing, offsetting at least partially this phenomenon. This aspect was also updated for evaluations made after the thermal shield analysis.

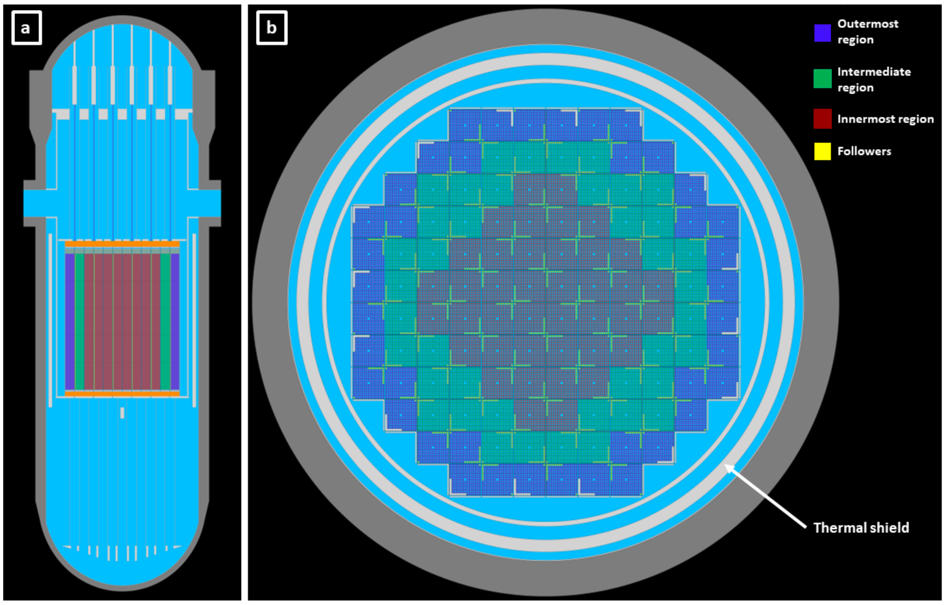

Fig. 3.1 (a) Vertical cross section and (b) horizontal (core midplane) cross section of the reactor. The fuel of different composition is represented with different colors for clarity. Fuel followers are represented with a fourth different color, although sharing the same fuel enrichment as the innermost region.

The modeled fuel pattern, visible in Figure 3.1 as well, features three concentric regions, with increasing enrichments from the center to the periphery of the core. This high-leakage fuel pattern resulted in a significant irradiation of the thermal shield, despite its presence in the reactor for only one operating cycle. In particular, the control rod cruciform followers, constructed from fuel rods themselves, share the same enrichment as the innermost region. The fuel temperature assumed for the calculation is 1144 K and the water temperature is 547 K. The cross sections used in the MC simulations belong to the JEFF-3.1.1. Nuclear Data Library [67]. The simulation was performed using 100000 neutrons per generation, with 1000 active generations and 50 inactive generations.

3.2 Step 2: External source simulations for accelerated transport and application of variance reduction techniques

The second phase in the calculation process using Serpent 2 is the propagation of neutrons from the reactor core to the surrounding thermal shield. This step is needed to assess the integral neutron flux (i.e. the neutron flux integrated across all energies) at specific locations within the component and to acquire the necessary neutron flux energy spectra for the subsequent activation analysis. Given that this stage involves neutron transport through several centimeters of water and, in certain instances, stainless steel, the challenge of obtaining statistically meaningful data in shielded regions becomes relevant. In addressing this challenge, VR techniques are employed in this step to accelerate the movement of neutrons generated within the core toward the adjacent structures. The parameters for the VR simulations are the same as in the critical case for what concerns the temperatures and libraries used, but 150 million particles are used in external source mode. The GVR iterations are performed until the entire geometry is populated with some neutrons before switching to detector-specific VR.

To evaluate the integral neutron flux, a collection of 17 small spherical void detectors with a radius (r) of 1 cm has been defined. These detectors employ the track length estimator for flux estimation. This estimator was chosen in anticipation of the future analysis of the RPV liner, which envisages detectors quite far from the source, e.g. close to the reactor head and bottom. The track length estimator is suggested in the Serpent2 manual for regions located far or isolated from the active source, as they already suffer from poor statistics.The selected measurement points align with those designated for the sampling campaigns and are situated either on the inner or outer surface of the shield. Their respective coordinates are detailed in Table 3.1, with the reference point $z = 0$ cm denoting the core's active zone's midpoint, and $\theta = 0°$ corresponding to the midpoint along one of the core's edges, as illustrated in Figure 3.2.

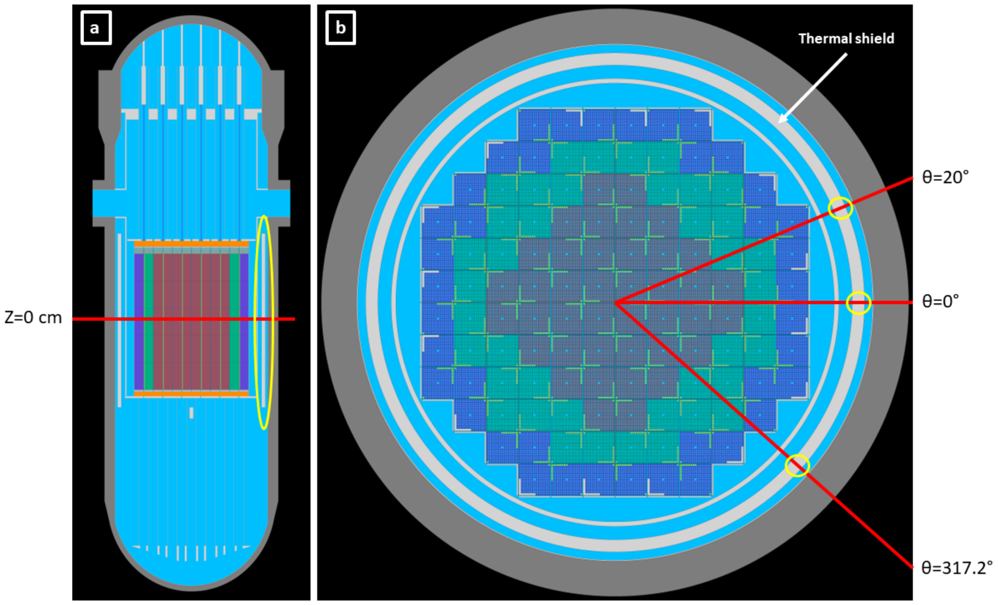

Fig. 3.2 (a) Vertical cross section and (b) horizontal (core midplane) cross section of the reactor. The detector/sample regions on the thermal shield are highlighted.

Table 3.1 Angular (θ) and axial (z) coordinates of the investigated points of the thermal shield.

$\theta/°$	z/cm	Inner surface/outer surface
0	172.35	Inner surface
0	134.35	Inner surface
0	102.35	Inner surface
0	72.35	Inner surface
0	39.35	Inner surface
0	13.35	Inner surface
0	12.35	Inner surface
0	12.35	Outer surface
0	-21.65	Inner surface
0	-53.65	Inner surface
0	-93.65	Inner surface
0	-134.65	Inner surface
0	-170.65	Inner surface
20	12.35	Inner surface
20	12.35	Outer surface
317.2	12.35	Inner surface
317.2	12.35	Outer surface

Preliminary calculations conducted at multiple locations on the inner surface of the thermal shield suggested that, for the majority of the examined points, there is negligible variation in the normalized neutron flux energy spectrum concerning both the axial (z) and angular (θ) coordinates. This consistent behavior can likely be attributed to the shield's close proximity to the reactor core, as evidenced in Figures 3.3 and 3.4. These figures compare spectra at different heights and angular positions with the spectrum integrated over both coordinates. Notably, the graphs closely overlay one another. Hence, to explore the residual activation at most of the surveyed locations, two integrated spectra are computed, one for the inner surface and one for the outer surface of the shield. The integrated spectra were obtained using a ring-shaped detector characterized by height and thickness equal to the sphere detectors' diameter. Integrating over θ enhances the statistical treatment of neutrons, as the general lower noise results particularly useful for both very high and low-energy neutrons. However, it is necessary to note two exceptions: the points situated at the extreme top and bottom of the shield exhibit slightly different spectra due to localized conditions, which will be discussed in more detail in Section 3.3.4.

In this scenario, the influence of the radial coordinate (r) on the neutron flux energy spectrum becomes significant. The shield's thickness plays a crucial role in shaping the neutron flux energy distribution, as illustrated in Figure 3.5. This figure provides a comparison of the integral neutron flux energy spectra for the inner and outer surfaces of the thermal shield, highlighting the particularly higher thermal peak in the inner surface spectrum.

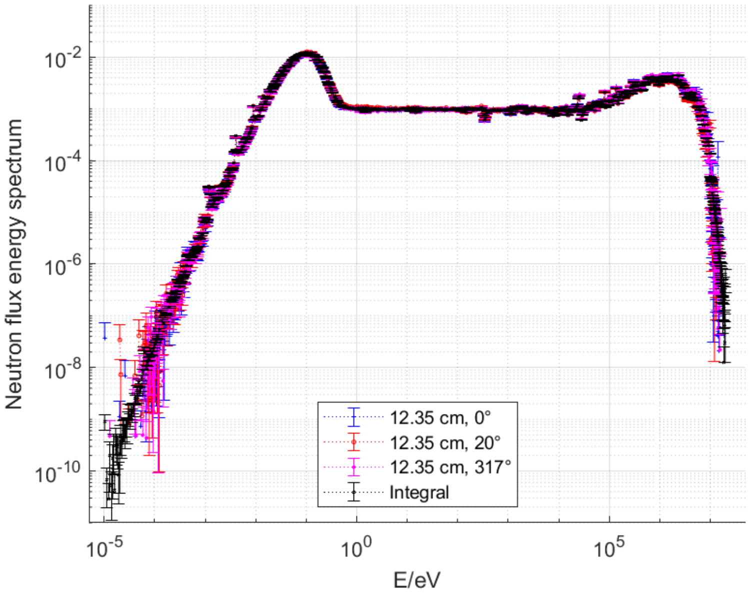

Fig. 3.3 Local neutron flux energy spectra in lethargy scale as a function of the energy E on the internal surface of the shield at different angular locations compared with the integral spectrum. All the spectra overlap for most energies, but in the high and low energy regions the integral spectrum is better defined.

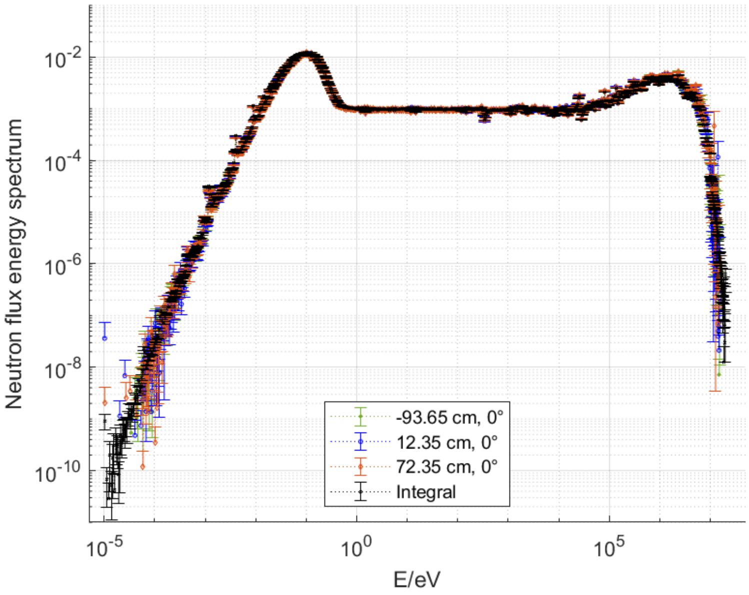

Fig. 3.4 Local neutron flux energy spectra in lethargy scale as a function of the energy E on the internal surface of the shield at different axial locations compared with the integral spectrum. All the spectra overlap for most energies, but in the high and low energy regions the integral spectrum is better defined.

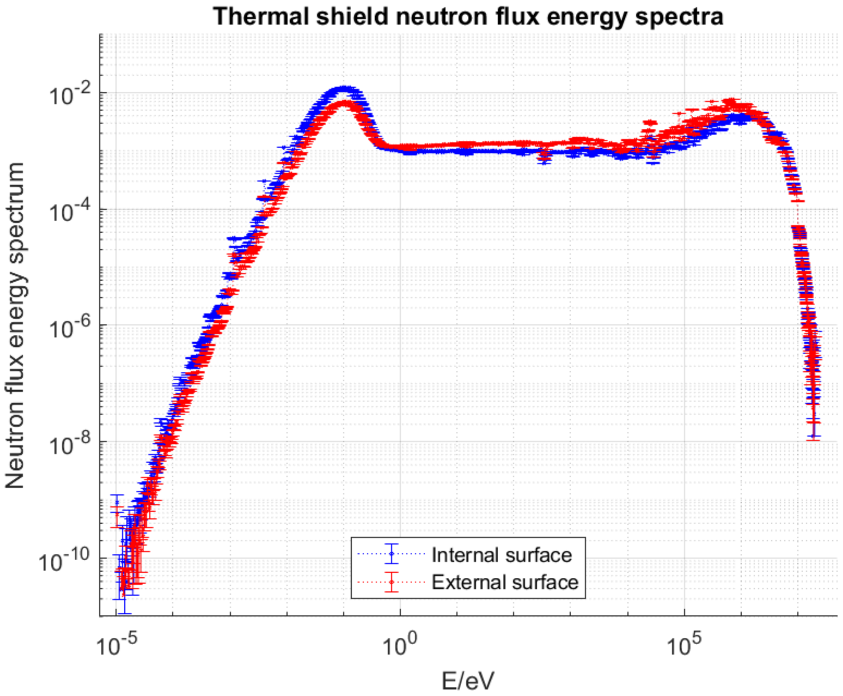

Fig. 3.5 Integral neutron flux energy spectra in lethargy scale as a function of the energy E on the internal and external surface of the thermal shield.

The acceleration model for the integral flux is customized to the specific objective, enabling the separate acceleration of particles toward distinct regions with varying angular coordinates and heights. This approach prevents the simultaneous acceleration of particles in too many different directions, which could be counterproductive. A qualitative importance map, illustrated in Figure 3.6, serves as an example. This map was specifically generated for the detector situated at the lower section of the internal surface of the shield, precisely at coordinates $\theta = 0°$ and $z = -170.65$ cm.

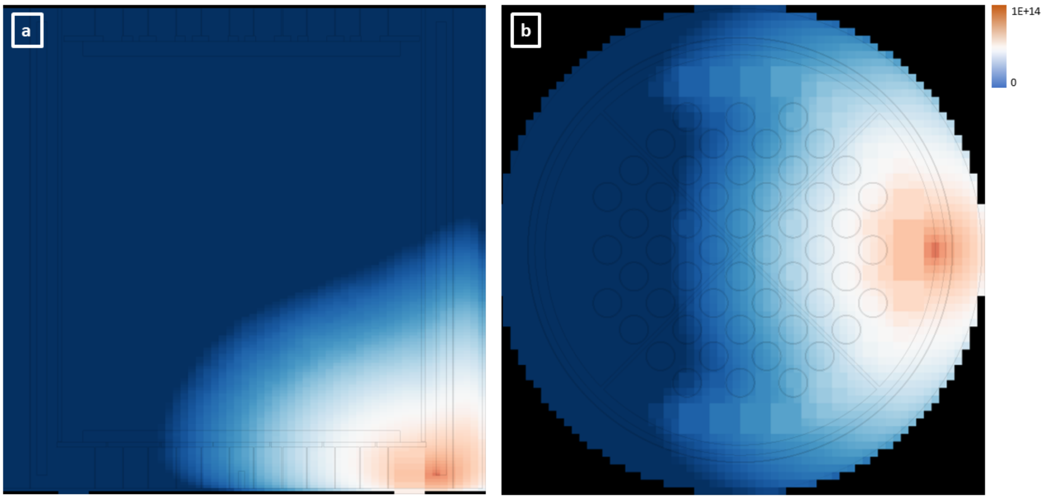

Fig. 3.6 Neutron importance, evaluated by Serpent 2 for the acceleration scheme, for (a) a *xz* section and (b) a *xy* (shield bottom) section of the central part of the reactor. The warmer the color, the higher the cell importance. As can be seen from both pictures, the importance map is tailored to the specific detector selected, in order to enhance the neutron transport in the desired direction.

3.3 Step 3: Activation calculations

The third step of the calculation scheme encompasses a series of simulations designed to assess the residual activation of the specified set of points belonging to the thermal shield. The necessary data introduced earlier will be briefly discussed in the subsequent Sections.

3.3.1 Detailed material compositions, including impurities

Structural materials often contain impurities that warrant attention. The ^{59}Co present in carbon and stainless steels is of particular concern, as it can be transmuted into ^{60}Co when exposed to a thermal neutron flux. Its decay emits strong gamma rays, therefore it is a crucial nuclide to consider for radiation protection purposes during the development of decommissioning plans. Historically, controlling this impurity during the manufacturing of reactor components was often not a top priority, since it does not affect the mechanical or thermal properties of the alloy, resulting in significant variation in trace cobalt amounts in steels used for different plants. As previously mentioned, The detailed composition of the stainless steel used in the framework of this thesis is reported in Appendix B.

3.3.2 Reconstructed irradiation history and decay time

To accurately assess the irradiation time, knowledge of the operational history of the reactor cycle under investigation is indispensable. A simplified operational history, typically comprised of intervals at constant power levels, is usually reconstructed based on plant data. This process can be challenging if the reactor experienced intermittent operation or operated at various power levels, as is the case with the initial operating cycle of the Trino reactor (see Figure 3.7).

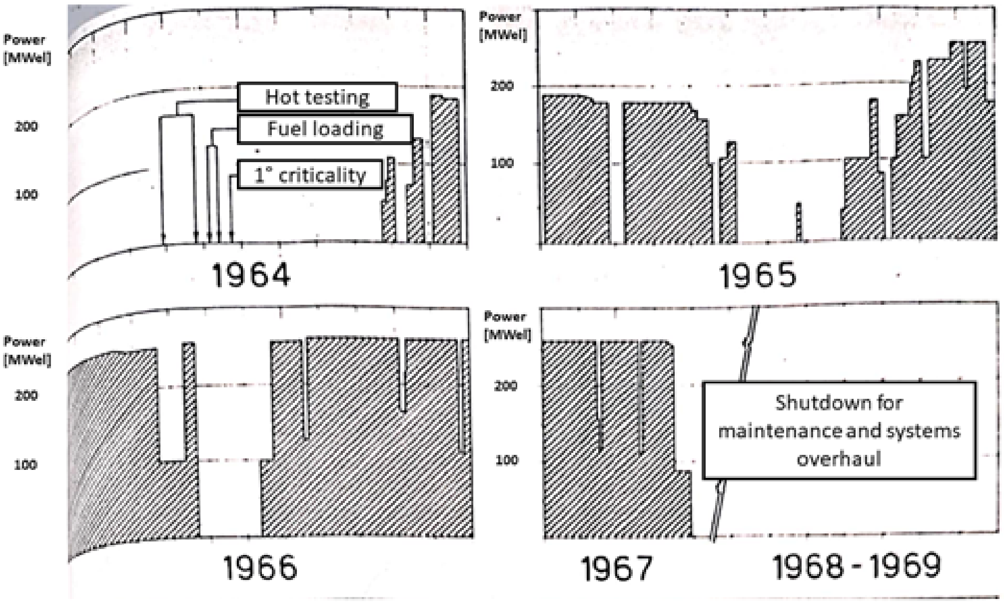

Fig. 3.7 First operating cycle of the Trino reactor [26].

In the context of this study, the simplified irradiation history employed is based on the recommendation from Sogin documentation [68] and is outlined in Table 3.2. The power ratios $\frac{P}{P_{max}}$ were used in the activation calculation to scale the flux used for the irradiation. This history comprises three distinct irradiation periods, each operated at a different power level, separated by two shutdown phases. The decay time, which is the duration between the conclusion of the cycle and the measurement of residual

Table 3.2 Simplified irradiation history used to reconstruct the first operating cycle of the Trino reactor. The length t of the steps is expressed in days.

Interval	From	To	t/d	$\frac{P}{P_{max}}$
1	21/10/1964	06/06/1965	225	0.56
2	07/06/1965	31/08/1965	87	0
3	01/09/1965	20/05/1966	260	0.75
4	21/05/1966	11/07/1966	53	0
5	12/07/1966	28/04/1967	295	0.89

activation, is necessary to consider the reduction in activity due to radioactive decay. This study takes into account two distinct decay times, aligning with the sampling campaigns conducted in August 1969 and February 1992:

- For the first dataset: 28/04/1967 – 1/08/1969
- For the second dataset: 28/04/1967 – 06/02/1992

3.3.3 Nuclear data

Activation calculations demand a substantial volume of nuclear data. Depending on the study's objectives, cross section data for various reactions and decay constants for numerous nuclides may be required. This step in the analysis of the thermal shield adopts the TENDL-2017 nuclear data library [69]. The primary reactions of interest, based on available measurements, are those contributing to the production of the aforementioned isotopes: ^{54}Mn, ^{55}Fe, ^{59}Ni, ^{60}Co and ^{63}Ni. It is worth noting that ^{55}Fe and ^{54}Mn, although valuable for assessing the scheme's performance, are not expected to be particularly relevant for the Trino reactor's decommissioning. This is due to the significant time passed since the shutdown in 1987 and their short half-lives of 2.74 years and 312 days, respectively [70], [2].

3.3.4 Neutron flux energy spectra and integral neutron flux

The neutron flux intensity and its energy distribution represent the final two parameters needed for conducting activation calculations. Differences in the distance from the source and the presence of various materials along the neutron path can result in distinct energy distributions in the neutron flux. In the case of the thermal shield, the neutron flux energy spectrum generally exhibits uniformity along angular and axial coordinates for the majority of the analyzed points, with the exception of two points. This uniformity could be attributed to the thermal shield's proximity to the neutron source. By integrating along these coordinates, a more comprehensive description of the neutron flux energy distribution is achieved, especially in the low-energy ($E \leq 0.001$ eV) and high-energy ($E \geq 1$ MeV) regions. The latter, in particular, holds significance for assessing the production of ^{54}Mn, which solely results from (n,p) reactions with fast neutrons involving ^{54}Fe. A poorly defined spectrum in the fast neutron region, such as that caused by inadequate statistical data, could lead to less accurate predictions of the residual activation linked to this isotope.

The two previously mentioned points that display slightly different spectra are situated at the very top ($z = 172.35$ cm) and bottom (z = -170.65 cm) of the shield. In these regions, the spectra differ somewhat from the rest of the component. This disparity arises from the varying proportions of water and steel in the surrounding volumes due to the shield's geometry and the specific sampling point selections.

Upon comparing the integral and local spectra, it becomes evident that employing the latter would imply a higher ^{60}Co production compared to the integral spectrum due to the elevated thermal peak. While both the integral and local spectra are well-defined in the thermal region, the local spectra encounter statistical uncertainties in the fast region, as illustrated in Figure 3.8.

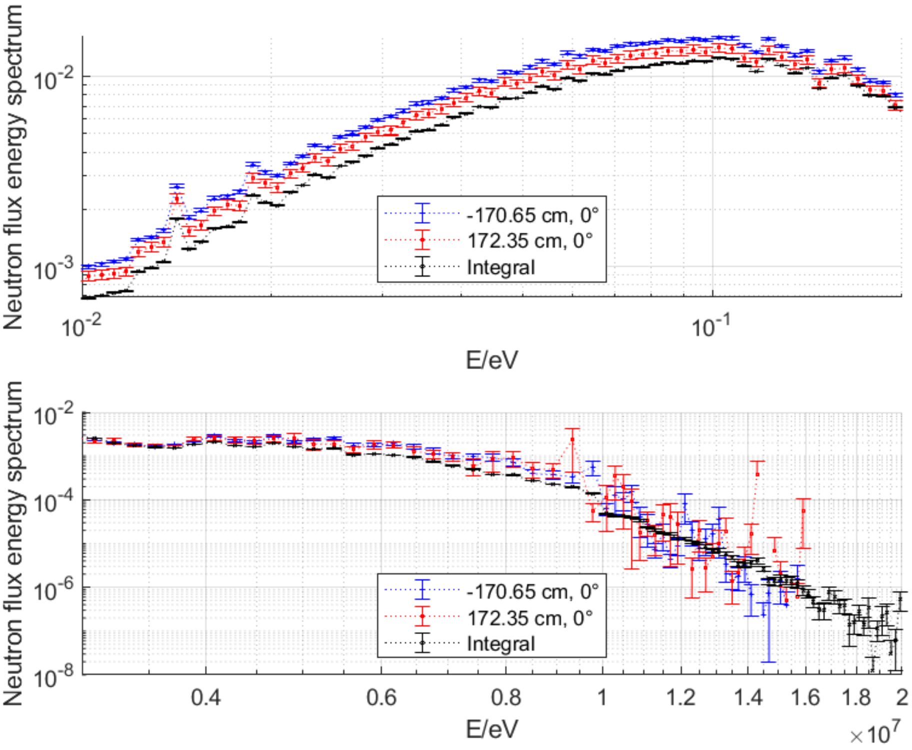

Fig. 3.8 Thermal (top) and fast (bottom) local neutron flux energy spectra in lethargy scale as a function of the energy E of the points at the top and bottom of the shield compared with the integral spectrum.

While the estimation of residual activation attributed to ^{60}Co remains reliable when calculated using local spectra, the same level of confidence does not apply when dealing with ^{54}Mn, as its calculation is sensitive to the input spectrum, including its statistical uncertainties. Given the greater significance of ^{60}Co in the decommissioning process compared to ^{54}Mn, local spectra were utilized for these two specific points in the activation calculation. This approach provides a more precise assessment of ^{60}Co that accounts for local effects, even if it results in a less reliable ^{54}Mn evaluation. For all the other points, employing the integral spectrum does not substantially impact the accuracy of the ^{60}Co estimation. This is because the thermal peak of ^{60}Co coincides with that of the local spectra. Simultaneously, it enables a more precise evaluation of ^{54}Mn, thanks to the reduced uncertainties in the fast neutron region, as illustrated in Figure 3.9.

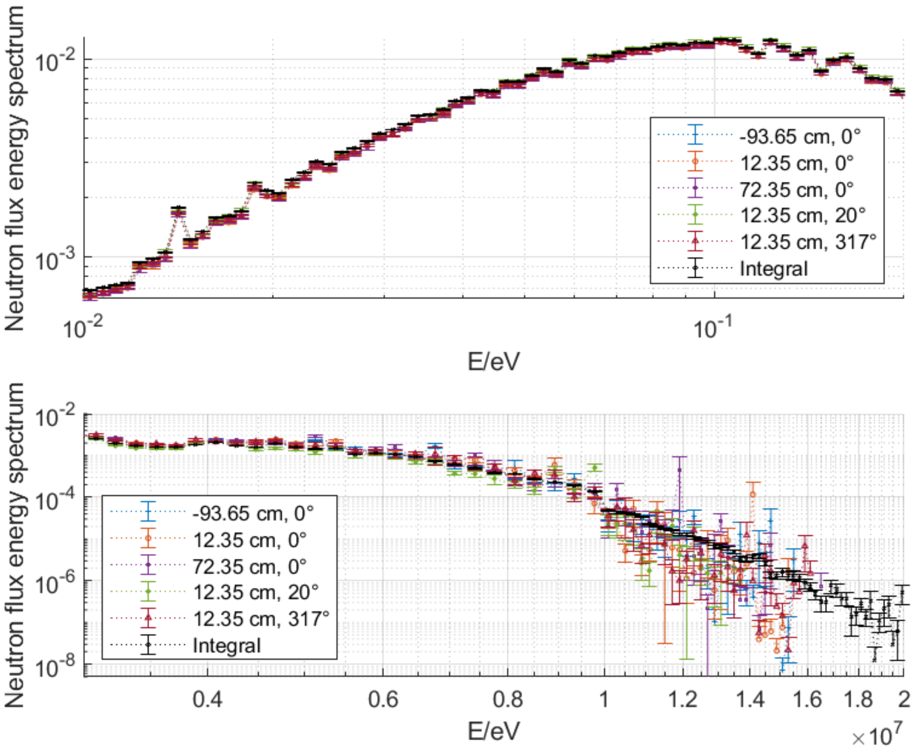

Fig. 3.9 Thermal (top) and fast (bottom) neutron flux energy spectra in lethargy scale as a function of the energy E of some of the other points located on the internal surface of the shield at different heights and angular coordinates.

3.4 Step 4: Results comparison and validation

The findings in this Section are presented using the C/M ratio, defined as:

$$\frac{C}{M} \equiv \frac{Specific\ activity_{calculated}}{Specific\ activity_{measured}} \tag{3.1}$$

a metric that facilitates a comparison between the specific activities predicted by the scheme and the data available in the database, for each isotope and each specific point of analysis. C/M values within the 1 to 10 range are regarded as acceptable, as they suggest a conservative estimate of specific activities without significant overestimation, aligning with decommissioning requirements [71], [72]. This range is considered reasonable in light of related research. For instance, [39] reported values within the 0.9 to 6.8 range for various isotopes, often coinciding with the results from activation foil campaigns detailed in [66]. [40] and [36] in Annex IV examined multiple isotopes and presented values up to 7.7 and 7.9, respectively, in specific locations.

In a prior activation study conducted for Sogin [27], acceptable values were within the range of 0.7 to 8.77. Discrepancies between calculated and measured values often arise due to a combination of factors, including uncertainties in nuclear data, activation measurements, flux estimation, material compositions, and operational history. Additionally, the utilization of MC techniques introduces statistical uncertainty into the assessment. This latter aspect was kept under control ensuring for all the neutron fluxes used in this analysis a relative standard deviation comprised between 1.2 and 1.7 %.

3.4.1 1969 sampling campaign on the thermal shield

In August 1969, the first sampling campaign was conducted on the thermal shield. Following its removal from the reactor at the conclusion of the initial operating cycle, the component was stored in the adjacent pool. The primary objective of this campaign was to assess the axial distribution of residual activation resulting from ^{60}Co and ^{54}Mn on the inner side of the shield at $\theta = 0°$. Additionally, the study included two points on the inner and outer surface of the shield at $\theta = 317.2°$, as well as a single point on the outer surface at $\theta = 0°$ [73]. It is necessary to note that these data were collected for industrial purposes, and the details of the measurement procedures, as well as error margins, are not available. Therefore, the uncertainty presented here solely pertain to the results calculated using FISPACT-II.

Axial distribution of residual activation due to ^{54}Mn and ^{60}Co at $\theta = 0°$

Figure 3.10 illustrates the axial distribution of residual activation stemming from ^{54}Mn and ^{60}Co on the internal surface of the shield. Correspondingly, Figure 3.11 showcases the axial distribution of the respective C/M values.

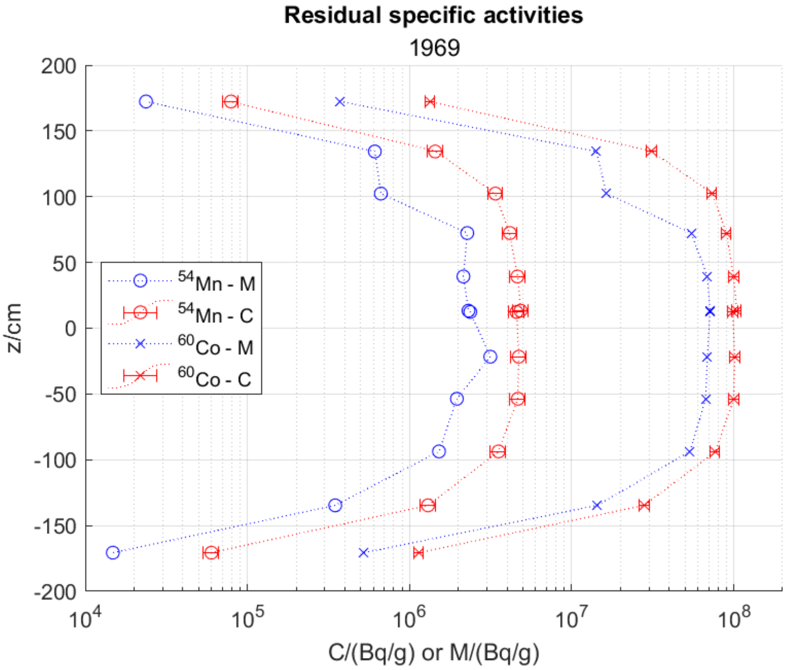

Fig. 3.10 Axial comparison between computed (C) and measured (M) axial distribution of the specific activity on the inner surface of the shield caused by ^{54}Mn and ^{60}Co at $\theta = 0°$. Measurements from the 1969 sampling campaign.

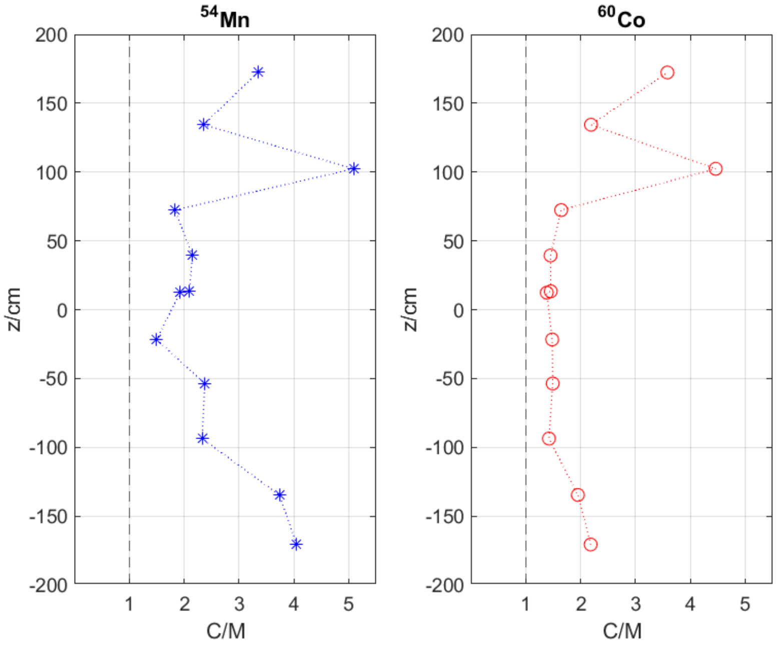

Fig. 3.11 Axial distribution of the C/M values for the isotopes considered.

As depicted in Figure 3.11, all C/M ratios for both isotopes fall within the 1 – 10 range of acceptability. The slight anomaly at $z = 102.35$ cm may be attributed to potential issues with the sample or measurement process, especially as it occurs similarly for both isotopes. In general, the results are deemed satisfactory. The calculated residual activations, while slightly higher than the measured values, consistently yield C/M ratios greater than 1, even when considering the error margins. As previously noted, ^{54}Mn is not a significant concern for the dismantling of the Trino reactor, in fact, it was already undetectable during the 1992 sampling campaign [73]. Conversely, ^{60}Co is a more significant nuclide due to its gamma ray emissions. Its presence necessitates a comprehensive and meticulous radiation protection plan during all phases of the dismantling process, such as vessel and internals segmentation and transport. This approach ensures that worker radiation exposure remains as low as reasonably achievable, aligning with the ALARA principle.

Other local residual activation values on the thermal shield surfaces

Only one sample was obtained from the outer surface of the shield at $\theta = 0°$, located at the same height as one of the internal points ($z = 12.35$ cm). The comparison results are presented in Table 3.3.

Table 3.3 Residual activation caused by ^{54}Mn and ^{60}Co on the external surface of the shield, at $z = 12.35$ cm and $\theta = 0°$. Calculations (C) from FISPACT. Measurements (M) from [27]. ΔQ from (2.76).

Isotope	C/(Bq/g)	ΔQ %	M/(Bq/g)	C/M
^{54}Mn	1.20E+06	10.89	9.25E+05	1.30
^{60}Co	1.93E+07	8.02	1.41E+07	1.37

A good agreement is evident between the scheme's outcomes and the actual measurements, although it is important to highlight that the uncertainty shown is the one calculated by FISPACT-II, which in turn does not consider the statistical uncertainties related to the MC calculation [59]. The C/M values remain within the acceptable range on the outer surface of the shield as well. Both isotopes' specific activities are accurately replicated, and in keeping with previous assessments, the results continue to be slightly overestimated.

At $\theta = 317.2°$, two samples were obtained, one from the inner and one from the outer side of the shield, both situated at $z = 12.35$ cm, mirroring the configuration of the internal and external points examined at $\theta = 0°$. Unfortunately, data regarding only ^{60}Co measurements are available for these two positions. The comparative results are detailed in Table 3.4. The overall assessment of the scheme's performance in evaluating the residual activation measured in 1969 is quite satisfactory for both ^{54}Mn and ^{60}Co. All the calculated C/M ratios fall within the proposed acceptable range. Particularly noteworthy is the fact that in many instances the disparities are generally within a factor of 2. In should be noted nevertheless that a detailed sensitivity analysis is missing, as it was deemed not compatible with the project timeline. It is therefore included in the areas were the model could be improved in future works.

Table 3.4 Residual activation caused by ^{60}Co on the internal and external surface of the thermal shield, at $z = 12.35$ cm and $\theta = 317.2°$. Calculations C from FISPACT. Measurements M from [73]. ΔQ from (2.76).

Isotope	C/(Bq/g)	ΔQ %	M/(Bq/g)	C/M
Internal	1.14E+08	7.01	5.77E+07	1.98
External	2.22E+07	8.02	1.48E+07	1.50

3.4.2 1992 sampling campaign on the thermal shield

The second sampling campaign on the thermal shield occurred in February 1992, with the objective of assessing the specific activities stemming not only from ^{60}Co, but also from ^{55}Fe, ^{59}Ni, and ^{63}Ni. As previously introduced, ^{55}Fe possesses a relatively short half-life of 2.74 years. Consequently, its concentration nowadays has diminished more than 20-fold since the removal of the thermal shield from the reactor in 1967. The current specific activity of ^{55}Fe within the thermal shield is anticipated to be less than 1/2000 ($1/2^{11}$ = 1/2048) of the levels recorded in 1992. ^{55}Fe may hold greater significance in the future decommissioning of carbon steel components, such as the RPV, owing to the higher iron content in their composition and their longer irradiation period. On the other hand, ^{59}Ni and ^{63}Ni emerge as two of the most relevant isotopes in decommissioning. This is primarily due to the substantial presence of nickel in stainless steel components and their notably extended half-lives. Consequently, the decay of these isotopes occurs at a much slower rate compared to other isotopes like ^{60}Co. As a result, these two nuclides will exert a prolonged influence on the material's overall radioactivity. The activity resulting from ^{59}Ni and ^{63}Ni assumes significance in waste classification procedures as well, as it is one of the criteria considered by Italian regulations, reported in Section 1.6.3, to categorize waste as either low-level waste (LLW) or intermediate-level waste (ILW). Specifically, a waste package falls under the low-level waste (LLW) category if the residual activation attributed to ^{59}Ni and ^{63}Ni is less than 40 kBq/g, along with other parameters such as total activity and the presence of other long-lived isotopes. Exceeding this value would designate the waste package as intermediate-level waste (ILW), regardless of other considerations.

During the 1992 campaign, reported in [73], only two sampling points were selected at $\theta = 20°$ and $z = 12.35$ cm, one on the inner and one on the outer surface of the shield [21]. The measurement of specific activities for ^{55}Fe, ^{59}Ni, and ^{63}Ni served to evaluate the scheme's performance in estimating these isotopes as well. Additionally, the 1992 dataset includes error bars for these values, enabling more precise comparisons. The outcomes of these comparisons are depicted in Figures 3.12 and 3.13.

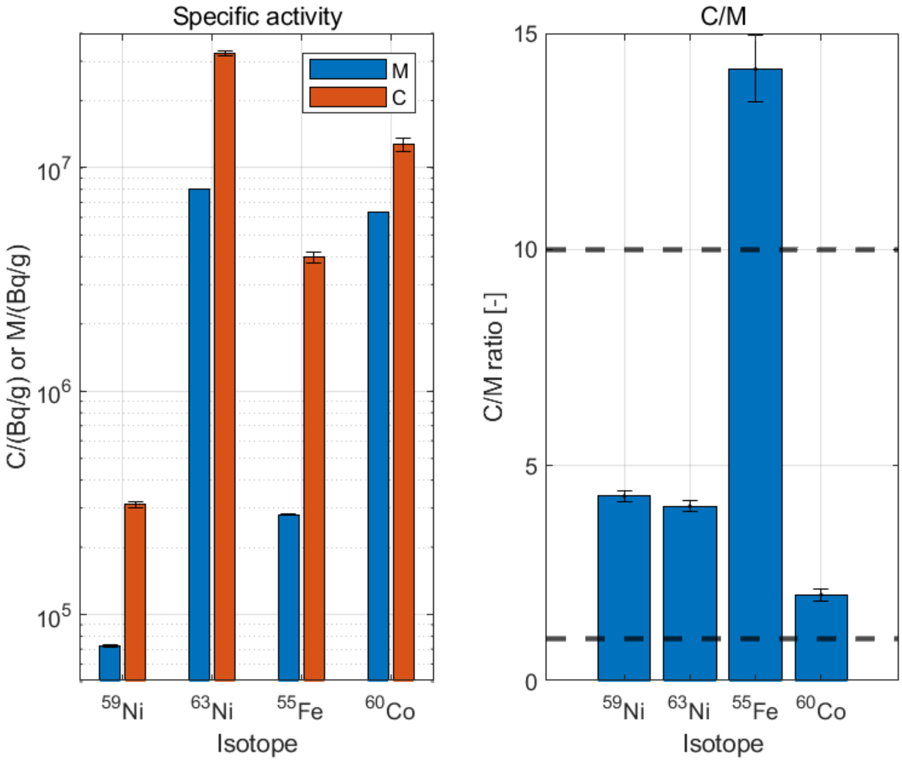

Fig. 3.12 (a) Computed (C) vs. measured (M) specific activities, and (b) C/M ratios, caused by ^{59}Ni, ^{63}Ni, ^{55}Fe and ^{60}Co on the internal surface of the thermal shield, at $z = 12.35$ cm and $\theta = 20°$.

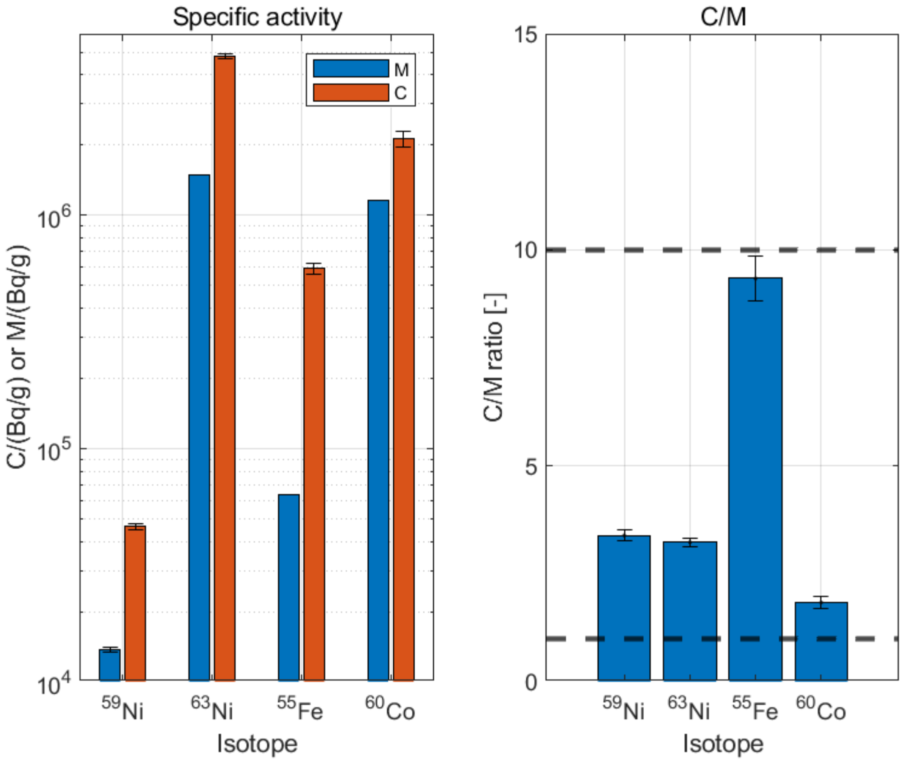

Fig. 3.13 (a) Computed (C) vs. measured (M) specific activities, and (b) C/M ratios, caused by ^{59}Ni, ^{63}Ni, ^{55}Fe and ^{60}Co on the external surface of the thermal shield, at $z = 12.35$ cm and $\theta = 20°$.

The concentration of ^{55}Fe appears to be particularly high compared to the other radioactive species evaluated. Considering that all these analysed isotopes are mainly generated by radiative capture of thermal neutrons, as suggested by the pathway analysis performed by FISPACT, this could be at least partially due to a larger share of the precursor isotope in the material used for the simulation with respect to the real one. In fact the neutron flux appears to work well both in terms of intensity and spectrum for ^{59}Ni, ^{63}Ni and ^{60}Co, and using different data libraries does not seem to address the issue, as ^{55}Fe is always overestimated compared to the other isotopes. Out of all the major parameters concurring to the production of ^{55}Fe, the initial share of the precursor in the material appears to be the only one that could significantly affect that isotope only, but this aspect would require further research, as a factor 10 difference is indeed strange.

This overestimation of ^{55}Fe, nevertheless, is not expected to be significant due to its short half life and its much lower contribution to the total residual activity nowadays, many decades after reactor shut down. Moreover it does not emit strong gamma rays, therefore its relevance in terms of radiation protection is modest, and it is not one of the key isotopes considered for waste classification in Italy.

3.5 Main remarks

To assess the residual activation of the Trino reactor's structures, a four-step calculation scheme was devised. This scheme was originally developed focusing on the thermal shield, and shows good performance. It successfully replicates nearly all measurements from both datasets with a good degree of accuracy.

All outcomes are overestimated and fall within the suggested acceptability range ($1 < C/M < 10$). There's only one exception, the specific activity of ^{55}Fe calculated for the point on the internal surface at $z = 12.35$ cm and $\theta = 20°$, which is slightly overestimated. This overestimation may stem from a lower precursor concentration in the stainless-steel alloy used, compared to the one modeled. This discrepancy would require further analysis, however, it is not considered significant, especially during the decommissioning phase, as the isotope is characterized by a short half-life, a low impact on gamma rays emissions and its current concentration is already a small fraction of the original. Moreover, it is not one of the critical isotopes for waste classification in Italy.

In most instances, particularly for ^{60}Co, the calculated specific activities are within a factor of 2 of the measured values, indicating the scheme's strong performance. It is worth noting that the comparisons with the 1969 data had to be conducted without considering measurement errors, underscoring the challenges of working with legacy data primarily collected for industrial purposes, lacking a detailed description of the methods used. Despite this limitation, the scheme accurately estimates the specific activities caused by the most critical isotopes in decommissioning: ^{60}Co for radiation protection planning, and ^{59}Ni and ^{63}Ni for waste characterization. It also correctly predicts the specific activities caused by ^{54}Mn and, to a lesser extent, of ^{55}Fe, with only the latter being overestimated in one instance.

The simulation scheme's results are subject to the same set of uncertainties previously discussed in Section 3.4, arising from various parameters involved in residual activation assessment. Material composition, measurements, irradiation time, Monte Carlo simulation statistics, and nuclear data can all contribute to the final overestimation of results.

A significant overhaul of the core took place after the first cycle to enhance reactor performance, consequently, this current geometrical and neutronic model would not be applicable to the analysis of subsequent operational cycles of the reactor. However, its applicability has already been expanded to analyze the RPV liner, a topic that will be covered in Chapter 4.

Chapter 4

Application of the developed model to the reactor pressure vessel's liner

In this Chapter, a slightly modified version of the model described in the previous chapter is applied to the RPV liner, mirroring the approach used for analyzing the thermal shield. This secondary analysis aims to offer useful insights into the segmentation plan of the component. Segments located farther from the core are anticipated to exhibit minimal activation, potentially enabling their treatment as conventional waste and consequently yielding substantial cost savings.

The primary goal of this analysis is to assess the specific activations and contact dose rates at various points along the height and circumference of the RPV's internal surface. The internal surface was selected for this examination due to the RPV being primarily made of carbon steel and internally covered by a thin stainless-steel liner. As previously discussed in Section 1.4.1, stainless steels typically undergo more significant neutron activation due to the high nickel content in their composition. Additionally, the liner is in closer proximity to the neutron source compared to the external surface. Consequently, the liner is expected to exhibit the most significant activation within the RPV due to both these reasons.

In segmentation planning, the separation of the liner from the bulk of the RPV is usually not considered feasible due to the complexities and cost involved in handling the radioactive working environment. Disposing of segmented RPV sections without further cuts often seems to be the most practical and cost-effective solution.

4.1 Differences with respect to the scheme adopted for the thermal shield

The calculation scheme used here closely resembles the one developed for the thermal shield analysis, but with three key modifications.

The first change involves the geometry of the track length detectors utilized to estimate the neutron flux. Unlike the 1 cm radius of the spherical detectors used in the thermal shield analysis, the radius for the RPV liner analysis has been increased to 5 cm. This modification allows for more statistics to be obtained reducing the statistical uncertainty in the evaluation of the neutron flux, especially in areas significantly distant from the core, such as the reactor's head or bottom. On the other hand, the flux is averaged over a larger volume, making the prediction less accurate.

The second change is related to the treatment of the fuel. While for the analysis of the thermal shield the fuel was considered fresh, in this case it is depleted. The approximated composition of the fuel is determined performing a depletion calculations with Serpent 2. The depletion is performed simulating a single assembly from each fuel batch of interest using periodic boundary condition in two directions to consider the presence of neighboring assemblies. This is an approximation, as in reality in the core some assemblies do not have neighbors all around (e.g. on the periphery) and the assemblies around may not belong to the same region. It was nevertheless deemed useful to update the fresh fuel configuration that characterized the analysis of the thermal shield. The depletion calculation is normalized imposing the produced power, as the ratios between the power produced by one average assembly of the region and the average power per assembly are available. Each assembly is depleted according to the power levels and the stops that characterized the reactor during its operation. The burnup reached at the end of the depletion is then compared to the burnup reported by Sogin, to assess discrepancies. The calculated values appear to approximate well the reported ones, as the relative difference between the calculated and reported values in all cases is around 2-3%. The composition selected to represent a middle of cycle condition is, for each region and each cycle, the one corresponding to the burnup of that fuel batch halfway through the cycle of interest.

The third modification is related to the acceleration technique applied. In the thermal shield analysis, a combination of GVR and detector-specific acceleration was utilized, whereas, in this case, only GVR was employed. This choice primarily stems from opting for larger detectors, as the acceleration provided by GVR proves sufficient, therefore reducing the overall calculation time.

A few other measurements of specific activity exist in various regions of the reactor: as a result, the model has been extended to replicate those measurements as well. The aim would be to further validate the model as it is expanded from the first cycle to encompass all subsequent cycles.

4.2 Model extension to all operating cycles

Extending the model to encompass all operating cycles posed a significant challenge. The Trino reactor underwent continuous modifications throughout its operational lifespan, thus requiring these adjustments to be considered into the development of the neutronic model. Two primary strategies exist for analyzing a reactor's complete life: examining each separate cycle individually or employing a *representative cycle*, which represents the average core configuration for most of the reactor's life.

The first approach demands substantial computational resources, potentially requiring in this case the creation and simulation of nine distinct core configurations. Each core analysis necessitates particle propagation towards the detectors, significantly increasing the number of simulations as more cores and points are analyzed.

The second method, often known as the *Representative Operating Cycle* (ROC), involves identifying an average core configuration that reflects the typical conditions of the core concerning geometry and enrichments throughout the reactor's lifespan. Although this strategy has proven effective [28], [66], [40], [38], it is usually recommended for reactors with relatively consistent operations, featuring minimal power fluctuations and geometric changes — a description that does not align with the Trino reactor's history. Here below is a concise list of the various modifications that affected the Trino reactor:

- Switch from a high leakage refueling pattern to a low leakage one between the first and second cycles;
- Removal of the thermal shield after the first cycle;

- Replacement of eight corner assemblies with zircaloy dummy ones after the first cycle;
- Increase in nominal power, from 825 MW_{th} to 870 MW_{th}, but only after the fourth cycle;
- Substitution of fuel followers attached to control rods with zircaloy ones after the fourth cycle;
- Gradual enrichment increase, starting from 2.72% (the lowest value during the first cycle) to 4.47% (the highest in the ninth cycle);
- Incorporation of a batch of MOX fuel assemblies.

Additionally, the reactor underwent significant power variability, further complicating the scenario. A detailed presentation of the reactor's power history reconstruction will be provided in Section 4.5.2. The initial strategy adopted to tackle this issue adopts a hybrid approach between these two methods. Given the initial complexity of identifying a single ROC and the computational expense of simulating all cycles, a decision was made to group similar cycles into macro groups. This grouping considers the various modifications introduced during the plant's life, aiming to reduce the number of cycles that need analysis. Essentially, this approach elaborates on the ROC strategy by analyzing multiple cycles to spotlight specific segments of the reactor's life.

4.3 Step 1: Critical simulation for source generation extended to different cores

A more detailed breakdown of the simulated cores is here available:

1. The first core, visible in Figure 4.1a, aligns with the initial operating cycle, distinct from the others. This core mirrors the geometrical features used in the thermal shield analysis but the depleted fuel is used and the source is normalized in Serpent2 at 825 MW_{th} instead of 870 MW_{th}, a modification made after obtaining additional operational documentation indicating a lower nominal power, as previously mentioned in Section 3.1. This allowed to update

the configuration used for the analysis of the thermal shield. This core serves solely for evaluating the first operational cycle, due to its stark differences in components, fuel elements count, averaging at 3.25% enrichment, and loading pattern;

2. The second core analyzed, visible in Figure 4.1b, corresponds to the third cycle and is utilized to analyze the second, third, and fourth cycles. This core lacks a thermal shield and corner assemblies, replaced by zircaloy dummies. It retains fuel followers attached to control rods. The other fuel elements average around 4% enrichment, and the reactor operated with a low leakage loading pattern, in contrast to the high leakage pattern in the first cycle;
3. The third core analyzed, visible in Figure 4.1c, represents the fifth cycle, which is the first cycle without fuel followers, removed due to high burnup after continuous presence throughout the preceding cycles. These were replaced with dummy zircaloy followers due to the uneconomical nature of replacing them with fresh fuel, as the shifting positions of these followers resulted in uneven and suboptimal fuel consumption. The average fuel enrichment stands at around 4.13%. This core was used solely for the fifth cycle analysis due to the relatively lower average enrichment;
4. The fourth and final simulated core, visible in Figure 4.1d, corresponds to the ninth cycle, sharing similarities with the previous core but exhibiting a higher average enrichment of 4.47%. This core represents cycles from the sixth to the ninth.

Each of these cores was used to perform a MC critical calculation and generate the neutron source file, similarly to what has been done for the thermal shield.

4.4 Step 2: Accelerated transport towards detectors positioned on the RPV internal liner

Each source file generated from the critical simulations was utilized to conduct a series of external source simulations, examining multiple points distributed at various heights and angular positions along the internal liner's circumference. The specific

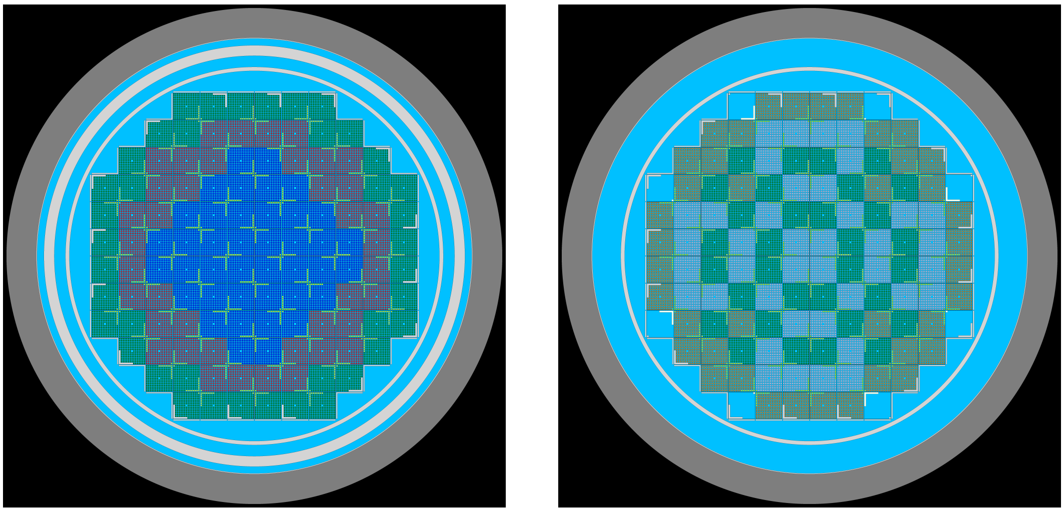

(a) First core analyzed.

(b) Second core analyzed.

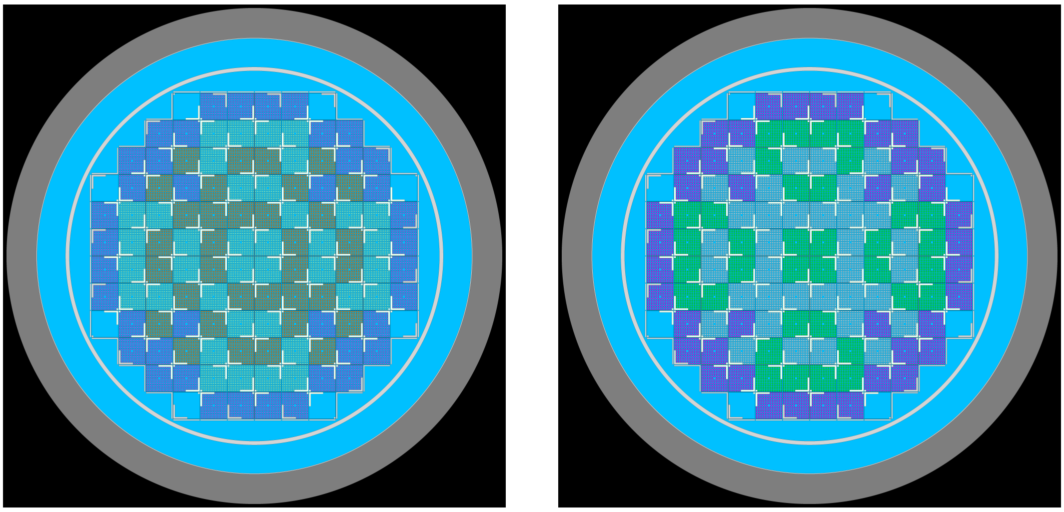

(c) Third core analyzed.

(d) Fourth core analyzed.

Fig. 4.1 Horizontal sections of the analyzed cores.

heights under scrutiny are detailed in Table 4.1. Employing the same reference frame as the thermal shield analysis, the designation $z = 0$ corresponds to the midplane of the active zone. Although the cores are not entirely quarter-symmetric, as the unconventional structure of the control rods/fuel followers/zircaloy followers create a more complex geometry and the fuel assemblies distribution in the third core differs slightly from full symmetry, they were treated as such. No symmetry option in the calculation was used, as the entire core was simulated, but for each height a set of 25 track length detectors was defined to cover only a quarter of the reactor's circumference. This approximation allowed to reduce the number of points to analyze.

There is an exception at $z = 454$ cm due to the distribution of points along the internal surface of the vessel head, which possesses a smaller radius compared to the remaining RPV. Consequently, to maintain consistent sphere size, 23 detectors were defined at this particular height. The angular coordinates of the sphere centers are provided in Table 4.2.

Table 4.1 Heights z considered in the framework of this study.

z/(cm)	-393	-350	-300	-250	-200	0	186	277	327	454

The angular flux profiles at different heights are visible in Figures 4.2 and 4.3, for the upper and lower parts of the reactor respectively.

The analysis of the neutron flux angular profile at various heights indicates that the flux is characterized by more pronounced angular peaks in the central and upper regions of the reactor, whereas the lower and uppermost sections exhibit relatively uniform irradiation, as the oscillations are likely caused by statistical fluctuations. Consequently, for heights displaying this uniformity, the activation calculations consider the average of the local flux values determined at those specific heights. To reduce computational efforts, upon recognizing this flux uniformity at select heights, the number of examined points was reduced from 25 to 6. Specifically, only bins 1, 5, 10, 15, 20, and 25 were considered, as illustrated in Figure 4.3.

The disparities in the flux profile are likely due to the presence of extracted control rods in the upper reactor part, potentially acting as neutron sinks. In particular, at heights displaying an angular flux profile, the impact of geometric alterations introduced after the first cycle becomes clear, specially for the region directly facing the core. The removal of corner assemblies and the thermal shield resulted in flux

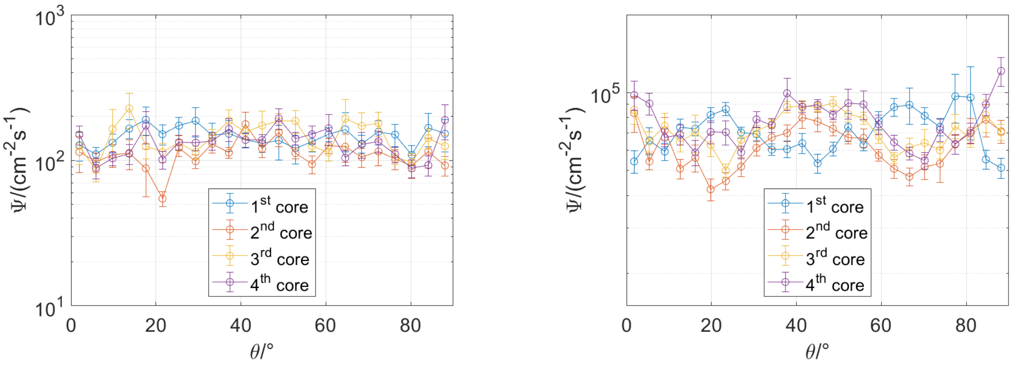

(a) $z = 454$ cm.

(b) $z = 327$ cm.

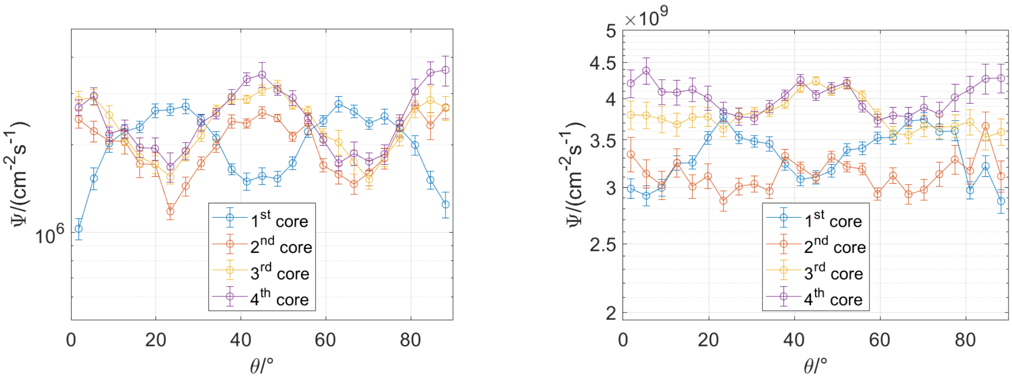

(c) $z = 277$ cm.

(d) $z = 186$ cm.

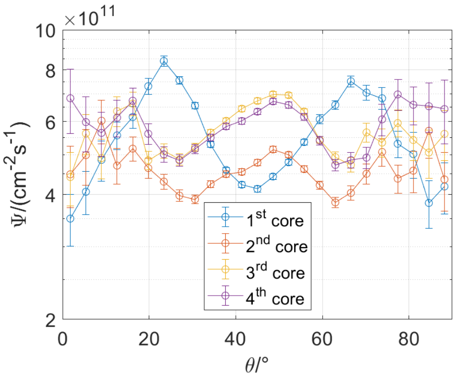

(e) $z = 0$ cm.

Fig. 4.2 Angular profiles of the neutron flux Ψ impacting on the RPV liner - upper part of the reactor. The error bars represent 1 σ statistical uncertainty

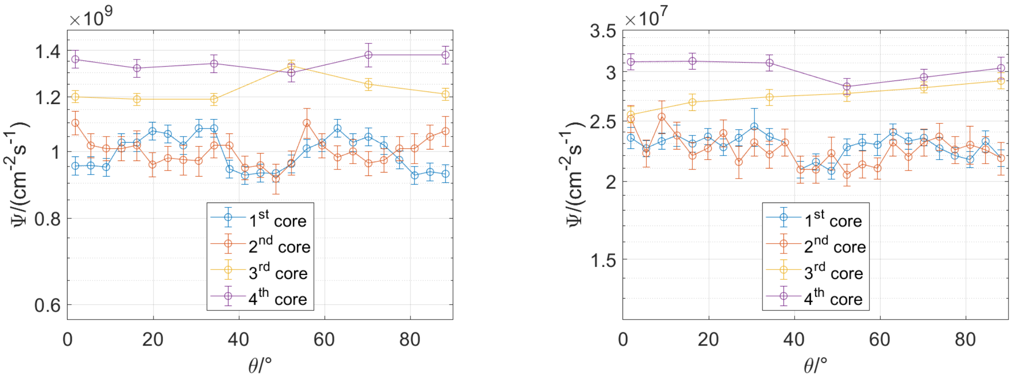

(a) $z = -200$ cm.

(b) $z = -250$ cm.

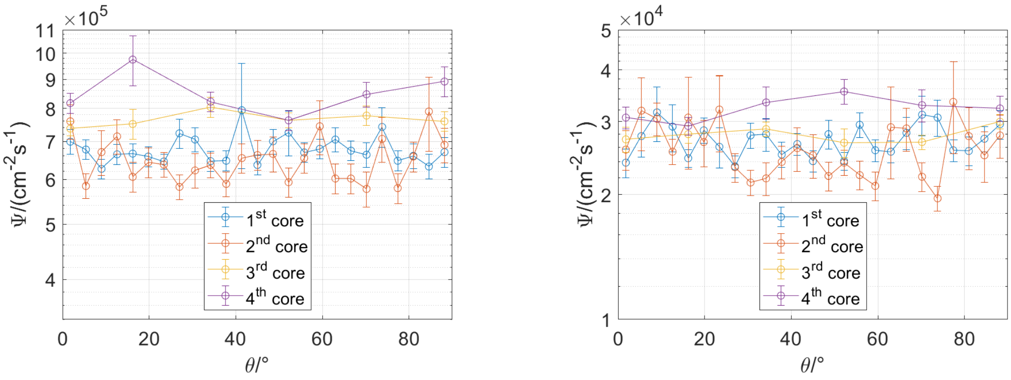

(c) $z = -300$ cm.

(d) $z = -350$ cm.

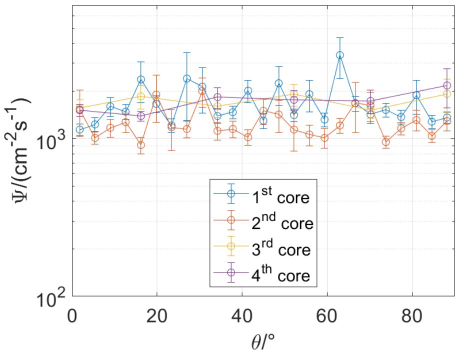

(e) $z = -393$ cm.

Fig. 4.3 Angular profiles of the neutron flux Ψ impacting on the RPV liner - lower part of the reactor. The error bars represent 1 σ statistical uncertainty

Table 4.2 Angular coordinates θ of the sphere detector's centres used in the framework of this study.

bin	Detectors $\theta/°$	Detectors $\theta/°$ @ $z = 454$ cm
1	1.80	1.96
2	5.40	5.87
3	9.00	9.78
4	12.60	13.70
5	16.20	17.61
6	19.80	21.52
7	23.40	25.43
8	27.00	29.35
9	30.60	33.26
10	34.20	37.17
11	37.80	41.09
12	41.40	45.00
13	45.00	48.91
14	48.60	52.83
15	52.20	56.74
16	55.80	60.65
17	59.40	64.57
18	63.00	68.48
19	66.60	72.39
20	70.20	76.30
21	73.80	80.22
22	77.40	84.23
23	81.00	88.04
24	84.60	
25	88.20	

distribution alterations, leading to a reduction and change in the angular position of local peaks. These modifications were indeed introduced to flatten the flux angular profile, as pronounced flux peaks on the RPV are generally undesirable due to increased activation and potential neutron-induced material structural damage, which could affect the reactor's lifespan.

Both phenomena, activation and neutron damage, are related to neutron fluence resulting from irradiation, which is influenced by all operational cycles, and the distinct peak distribution resulting from modifications introduced after the first cycle affects the final fluence distribution. Notably, it cannot be assumed a priori that maximum fluence points correspond to the flux peaks. Thus, the adopted strategy is twofold:

- For heights exhibiting a neutron flux angular profile (0, 186, 277, and 327 cm), the objective is to identify maximum and minimum fluence points. This involves considering the flux profile, computing the fluence caused by each macro group for each point and summing these values to obtain an integral fluence value that encompasses contributions from all cycles. These maximum and minimum fluence points are then investigated to determine an interval of possible residual activation values.
- For heights without a neutron flux angular profile (-393 to -200 and 454 cm), calculating a single fluence value using the average flux for each height and each macro group is sufficient due to the mostly uniform irradiation. Summation of these values represents the average integral fluence from all cycles for points at that height. Employing the average flux contributes to lower relative standard deviation, thereby improving accuracy in estimating the residual activation.

The impact of the presence or absence of fuel followers on the neutron flux distribution within the RPV liner appears insignificant. This is likely due to the physical distance, as it is well-known that the fuel assemblies contributing to the RPV irradiation primarily belong to the outer region of the core [38]. Fuel followers, representing only few percentage points of the fuel mass of the core and situated far from the edge, contribute minimally to neutron leakage and therefore to the neutron flux affecting the RPV. In contrast, the removal of corner assemblies after the first cycle has a more pronounced and noticeable effect.

4.5 Step 3: Activation calculations for the RPV internal liner at different heights

Before proceeding with the activation calculations, the specific points for analysis have to be determined, since a comprehensive analysis of each local point would demand considerable time and resources. The ultimate residual activation strongly correlates with the fluence experienced by each point throughout reactor operation, serving as a reliable indicator for the expected activation levels within different regions. The fluence F is calculated as the product between the neutron flux Ψ and the irradiation time t. If different neutron fluxes apply to different irradiation time steps, the sum of the contributions of each step i is considered, as reported in (4.1).

$$F = \sum_i \Psi_i t_i \tag{4.1}$$

For heights with a mostly uniform irradiation pattern, a single activation calculation was performed. Given the consistent fluence along the angular coordinate, calculated using the average flux, it is expected that the residual activation will follow a similar trend. Total fluence for these heights and associated relative standard deviations (RSD) are reported in Table 4.3.

Table 4.3 Total fluence F for heights z experiencing uniform irradiation. RSD propagated considering the sum of the contributions of different steps.

z/cm	$F/(\mathrm{cm}^{-2})$	Propagated RSD
454	4.22E+10	0.03
-200	4.02E+17	0.009
-250	9.08E+15	0.011
-300	2.59E+14	0.02
-350	1.00E+13	0.03
-393	5.38E+11	0.06

In contrast, heights exhibiting a distinctive angular distribution of the neutron flux, such as the ones visible in Figure 4.4, led to the selection of two points for activation calculations: the points experiencing maximum and minimum fluence. This approach translates into the examination of maximum and minimum activation points, facilitating an assessment of the potential range of residual activations at the analyzed height. Minimum and maximum fluence points and their respective fluence are listed in Table 4.4.

A second calculation was conducted, assuming uniform irradiation for the points exhibiting an angular fluence profile as well. The aim was to evaluate the influence of this type of approximation on the outcomes, specially for what concerns the loss of information caused by neglecting the angular variability of the flux. For this scenario, the residual activation was determined using the average flux for each cycle

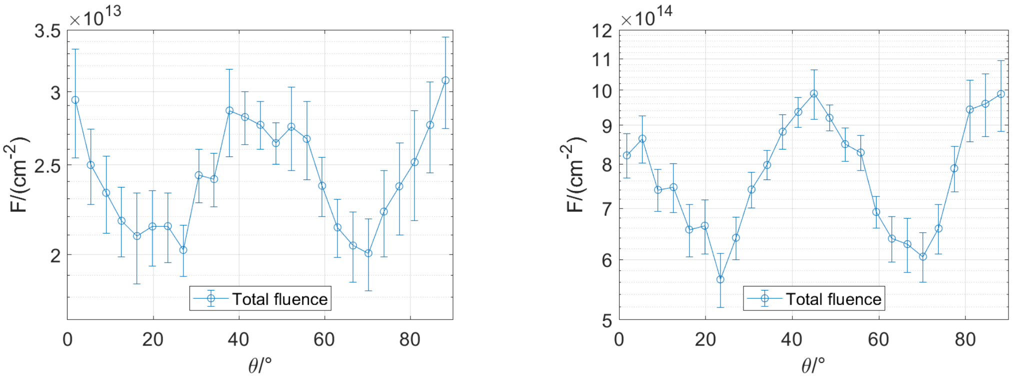

(a) $z = 327$ cm. (b) $z = 277$ cm.

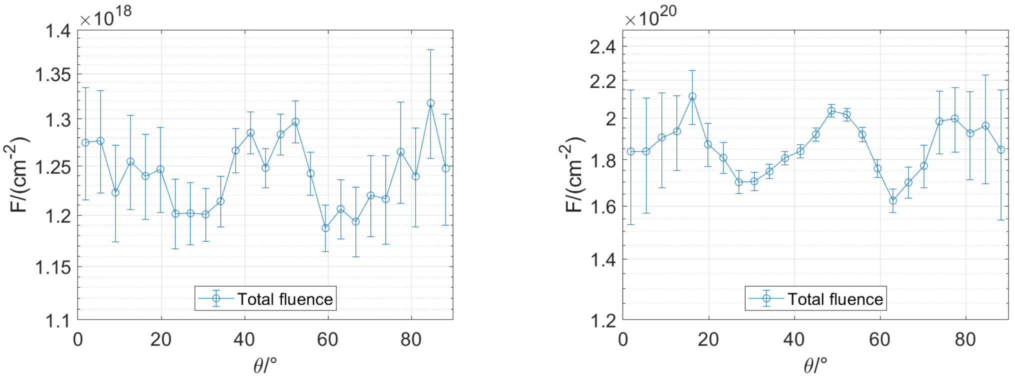

(c) $z = 186$ cm. (d) $z = 0$ cm.

Fig. 4.4 Total fluence F for heights exhibiting an angular profile of the neutron flux.

Table 4.4 Angular coordinates θ and total fluence F of minimum and maximum fluence points for different heights z. RSD propagated considering the sum of the contributions of different steps.

z/cm	Point	θ/°	F/(cm^{-2})	Propagated RSD
327	min	70.20	2.00E+13	0.08
	max	88.20	3.10E+13	0.11
277	min	23.40	5.60E+14	0.08
	max	45.00	9.80E+14	0.07
186	min	59.40	1.19E+18	0.019
	max	84.60	1.32E+18	0.04
0	min	63.00	1.60E+20	0.02
	max	16.20	2.10E+20	0.06

and height, similarly to what has been done for the points in Table 4.3, and therefore disregarding the angular distribution of flux. The values of uniform fluence are listed in Table 4.5

Table 4.5 Total fluence F for heights z experiencing an angular distribution of the neutron flux under the hypothesis of uniform irradiation. RSD propagated considering the sum of the contributions of different steps.

z/cm	F/(cm^{-2})	Propagated RSD
327	2.45E+13	0.02
277	7.81E+14	0.014
186	1.24E+18	0.006
0	1.86E+20	0.016

The ratios between the previously identified maximum and minimum values, and the fluence calculated using the average flux, are documented in Table 4.6. In particular, the relative difference between the maximum value and the uniform one is around 27% in regions farther from the reactor core. Conversely, in the proximity of the core, this underestimation seems comparatively smaller and, on the whole, more acceptable. A similar pattern is expected for activation considering the strong correlation between the two parameters.

The isotopes of primary significance are ^{59}Ni and ^{63}Ni, owing to their substantial involvement in long-term activation, gamma radiation emission, and waste classification. Similarly to its significance in the context of the thermal shield analysis, ^{60}Co is relevant for radiation protection considerations, expected to serve as the primary contributor to the gamma field emanating from the components. A few other isotopes were considered, such as ^{51}Cr, ^{54}Mn, ^{58}Co, ^{59}Fe, ^{110m}Ag and ^{182}Ta, when

Table 4.6 Angular coordinates θ of minimum and maximum fluence points F_{local} and respective fluence ratios for different heights z. RSD propagated considering the ratio between the two quantities.

z/cm	Point	$\theta/°$	$\frac{F_{local}}{F_{uniform}}$	Propagated RSD
327	min	70.20	0.82	0.09
	max	88.20	1.27	0.11
277	min	23.40	0.72	0.08
	max	45.00	1.25	0.07
186	min	59.40	0.96	0.02
	max	84.60	1.06	0.04
0	min	63.00	0.86	0.03
	max	16.20	1.13	0.07

the analyses of a set of dosimeters and a liner sample were performed. The nuclear data library employed in this analysis is the TENDL-2019 [74].

4.5.1 Neutron flux energy spectra

Similar to the analysis of the thermal shield, understanding residual activation requires information about the neutron flux energy spectrum alongside the neutron flux. As in the previous analysed case, the energy distribution of neutrons appears weakly affected by the angular coordinate as visible for instance in Figure 4.5, where, as an example, the normalised spectra at different angular coordinates for the height $z = 327$ cm of the first cycle are compared. Averaging the spectra along the angular coordinate for each considered height has therefore been considered an acceptable approximation.

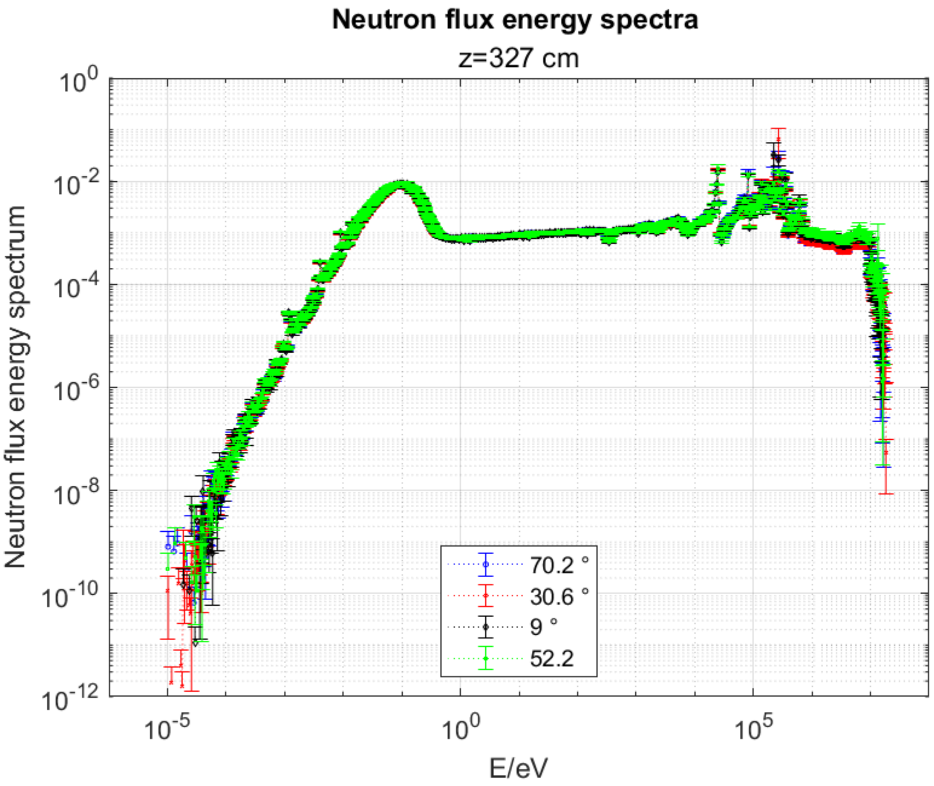

Fig. 4.5 Comparison between the local neutron flux energy spectra in lethragy scale as a function of the energy E belonging to points at different angular coordinates

It is important to note that the spectral characteristics are influenced by the specific height under consideration as well. This variability is evident, as illustrated in Figures 4.6 and 4.7, when normalized spectra from various heights are compared, as these spectra exhibit differences in both the thermal and fast neutron regions. Therefore, utilizing a singular average spectrum for the entire section would introduce additional uncertainties that are undesirable and may not accurately represent the varying neutron flux energy distributions across different heights.

Moreover, another influential parameter affecting the neutron flux energy spectrum is the radial coordinate. Although most analyzed points share the same radial coordinate, being situated on the inner surface of the RPV liner, points at $z = 454$ cm are located on the inner surface of the flange. Notably, the flange has a smaller internal radius compared to the RPV liner, which impacts the energy distribution of the neutron flux. This disparity is observable in Figure 4.7, where integral spectra for the upper section of the RPV liner are presented.

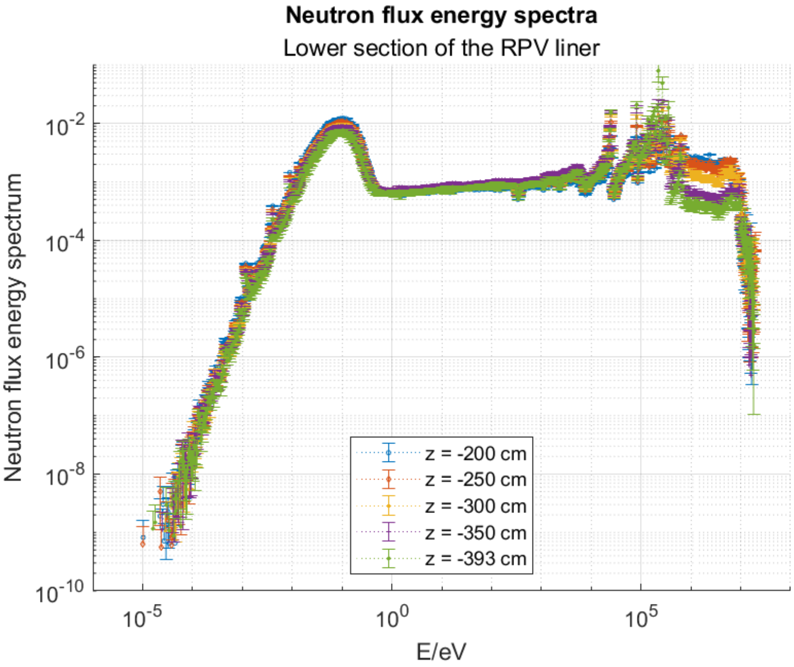

Fig. 4.6 Comparison between the integral neutron flux energy spectra in lethargy scale as a function of the energy E belonging to different heights in the lower section of the RPV liner.

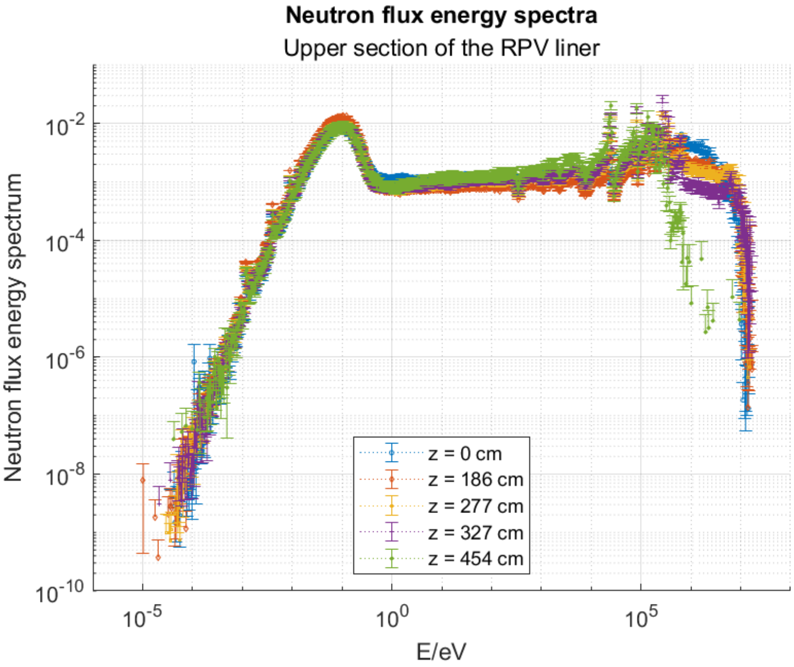

Fig. 4.7 Comparison between the integral neutron flux energy spectra in lethargy scale as a function of the energy E belonging to different heights in the upper section of the RPV liner.

Calculating a distinct local spectrum for each point would be computationally intensive without significant benefits, but at the same time utilizing a single spectrum for all heights would overlook the alterations in energy distribution due to increased distance from the source. Hence, the strategy applied involves computing a different spectrum for each height, integrated over the angular coordinate, in a procedure similar to what has been done for the thermal shield analysis. A section of a ring-shaped detector with height and thickness equal to the sphere detectors' diameter was used to evaluate the neutron flux energy spectrum integrating over the angular coordinate in the interval 0-90 °. This approach allows good accuracy without disregarding the differences introduced by varying heights and without being excessively demanding in terms of computational resources. Test activation calculations were performed to compare the performance of the integral spectra vs. the local ones and they suggest that the relative differences between the two approaches in the evaluation of residual activation after many decades of cooling time are limited. For example, using the spectra reported in Figure 4.5, the differences between the residual activation values calculated with the local spectra and the ones calculated with the integral spectrum range from a minimum of 1% to a maximum of around 7%.

The analysis of neutron flux energy spectra shows no significant dependence on the evaluated cycle as well, as shown for instance in Figure 4.8 for the points at $z = 277$ cm, except in one case: the point at $z = 0$ cm, particularly affected by the thermal shield removal, as can be seen in Figure 4.9.

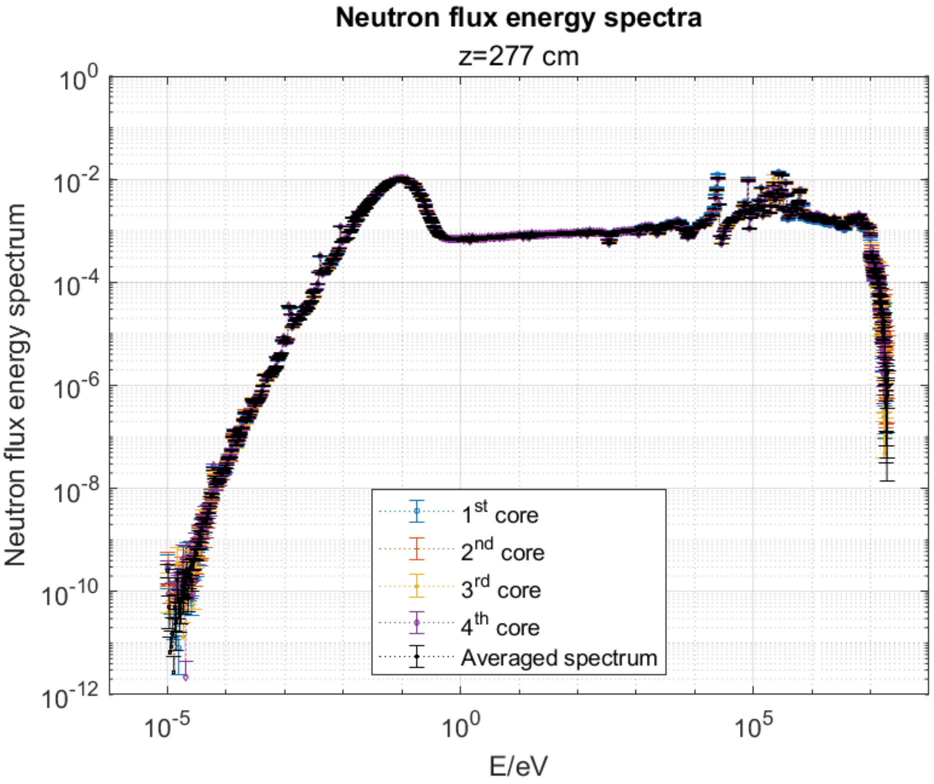

Fig. 4.8 Comparison between the integral neutron flux energy spectra in lethargy scale as a function of the energy E belonging to different cycles for the points at $z = 277$ cm and the spectrum averaged on all macro groups.

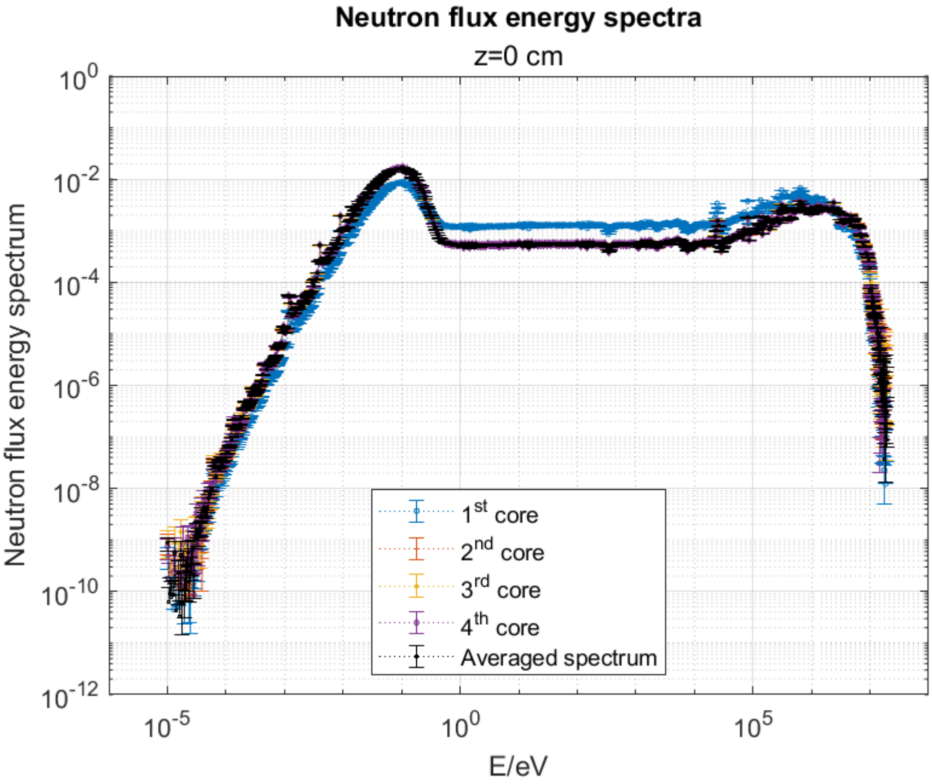

Fig. 4.9 Comparison between the integral neutron flux energy spectra in lethragy scale as a function of the energy E belonging to different cycles for the points at $z = 0$ cm and the spectrum averaged on the second, third and fourth macro groups.

Given the overall lack of substantial differences, except for $z = 0$ cm, a single spectrum averaged across all macro groups was employed for activation calculations, one for each height. This averaging process reduced the number of activation calculations required and lowered the statistical uncertainties, particularly in the high and low energy ranges. However, for the $z = 0$ cm points, the averaging procedure only involved the three spectra related to the second, third, and fourth macro groups. Consequently, for these points the activation calculation for the first cycle was conducted separately, and the resulting isotope inventory was utilized as the material composition in a subsequent second calculation. All spectra were computed using a quarter (0-90°) of a ring-shaped collision detector measuring 10 cm in height and 10 cm in width. This detector, defined to overlap and encompass the sphere detectors for evaluating the integral flux, ensures a good correspondence between the integral spectrum and local ones, enhancing accuracy without compromising critical information.

4.5.2 Reconstructed irradiation history

The reconstruction of the reactor's operational lifespan is itself quite challenging. The primary criterion relied upon involves conserving as much as possible the thermal energy generated during each cycle, based on the dataset provided by Sogin and delineated in Table 4.7 [27].

Table 4.7 Thermal energy E_{th} released each cycle. Dataset provided by Sogin [27].

Cycle	Period	E_{th}/MWd
1	22/10/64 - 28/04/67	460271
2	20/05/70 - 07/07/71	302982
3	23/09/71 - 29/03/73	365218
4	02/07/73 - 16/08/74	322235
5	21/10/74 - 02/04/76	406134
6	02/07/76 - 20/05/77	274891
7	01/08/77 - 19/01/79	430073
8	12/03/79 - 15/05/85	383512
9	31/07/85 - 21/03/87	423214

This reconstruction entails simplifying the actual operational history into a piecewise constant function, characterized by numerous irradiation steps at various constant power levels, separated by several shutdown phases. For detailed reference, the reconstructed power history used in the framework of this Chapter is outlined in Table 4.8, serving as a basis for the activation calculations.

Table 4.8 Reconstructed irradiation history. The length t of the steps is expressed in days.

Cycle	$P_{nominal}$/MW$_{th}$	Step	t/d	$\frac{P}{P_{nominal}}$	E_{th}/MWd
1	825	1	225	0.52	460267
		STOP	87	0	
		2	260	0.72	
		STOP	53	0	
		3	295	0.86	
		STOP	998	0	
2	825	4	22	0.34	302956
		STOP	97	0	
		5	24	0.36	

Table 4.8 Reconstructed irradiation history. The length *t* of the steps is expressed in days.

Cycle	$P_{nominal}$/MW$_{th}$	Step	t/d	$\frac{P}{P_{nominal}}$	E_{th}/MWd
		6	19	1	
		7	13	0.39	
		8	225	0.98	
		9	39	0.47	
		10	90	0.98	
		STOP	78	0	
3	825	11	10	0.94	365186
		STOP	38	0	
		12	151	0.93	
		13	32	0.41	
		14	175	0.96	
		STOP	7	0	
		15	40	0.99	
		16	103	0.70	
		STOP	96	0	
4	870	17	346	0.94	322213
		18	64	0.70	
		STOP	67	0	
5	870	19	34	0.34	406149
		20	401	0.97	
		21	92	0.72	
		STOP	91	0	
6	870	22	323	0.98	274828
		STOP	72	0	
7	870	23	536	0.92	429947
		STOP	52	0	
8	870	24	102	1	383429
		STOP	1752	0	
		25	371	0.91	
		STOP	130	0	
9	870	26	515	0.90	423081
		27	60	0.38	

The initial cycle reveals discrepancies when compared to the irradiation history adopted in the thermal shield analysis and listed in Table 3.2. These differences stem primarily from the utilization of a lower nominal power for source normalization and a more refined recalculation of the produced thermal energy. If both these aspects had been incorporated into the thermal shield analysis, the C/M ratios computed in Chapter 3 would have been at maximum approximately 10% lower. Nonetheless, this disparity does not undermine the validity of the findings: in fact, all C/M values would still be inside the acceptability interval considered.

4.5.3 Axial distribution of specific activities

The residual specific activity axial distribution for the uniformly irradiated points is listed in Table 4.9, whereas the distribution for the points exhibiting an angular profile is provided in Table 4.10.

Table 4.9 Calculated specific activity C for heights z experiencing uniform irradiation. ΔQ from (2.76).

z/cm	C/(Bq/g)	ΔQ %
454	1.12E-01	0.0[1]
-200	1.09E+04	2.7
-250	2.18E+02	2.7
-300	5.85E+00	2.6
-350	3.19E-01	1.8
-393	1.20E-01	0.2

All residual activations refer to March 2023. Similarly to what has been done for the fluence, the residual activation for the heights listed in Table 4.10 was recalculated using the uniform irradiation hypothesis as well, as reported in Table 4.11.

Upon comparing the detailed model with the uniform irradiation hypothesis at $z = 0$, 186, 277, and 327 cm as summarized in Table 4.12, it is noted that the relative difference between the uniform irradiation hypothesis and the maximum residual activation points is around 23-27% in regions far from the core. This underestimation, nevertheless, occurs for regions that exhibit relatively low residual activation, therefore it may be considered acceptable. The underestimation at core

---

[1] The reason why the error calculated by FISPACT-II in this case is 0 is that this region is so weakly irradiated that essentially no transmutation occurs.

Table 4.10 Angular coordinates θ and calculatd specific activity C of minimum and maximum fluence points. ΔQ from (2.76).

z/cm	Point	θ/°	C/(Bq/g)	ΔQ %
327	min	70.20	5.36E-01	2.2
	max	88.20	7.82E-01	2.3
277	min	23.40	1.32E+01	2.7
	max	45.00	2.34E+01	2.7
186	min	59.40	3.44E+04	2.7
	max	84.60	3.83E+04	2.7
0	min	63.00	5.35E+06	2.4
	max	16.20	7.20E+06	2.5

Table 4.11 Calculated specific activity C for heights z experiencing an angular distribution of the neutron flux under the hypothesis of uniform irradiation. ΔQ from (2.76).

z/cm	C/(Bq/g)	ΔQ %
327	6.37E-01	2.2
277	1.84E+01	2.7
186	3.61E+04	2.7
0	6.33E+06	2.5

level is larger in absolute terms, and a similar underestimation occurs for the dose rate. The implications of these underestimations will be discussed in Section 4.5.4.

A preliminary classification of the waste package derived from RPV segmentation is feasible, considering the Italian regulatory thresholds previously introduced across three primary parameters: total specific activity, the contribution from nickel isotopes, and the presence of alpha-emitting nuclides. In particular, the concentration of alpha-emitting nuclides remains essentially negligible across all examined regions, reaching a maximum of only a few dozen Bq/g in the core-facing zone. Given the substantial time since reactor shutdown and the faster decay of ^{60}Co, the predominant residual activity across all heights primarily arises from ^{63}Ni, which accounts for around 95% of the total. This is a well known phenomenon, as described in Section 1.4.1.

The axial distribution of the residual activity is reported in Figure 4.10, with only the results under the hypothesis of uniform irradiation for all points displayed. This is for the sake of clarity, as the logarithmic scale would not allow to notice the differences between maximum and minimum values, while also showing the very low levels of residual activation far from the core.

Table 4.12 Angular coordinates θ of minimum and maximum fluence points and respective calculated activation ratios. ΔQ from (2.76) and propagated considering the ratio between the two quantities.

z/cm	Point	θ/°	$\frac{C_{local}}{C_{uniform}}$	Propagated ΔQ %
327	min	70.20	0.84	3.1
	max	88.20	1.23	3.2
277	min	23.40	0.72	3.8
	max	45.00	1.27	3.8
186	min	59.40	0.95	3.8
	max	84.60	1.06	3.8
0	min	63.00	0.84	3.5
	max	16.20	1.14	3.5

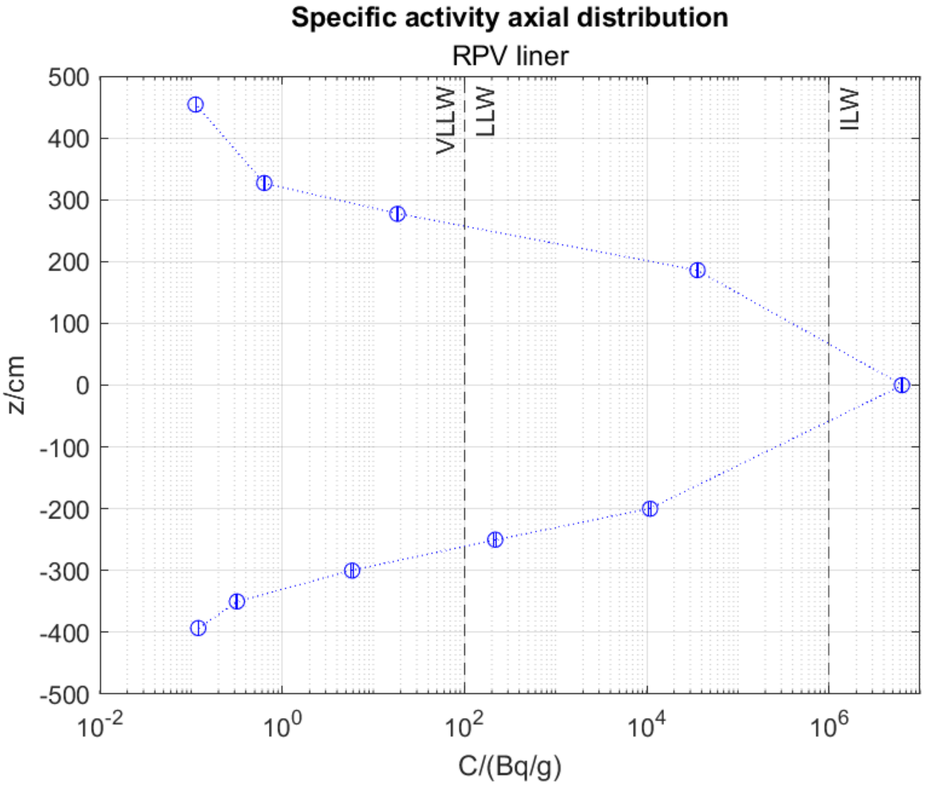

Fig. 4.10 Calculated specific activity (C) axial distribution in the RPV liner.

As can be seen in Figure 4.10, the region directly facing the reactor core at $z = 0$ cm appears to belong to the ILW category. In contrast, regions adjacent to it, extending to around $z = 186$ cm towards the reactor head and $z = -250$ cm towards the bottom, appear to fall within the lower categorization of LLW. Considering the symmetry of the curve shape it is probable that the region belonging to the LLW category extends up to around $z = 250$ cm for the top section as well. The remaining sections exhibit minimal residual activation. Overall, the RPV liner demonstrates weak activation, excluding the core vicinity. This condition can be attributed to factors including lower nominal power compared to conventional reactors, a truncated operating lifespan due to the outcome of Italy's referendum for nuclear phase-out in 1987, and an extensive cooling period post-reactor shutdown. This scenario potentially translates into considerable cost reductions in waste disposal from dismantling operations, as lower category waste typically adheres to less stringent regulations. Depending on clearance limits and residual contamination, significant portions of the RPV might qualify as conventional waste, suitable for recycling as metal scraps.

4.5.4 Axial distribution of contact dose rates

The contact γ dose rate was evaluated along with the specific activity in FISPACT. As FISPACT is a 0D code, the default value provided is an approximation based on the semi-infinite slab model, and is calculated as follows:

$$D = C\frac{B}{2}\sum_{i=1}^{N_\gamma}\frac{\mu_a(E_i)}{\mu_m(E_i)}S_\gamma(E_i) \tag{4.2}$$

where N_γ is the number of energy groups in the γ spectrum histogram, E_i is the mean energy of the i-th group, μ_a and μ_m are the mass energy absorption coefficient of air and the mass energy attenuation coefficient of the material, B is the build up factor, S_γ is the γ emission rate, and C is the conversion coefficient to obtain Sv/h. μ_m is calculated as a weighted sum considering the elemental values provided by the library used and the mass share of the element in the material. The source S_γ is evaluated multiplying the emission intensity of energy group i for the activity of the material at the time considered [60].

Similarly to the previous cases, results are reported for the points exhibiting uniform irradiation and those characterised by an angular distribution in Table 4.13 and Table 4.14, respectively.

---

[2] The reason why the error calculated by FISPACT-II in this case is 0 is that this region is so weakly irradiated that essentially no transmutation occurs.

Table 4.13 Calculated contact dose rate D for heights z experiencing uniform irradiation. ΔQ from (2.76).

z/cm	D/(μSv/h)	ΔQ %
454	1.02E-03	0.0^2
-200	2.96E+02	7.3
-250	5.85E+00	7.8
-300	1.61E-01	8.3
-350	6.31E-03	7.3
-393	1.35E-03	2.2

Table 4.14 Angular coordinates θ and calculated contact dose rate D of minimum and maximum fluence points. ΔQ from (2.76).

z/cm	Point	θ/°	D/(μSv/h)	ΔQ %
327	min	70.20	1.14E-02	7.7
	max	88.20	2.20E-02	8.1
277	min	23.40	3.21E-01	8.1
	max	45.00	6.45E-01	8.1
186	min	59.40	8.70E+02	7.1
	max	84.60	1.01E+03	7.1
0	min	63.00	1.38E+05	6.2
	max	16.20	1.93E+05	6.3

The natural background radiation dose rate in Piedmont typically measures around 0.1 μSv/h [75], indicating that numerous regions experience very low levels of irradiation. Consequently, the gamma field generated in these areas does not pose a significant risk to individuals in close proximity. However, regions directly facing the reactor core exhibit a radiation field that could pose potential risks to workers without adequate precautions. For this reason, the dismantling of these specific parts necessitates remote handling, preferably conducted underwater to capitalize on the shielding effect offered by water. This approach aligns with the technological solutions commonly employed in the decommissioning industry, particularly when sufficient working space is available. The reactor cavity is designed to accommodate substantial water volumes during refueling and maintenance tasks, making it suitable for similar usage in decommissioning activities, especially during segmentation processes.

Similarly to previous cases, the calculation was once again conducted under the assumption of uniform irradiation for the points detailed in Table 4.14, and the outcomes are summarized in Table 4.15

Table 4.15 Calculated contact dose rate D for heights z experiencing an angular distribution of the neutron flux under the hypothesis of uniform irradiation. ΔQ from (2.76).

z/cm	$D/(\mu\mathrm{Sv/h})$	ΔQ %
327	1.58E-02	7.9
277	4.94E-01	8.1
186	9.34E+02	7.1
0	1.66E+05	6.3

Contact dose rates calculated under the uniform irradiation hypothesis were compared to the maximum and minimum ones, as summarised in Table 4.16.

Table 4.16 Angular coordinates θ of minimum and maximum fluence points and respective calculated contact dose rate ratios. ΔQ from (2.76) and propagated considering the ratio between the two quantities.

z/cm	Point	$\theta/°$	$\frac{D_{local}}{D_{uniform}}$	Propagated ΔQ %
327	min	70.20	0.72	11.0
	max	88.20	1.39	11.3
277	min	23.40	0.65	11.5
	max	45.00	1.31	11.5
186	min	59.40	0.93	10.0
	max	84.60	1.07	10.0
0	min	63.00	0.82	8.8
	max	16.20	1.16	8.9

The axial distribution of the contact dose rate is displayed in Figure 4.11, only presenting outcomes derived from the assumption of uniform irradiation for all points. This choice was again made to ensure clarity in presentation, given the nature of the logarithmic scale employed: the difference between maximum and minimum values would not be noticeable if represented on the same graph of the low dose rates in regions distant from the core. Notably, in these areas, the contact dose rates are essentially on par with, if not lower than, the ambient natural background radiation levels.

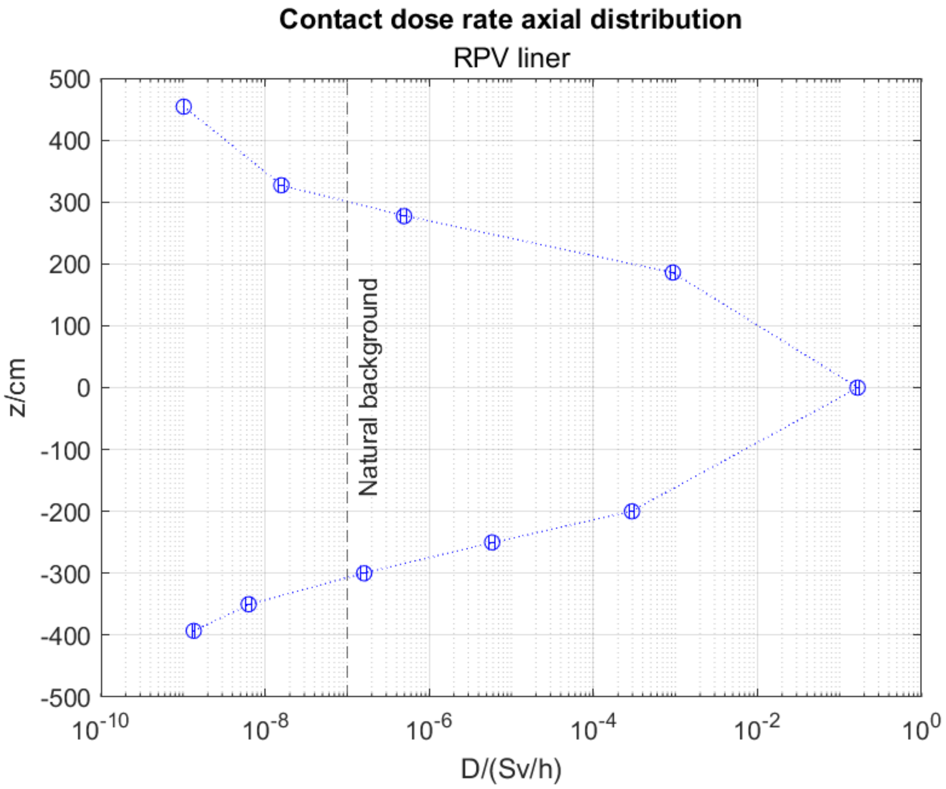

Fig. 4.11 Calculated contact dose rate (D) axial distribution.

Similarly to what happened for both the fluence and the residual activation, the uniform irradiation hypothesis may underestimate the contact dose rates when compared to the maximum points. The most severe underestimations, however, occur for regions exhibiting extremely low levels of dose rates due to the distance from the source. Although the underestimation is not negligible for regions closer to the reactor core, it occurs where the gamma field generated is strong enough already to require special planning. A good example would be $z = 0$ cm: although the uniform 1.66E-01 Sv/h is lower than the maximum value of 1.93E-01 Sv/h, both are significant dose rates, and 1.66E-01 Sv/h by itself already would require radiation protection measures to be implemented. The analysis of the thermal shield also suggests that the scheme provides results that are overestimated by a factor larger than the underestimation introduced by neglecting the angular distribution of the neutron flux. Safety factors larger than the underestimation here estimated are also considered during preliminary shielding design to account for possible uncertainties in the results of calculations or in the measurement campaigns, therefore the more detailed modeling of the angular distribution would likely not be required. A coarser, uniform approach on θ could provide enough information on the magnitude of the residual activation and consequent dose rate expected. On a minor note, the angular distribution shows much smaller gradients in both activation and dose rate compared to the axial distributions, therefore shielding design and waste classification are expected to be more dependent on the latter than on the former.

4.6 Step 4: Validation of the extended model using specific activity measurements

Two different sets of specific activity measurements were considered to validate the results of the extended model: a liner sample and a series of dosimeters.

4.6.1 Liner sample

The first set was created analysing a liner sample removed from the internal surface of the RPV, which was collected 20 days after the end of the sixth cycle, on 10/06/1977, around 4.5 m below the flange (corresponding to $z = -25.65$ cm) at $\theta = 225°$[27]. The analysis was performed on 15/06/1977 and focused on the following isotopes: ^{51}Cr, ^{54}Mn, ^{58}Co, ^{59}Fe and ^{60}Co. The irradiation history experienced by this sample is therefore the same as the one reported in Table 4.8, up to step number 22. The irradiation was then followed by a cooling time of 26 days before the analysis was performed. Neutron fluxes and spectra were evaluated using the same methodology described in the previous chapters for $z = 0$ cm, considering the proximity to the core region of the sampling location, which required the separate analysis of the first cycle. Comparisons were performed using the C/M ratio, as was the case in Chapter 3. The results are reported in Table 4.17.

Only the uncertainty belonging to the FISPACT-II calculation is reported, as no experimental error is available. As can be seen from Table 4.17, all C/M ratios belong to the 1-10 acceptability interval and overall the comparison can be considered satisfactory and conservative. ^{54}Mn and ^{58}Co are typically generated by interaction of their respective precursors with the fast flux, while the other isotopes are generated by radiative capture of thermal neutrons. The calculation scheme therefore appears to perform well both in the thermal and fast neutron range.

Table 4.17 Residual activation of the liner sample. Measurements from [27]. ΔQ from (2.76).

Isotope	C/(Bq/g)	ΔQ %	M/(Bq/g)	C/M
^{51}Cr	2.26E+08	3.44	9.12E+07	2.48
^{54}Mn	2.92E+06	10.40	2.27E+06	1.29
^{58}Co	5.85E+06	10.67	4.03E+06	1.45
^{59}Fe	4.67E+06	3.46	2.09E+06	2.23
^{60}Co	2.87E+07	6.16	8.72E+06	3.29

4.6.2 Dosimeters

The second set of experimental data considered for validation is formed by five activation foil dosimeters irradiated during the seventh cycle, from 01/08/77 to 19/01/79, in the framework of the vessel surveillance program performed by plant operators. The foils were positioned on the central axis of the reactor, 27.6 cm below the end of the active zone ($z = -160.4$ cm) [27]. They were made of silver, cobalt, iron, nickel and tantalium and the reaction of interest are listed in Table 4.18.

Table 4.18 Activation foils compositions and reactions of interest [27].

Precursor	Reaction	Product
^{109}Ag	n,γ	^{110m}Ag
^{59}Co	n,γ	^{60}Co
^{54}Fe	n,p	^{54}Mn
^{58}Ni	n,p	^{58}Co
^{181}Ta	n,γ	^{182}Ta

The neutron flux was evaluated using a spherical track length detector of radius 5 cm and the neutron flux energy spectrum was evaluated using a disk-shaped detector 25 cm in radius and 10 cm in height to ensure high spectrum accuracy. The results of the comparisons are listed in Table 4.19.

All C/M ratios belong to the acceptability interval. As was the case with the liner sample, the scheme performs well both in the thermal and fast neutron regions, since ^{58}Co and ^{54}Mn are fast activation products, while the others are generated by radiative capture of thermal neutrons.

Table 4.19 Residual activation of the dosimeters. Measurements from [27]. ΔQ from (2.76).

Isotope	C/(Bq/g)	ΔQ %	M/(Bq/g)	C/M
^{110m}Ag	1.85E+10	1.34	4.60E+09	4.01
^{60}Co	1.05E+11	6.35	2.61E+10	4.02
^{54}Mn	1.23E+07	10.53	1.04E+07	1.19
^{58}Co	2.52E+08	11.16	2.26E+08	1.12
^{182}Ta	1.14E+11	11.57	6.07E+10	1.87

4.7 Main remarks

The calculation scheme initially developed for the analysis of the thermal shield was modified and expanded to encompass the entire operational life of the reactor. It was then applied to the analysis of the RPV internal liner, as the RPV is the largest and most difficult component to dismantle and the stainless-steel liner is prone to activation due to the significant nickel content.

The scheme was used to evaluate the residual activation and contact dose rate at several locations with different combinations of radial, angular and axial coordinates, and characterised by different irradiation histories. For example both the datasets used for validation were characterised by a different irradiation history compared to the thermal shield, proving that the model performs well with different boundary conditions and is flexible enough to adapt to the user's requirements.

Chapter 5

Representative Operating Cycle (ROC) approach

The hybrid calculation scheme developed and discussed in the previous Chapters proved to be effective, but its implementation is not straightforward. There are many modeling choices involved in the definition of the cores to be analysed and the overall procedure seems suited more for research purposes than industrial needs. The decommissioning of nuclear plants is an industrial task, and therefore it could usually benefit more from a quicker, although coarser, result than from a lengthy, detailed analysis, as time is one of the main constraints in this type of activity. This is the reason why the previously mentioned ROC approach is favored: it allows a quick characterization of the most important components without excessive use of computational resources. The drawback of this approach is that it is generally suggested for reactors characterised by a very steady operation and little to no modifications in terms of geometry or other significant features, and may involve many approximations [28].

Most nuclear reactors nowadays have standardized designs and are operated at full, constant power for most of the time, in order to cover the need for baseload electricity. The high capacity factor and constant operation with minor or no modifications at all makes them ideal for the ROC approach, but this was not the case of the Trino reactor at all, as was illustrated in the previous Chapters: especially the core overhaul after the first cycle introduced significant changes that affected the fluence, residual activation and contact dose rate distributions.

Nevertheless, since the hybrid approach proposed performed well and it was essentially developed applying the ROC hypothesis to subsets of the reactor's operational life, the same approach was used once again but in its coarser form. The aim in this case was to assess the performance of this approximation when applied to a reactor that does not appear to be particularly suitable for this kind of analysis.

5.1 ROC selection

In order to select which of the four cores defined is the most suitable to be used as ROC, a fluence analysis has been performed. Across all the points of the RPV liner analysed, the average % fluence distribution is the one reported in Table 5.1.

Table 5.1 Average % fluence distribution.

	1^{st} core	2^{nd} core	3^{rd} core	4^{th} core
% fluence	13.5	26	12.3	48.2

It is clear from the data reported in Table 5.1 that the core configuration responsible for most of the neutron fluence in the hybrid model developed is the fourth one, which approximates cycles from 6 to 9 and accounts for almost half of the total. Moreover, this core configuration is quite similar to the previous one, used for cycle 5, which shares the same geometry although not the same enrichments. These two configurations combined are responsible for around 60% of the total fluence, therefore they are the best available options for a ROC analysis. The fourth core in particular seemed the most suited and was therefore selected as ROC for the following analysis.

5.2 Adaptation of the reconstructed irradiation history

The reconstructed irradiation history used for the analysis of the RPV liner and reported in Table 4.8 assumed a nominal power of 825 MW_{th} for cycles from 1 to 3 since the reactor was allowed to operate at 870 MW_{th} only from the fourth cycle on. The neutron source generated with the fourth core was normalised at 870 MW_{th}, therefore, in order to keep constant the thermal energy released in each cycle, the $\frac{P}{P_{nominal}}$ ratios for cycles 1 to 3 had to be scaled down, while keeping all the other parameters constant. The rescaled factors are listed in Table 5.2. No modification was introduced for cycles from 4 to 9, as the source was already normalised at 870 MW_{th} in the previous analysis.

Table 5.2 Reconstructed irradiation history for cycle 1 to 3 under the ROC approximation. No modification was introduced for cycles from 4 to 9, therefore for these cycles the reference irradiation history is the same listed in Table 4.8.

Cycle	$P_{nominal}/\mathrm{MW}_{th}$	Step	t/d	$\frac{P}{P_{nominal}}$	E_{th}/MWd
1	870	1	225	0.49	460267
		STOP	87	0	
		2	260	0.68	
		STOP	53	0	
		3	295	0.82	
		STOP	998	0	
2	870	4	22	0.32	302956
		STOP	97	0	
		5	24	0.34	
		6	19	0.95	
		7	13	0.37	
		8	225	0.93	
		9	39	0.45	
		10	90	0.93	
		STOP	78	0	
3	870	11	10	0.89	365186
		STOP	38	0	
		12	151	0.88	
		13	32	0.39	
		14	175	0.91	
		STOP	7	0	
		15	40	0.94	
		16	103	0.66	
		STOP	96	0	

5.3 Activation results with the ROC approach

The entire procedure used for the analysis of the thermal shield and the RPV liner was repeated, this time in its approximated form. In principle the angular distribution of the final fluence could be affected, and therefore residual activation and dose rates, as in this case they depend only on the angular flux profile generated by the fourth core. The positions of the maximum and minimum points for the heights exhibiting an angular profile may be different, but this effect, while possible in theory, is strongly mitigated by the much longer time the reactor operated under the conditions set by the fourth core, as can be seen in Figure 5.1, where the total fluences under the ROC hypothesis are compared to the ones calculated in Chapter 4 with the hybrid model.

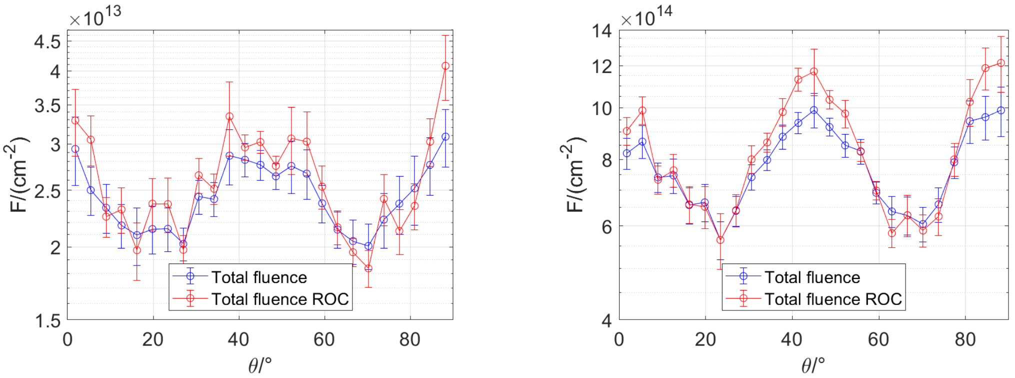

(a) $z = 327$ cm.

(b) $z = 277$ cm.

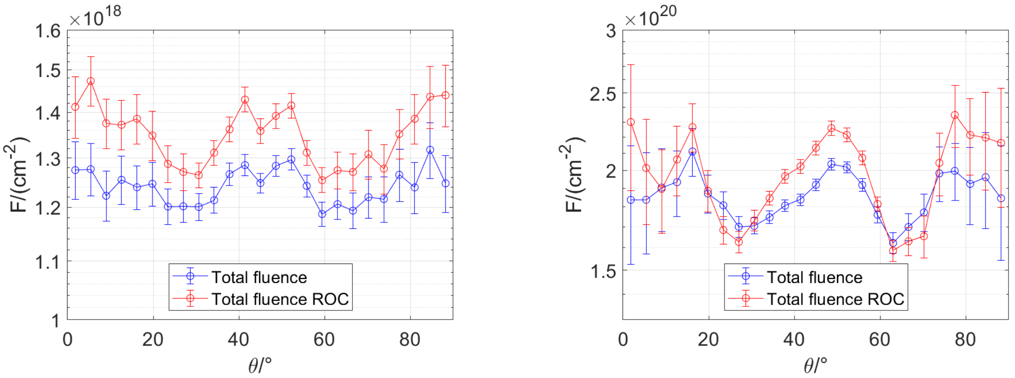

(c) $z = 186$ cm.

(d) $z = 0$ cm.

Fig. 5.1 Total fluence for heights exhibiting an angular profile of the neutron flux under the ROC hypothesis compared to the total fluence computed using the hybrid model.

In fact, the total fluence computed using the hybrid approach already exhibits a shape that suggests a strong prevalence of the irradiation conditions set by the second, third and fourth cores. This aspect is in line with the analysis of the % fluence distribution. The effects of the different geometry of the first cycle were progressively reduced by the more conventional operation that characterised the second half of the reactor's life. This pattern is expected for the residual activation and the contact dose rates as well, similarly to the previous cases analysed.

Considering the limited differences introduced by treating the regions characterised by an angular flux profile as uniformly irradiated, as the previous analyses suggested, residual activations and dose rates were evaluated assuming a uniform, average neutron flux for all heights. The results of the analysis of the RPV under the ROC approximation are reported in Sections 5.3.1 and 5.3.2.

5.3.1 Residual activation

The axial profile of the residual activation is visible in Figure 5.2, and the ratios between the values calculated with the ROC hypothesis and the hybrid model are reported in Figure 5.3.

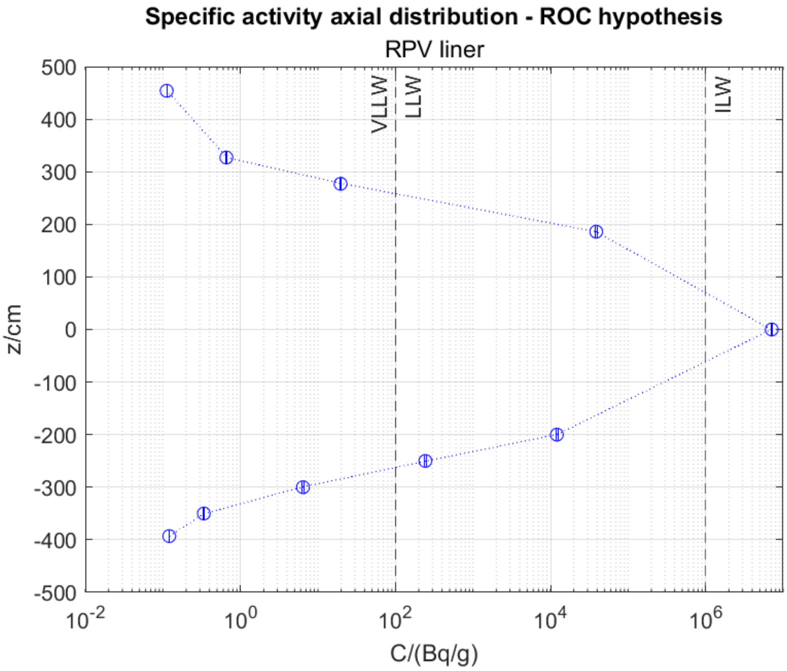

Fig. 5.2 Calculated specific activity (C) axial distribution under the ROC hypothesis.

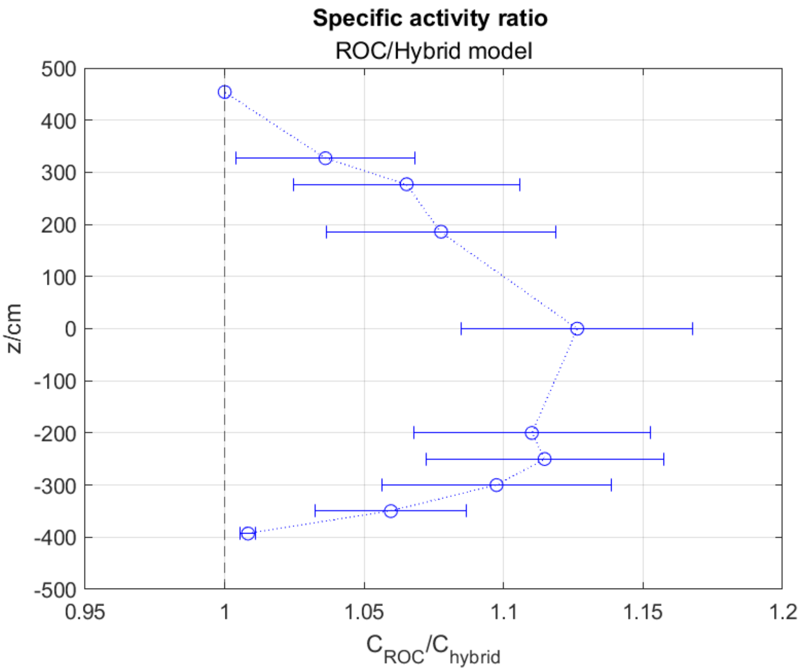

Fig. 5.3 Axial distribution of the ratio between the specific activity calculated with the ROC approach (C_{ROC}) and the one calculated with the hybrid model (C_{hybrid}).

The ROC approximation does not seem to introduce significant errors, as the maximum relative difference occurs around the central part of the reactor and is around 13-15%. For most heights, the relative difference is lower than or around 10%. Overall, the error introduced could be acceptable, especially considering the analysis of the entire operational life of the reactor and the sources of uncertainties described in Section 3.4, which affect these calculations as well.

5.3.2 Contact dose rates

The axial profile of the contact dose rate is available in Figure 5.4, and the ratios between the values calculated with the ROC hypothesis and the hybrid model are reported in Figure 5.5.

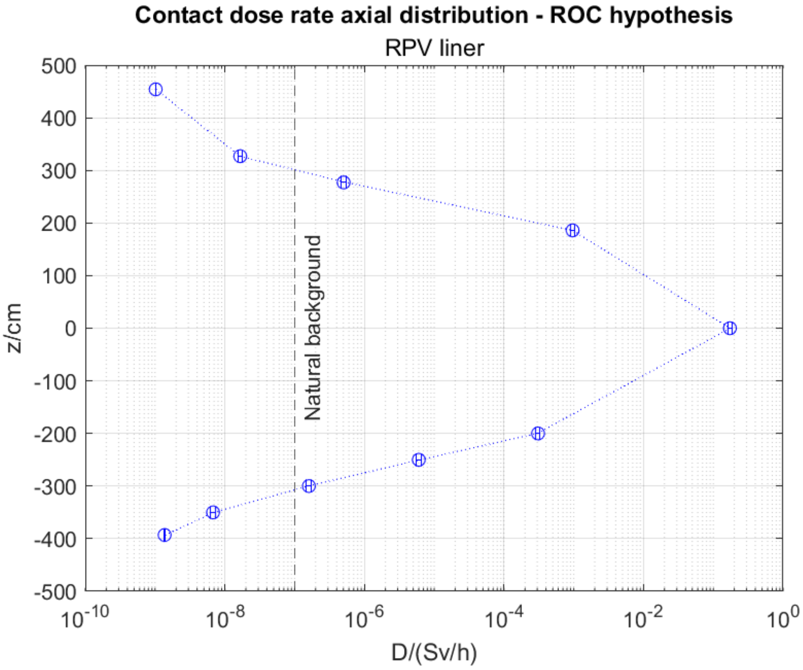

Fig. 5.4 Contact dose rate axial distribution under the ROC hypothesis.

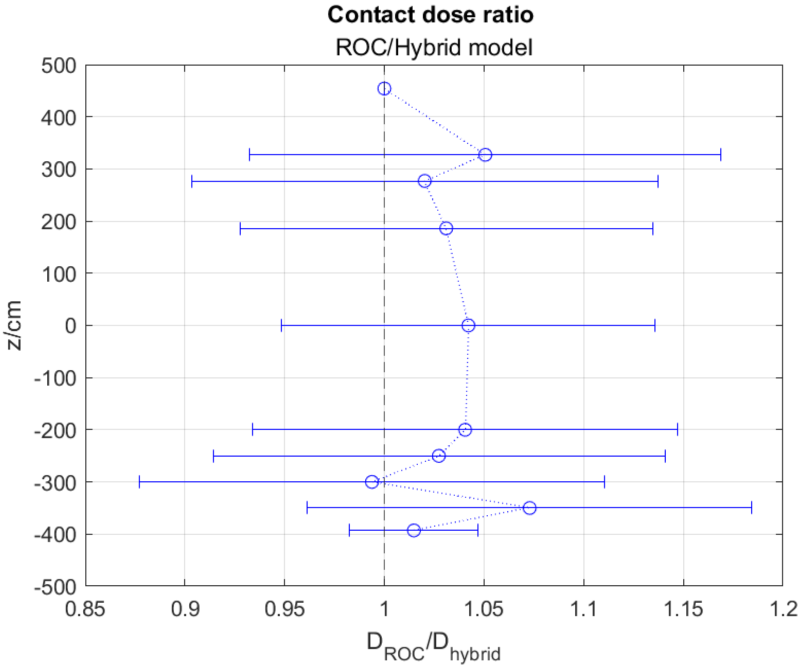

Fig. 5.5 Axial distribution of the ratio between the contact dose rate calculated with the ROC approach and the one calculated with the hybrid model.

As visible in Figure 5.5, the overestimation in the case of the contact dose rate is mostly acceptable, as the maximum relative difference is around 7%. The graph suggests that the two approaches are very similar in assessing the contact dose rates. As previously suggested, the overestimation in the central part of the reactor would not impact significantly the development of a decommissioning strategy, as it occurs in regions with a significant dose rate already. This gamma field would require remotely-operated equipment and possibly underwater cutting anyway.

5.3.3 Main remarks

The ROC hypothesis has been tested and compared to the hybrid model previously developed. This approach appears to work well, although it is based exclusively on the fourth core developed in the framework of the previous analysis detailed in Chapter 4, which implies that the particular configuration of the first cycle is completely neglected. This introduces two notable approximations:

- The different neutron flux angular distribution of the first cycle is not considered, which could potentially impact the fluence distribution and might change the coordinates of the maximum and minimum fluence and residual activation points. This effect, nevertheless, appears to be negligible, as discussed in Section 5.3.
- The lack of a separate treatment for the first operating cycle implies that its neutron flux energy spectra are not considered. This is not a significant issue for most points, as there is very little variation between the spectra of different cycles for a given specific height, which is the reason behind the averaging process discussed in Section 4.5.1. Nevertheless, this reasoning does not hold true for the points at $z = 0$ cm. These points are the only ones that required a slightly more complex analysis in the hybrid model, as the presence of the thermal shield impacts the energy distribution of the neutrons interacting with the RPV. In the case of the ROC hypothesis, therefore, the neutron flux energy spectrum used for the points at $z = 0$ cm corresponds to the spectrum of the fourth core, and it exhibits a higher thermal peak, since the presence of the shield is neglected. This approximation, nevertheless, is deemed acceptable, as a more thermalised spectrum leads to a slightly higher residual activation,

because most activation products are generated in the thermal range. The approximations should therefore produce conservative results.

Chapter 6

Conclusions and future work

The decommissioning of nuclear power reactors and, more in general, nuclear related facilities, is a multidisciplinary, decade-long task that is only currently starting to be completely understood. The abundance of parameters to be considered in the development of a decommissioning strategy for an NPP is noteworthy: type of reactor, materials used, component thickness, working space available, residual activity of the structures and consequent gamma ray fields, operational history of the plant, cost and regulations. The most challenging tasks are typically encountered during the dismantling of the large components of the reactor, in particular the RPV and RVI. This difficulty stems from the large size and radioactive environment that requires special planning and safety procedures. The distribution of the structural residual activation and the consequent radiation field is the parameter that affects the most the difficulty of the operations, hence why modeling activities play a significant role in the optimization process of the entire procedure.

In the context of this thesis a MC four-step calculation scheme has been developed to evaluate the residual activation in the supporting structures of the PWR at the Enrico Fermi NPP in Trino, Italy.

The scheme has been developed using mainly MC techniques, although there are some elements of deterministic analysis and therefore it is not entirely statistical in nature. More in detail, the solver used to compute the cell importance in the accelerated transport simulations detailed in Chapter 3 is based on the Response Matrix Method, which is a deterministic technique. Moreover, the calculation of the concentration of radioactive nuclides has been performed using FISPACT-II, which is based on the solution of the Bateman equations, as detailed in Section 2.5, despite the possibility of performing the calculation with Serpent 2.

The scheme has been initially applied to the thermal shield of the reactor, an internal component removed at the end of the first operating cycle. This choice stemmed from the availability of two sets of residual activation measurements gathered during two different sampling campaigns performed in 1969 and 1992. The measurements, although collected for industrial purposes and therefore without a clear experimental set up, proved to be extremely valuable for the validation of the scheme, as they allowed to assess the scheme performance in the evaluation of the concentration of different radioactive species. The scheme performed well and was able to correctly estimate most of the experimental values, except for one isotope in one occasion. The possible reason for this mismatch has been discussed in Section 3.5. In most cases, the estimated values are quite close to the measurements, which is an encouraging result, specially considering all the uncertainties involved in the overall procedure, such as the ones related to nuclear data, geometry, experimental error bars, statistics, data processing between different codes and so on.

The scheme has been afterwards expanded and modified to analyse the RPV, notably the largest and most difficult component to dismantle. The main focus has been the stainless steel internal liner, as it contains large amounts of nickel, which is particularly prone to activate under thermal neutron irradiation. Ten heights were considered to study the axial distribution of the residual activation and contact dose rates. Initially, for all heights, the analysis of the angular distribution of the neutron flux was performed, using 25 or 23 angular bins. The modifications introduced after the first operating cycle altered significantly the neutron flux angular profile, and this effect had to be considered in the evaluation of the residual activation. After a few preliminary calculations, it was clear that not all heights exhibited a significant variation in the angular profile of the neutron flux. More in detail, only the analysed heights in the proximity of the core were characterised by clear maximum and minimum flux points, whereas the others exhibited mostly uniform irradiation. The differences between the modeling approach and its effect on the results were discussed in Section 4.4.

The scheme has been validated a second time in its modified form used for the analysis of the RPV liner using two different sets of measurements available. The first set belongs to a 1977 sampling activity performed on the liner itself. The second set is formed by five activation foils used for the surveillance program of the RPV and analysed in 1979. This second validation activity proved that the scheme in its modified form is able to correctly estimate the residual activation of the structures under analysis, despite the different combination of simulation parameters considered, e.g. a different operational history, much longer than the one that characterised the thermal shield. It has been possible as well to test the scheme performance on the evaluation of new, different isotopes, proving its good flexibility and its worth as a supporting tool for the optimization of the decommissioning plans. Overall, the scheme proved robust, as it was able to yield satisfying results analyzing several points in different positions in the reactor, with different combinations of isotopes and irradiation conditions, without overestimating the power.

The scheme was eventually modified a third time to assess the effectiveness of a much simpler hypothesis, the Representative Operating Cycle (ROC), which is usually recommended for the radiological analysis of power plants characterised by few modifications and a relatively constant operation. This is not the case of the Trino NPP, which had a much more complex history. Nevertheless, it was deemed interesting to compare the results of the analysis performed with the hybrid model developed, which originally encompassed the analysis of four different cores, with the one performed under this ROC hypothesis, in order to assess its effectiveness considering the much lower computational cost and shorter implementation time.

The results of the analysis are encouraging, as under the ROC hypothesis the results were only slightly overestimated compared to the original hybrid model. The overestimation does not appear to be significant, both in terms of residual specific activity and contact dose rate. This suggests that this hypothesis, despite its numerous approximations such as the lack of a separate analysis for the first cycle, which impacts the neutron flux angular distribution, is a powerful and inexpensive tool to assess the radiological conditions of the supporting structures even in plants characterised by a complex operation. Considering that decommissioning activities are essentially an industrial practice, quick, although less detailed results, may be preferable in many cases to extensive and lengthy analyses that provide more details but at greater cost.

Of course the advantages of a purely research-oriented analysis performed with only MC tools are reduced by the set of methods and simplifications applied, such as using FISPACT which does not consider statistical uncertainty and requires energy averaging of the cross sections, the volume averaging of neutron flux energy spectra, or the application of the RoC method. Despite all these aspects, the results proved useful for the radiological characterization of the Trino reactor.

The dismantling of nuclear related facilities, either power plants or factories belonging to the fuel cycle, represents a growing market for companies offering highly skilled engineering services. The correct treatment of decommissioning activities and subsequent radioactive waste management stands therefore as a growing business field which will gain importance in the decades to come given the progressive aging of the world nuclear fleet. Modeling activities revolving around the characterization of reactors and supporting structures are therefore projected to play a fundamental role in the development and growth of the industry.

The developed scheme, either in its original hybrid form or if the ROC approximation is considered, could be used to analyse virtually every component of the Trino reactor, considering its 3D nature and flexibility in terms of spectra and operational history used. Future work on these topic include the expansion of the domain to encompass other, further components, such as the neutron shield tank and the concrete bioshield of the reactor pit. This would allow to expand the analysis and take advantage of the accelerated transport to investigate regions further away from the core, that nevertheless require some level of knowledge in terms of residual activation before dismantling, e.g. the bioshield concrete or steel rebar. It would be also possible to analyse the radial profile of the residual activation inside the RPV bulk, which is affected by different neutron flux energy spectra. Initially, from the inside to the outside, the spectrum becomes progressively less thermalised, as neutrons impact on the steel structure. On the outer side instead the spectrum becomes more thermalised again, due to the presence of water inside the neutron shield tank that acts as a moderator for backscattered neutrons.

This activity could be performed in parallel with the actual decommissioning of the plant, which is currently ongoing: the primary circuit and its pumps have already been dismantled, and the RPV and RVIs are going to be segmented in the next few years. The opening of the reactor head would allow to perform more samplings of the structures, which would provide new, more rigorous data for further validation. It would be interesting to continue the comparisons between the calculated and measured results, in order to identify areas in the scheme that may require improvements.

One such area that could be addressed further is the uncertainty estimation, as the the effect of using different nuclear data or simplification hypothesis would be worth investigating. This activity would allow to refine the scheme and make it more precise, taking into account a more comprehensive set of parameters that could affect the results.

The model, with the proper modifications, could also be used to analyse other PWRs, if all the information in terms of geometry, materials, enrichments, and all the other parameters discussed in the framework of this Thesis, were provided. If required, the scheme could also be expanded to encompass the analysis of the gamma field generated by the activation products, as photons are neutral particles that could be treated similarly to neutrons for many aspects (e.g. generation, accelerated transport, interaction with a target).

The calculation scheme itself is in principle valid for other types of reactors as well, although in order to be used for other plants new geometrical and neutronic models should be developed. It would be possible, for example, to substitute the model of the Trino reactor with the model of one of the BWRs that have to be decommissioned (i.e. the Garigliano or Caorso reactors). Although the creation ex novo of these new models could be relatively time consuming, the global architecture of the scheme remains valid and could be exploited for the analysis of other plants.

References

[1] Ember. *Distribution of electricity generation worldwide in 2022, by energy source*. https://www.statista.com/statistics/269811/world-electricity-production-by-energy-source/ [Accessed: (06/02/2024)].

[2] IAEA. *Power Reactor Information System - PRIS*. https://pris.iaea.org/pris/ [Accessed: (05/02/2024)].

[3] S. Marguet. *The Technology of Pressurized Water Reactors*. Vol. 1. Springer, 2022. DOI: https://doi.org/10.1007/978-3-030-86638-9.

[4] W. M. Stacey. *Nuclear Reactor Physics*. Wiley, 2007. ISBN: 9783527406791. URL: https://books.google.it/books?id=y1UgcgVSXSkC.

[5] M. Matsuura et al. “Features of BWR plant”. In: *Boiling Water Reactors: Volume 4*. Vol. 4. 2023, pp. 59–165. ISBN: 9780128213612. DOI: 10.1016/B978-0-12-821361-2.00001-5.

[6] T. W. Kerlin and B. R. Upadhyaya. “Chapter 14 - Pressurized heavy water reactors”. In: *Dynamics and Control of Nuclear Reactors*. Ed. by Thomas W. Kerlin and Belle R. Upadhyaya. Academic Press, 2019, pp. 191–202. ISBN: 978-0-12-815261-4. DOI: https://doi.org/10.1016/B978-0-12-815261-4.00014-7. URL: https://www.sciencedirect.com/science/article/pii/B9780128152614000147.

[7] P. Breeze. “Chapter 5 - Gas-Cooled Reactors”. In: *Nuclear Power*. Ed. by Paul Breeze. Academic Press, 2017, pp. 45–51. ISBN: 978-0-08-101043-3. DOI: https://doi.org/10.1016/B978-0-08-101043-3.00005-5. URL: https://www.sciencedirect.com/science/article/pii/B9780081010433000055.

[8] E. Midgley and J. Burge. *Nuclear Decommissioning Market Set to Boom*. https://www.iaea.org/bulletin/nuclear-decommissioning-market-set-to-boom [Accessed: (05/02/2024)].

[9] J. C. Evans et al. *Long-Lived Activation Products in Reactor Materials–NUREG/CR-3474*. Tech. rep. Pacific Northwest Laboratory, prepared for the U.S. Nuclear Regulatory Commission, 1984.

[10] *ITER*. https://www.iter.org/ [Accessed: (07/03/2024)].

[11] K. Mergia and N. Boukos. “Structural, thermal, electrical and magnetic properties of Eurofer 97 steel”. In: *Journal of Nuclear Materials* 373.1-3 (2008), pp. 1–8. ISSN: 00223115. DOI: 10.1016/j.jnucmat.2007.03.267.

[12] M. Zmitko et al. “The European ITER Test Blanket Modules: EUROFER97 material and TBM’s fabrication technologies development and qualification”. In: *Fusion Engineering and Design* 124 (2017), pp. 767–773. ISSN: 09203796. DOI: 10.1016/j.fusengdes.2017.04.051. URL: https://doi.org/10.1016/j.fusengdes.2017.04.051.

[13] D. A. Brown, M. B. Chadwick, R. Capote, et al. “ENDF/B-VIII.0: The 8^{th} Major Release of the Nuclear Reaction Data Library with CIELO-project Cross Sections, New Standards and Thermal Scattering Data”. In: *Nuclear Data Sheets* 148 (2018). Special Issue on Nuclear Reaction Data, pp. 1–142. ISSN: 0090-3752. DOI: https://doi.org/10.1016/j.nds.2018.02.001. URL: https://www.sciencedirect.com/science/article/pii/S0090375218300206.

[14] NEA Data Bank. *JEFF-3.2*. https://www.oecd-nea.org/dbforms/data/eva/evatapes/jeff_32/ [Accessed: (05/02/2024)].

[15] M. R. Gilbert and J. C. Sublet. *Handbook of activation, transmutation, and radiation damage properties of the elements simulated using FISPACT-II and TENDL-2014; Nuclear Fission plants (HFR focus)*. 2015. URL: https://fispact.ukaea.uk/wp-content/uploads/2016/10/Handbook_HFR_UKAEA1532.pdf.

[16] P. Pospíšil. “Reactor Vessel Internals Segmentation Experience using Mechanical Cutting Tools”. In: *Technological Engineering* 10.2 (2013), pp. 6–10. DOI: 10.2478/teen-2013-0012.

[17] J. Boucau, P. Segerud, and M. Sanchez. “Best practices for preparing vessel internals segmentation projects”. In: *PREDEC 2016* (2016), pp. 1–7.

[18] L. Santiago. “Dismantling large components at the José-Cabrera NPP (CNJC) in Spain”. In: *Nea/Rwm/R(2-18)8* (2012), pp. 77–81. URL: http://www.iaea.org/inis/collection/NCLCollectionStore/_Public/45/073/45073552.pdf.

[19] L. Johansson. “Possible means to manage and store the BKAB RPV”. In: *OECD NEA* (2012). URL: https://inis.iaea.org/collection/NCLCollectionStore/_Public/45/073/45073553.pdf.

[20] P. Segerud. “Breaking up Barsebäck”. In: *Nuclear Engineering International* (2018).

[21] Sogin. *Private communications*. Tech. rep. Sogin, 2021.

[22] Sogin. *Deposito Nazionale*. https://www.depositonazionale.it/ [Accessed: (05/02/2024)].

[23] Italian Ministry of Environment. *Decreto 7 agosto 2015 - Classificazione dei rifiuti radioattivi, ai sensi dell’articolo 5 del decreto legislativo 4 marzo 2014, n. 45*. 2015.

[24] *CIRTEN*. http://www.cirten.it/ [Accessed: (05/02/2024)].

[25] *Sogin*. https://sogin.it/en [Accessed: (05/02/2024)].

[26] Sogin. *Rapporto Decennale sullo Stato di Conservazione di Trino*. Tech. rep. Sogin, 1977.

[27] M. Genova, E. Penno, and G. Vimercati. *Disattivazione Trino: inventario della radioattività residua dovuta ad attiv azione neutronica. Rapporto finale CISE-DSM-95-13*. Tech. rep. CISE, 1995.

[28] M. Pantelias Garcés. "Activation Neutronics for the Swiss Nuclear Power Plants". PhD thesis. ETH, 2013. ISBN: 8610828378018.

[29] J. J. Duderstadt and L. J. Hamilton. *Nuclear Reactor Analysis*. Wiley, 1976. ISBN: 978-0-471-22363-4.

[30] A. M. Weinberg and E. P. Wigner. *The Physical Theory of Neutron Chain Reactors*. University of Chicago Press, 1958.

[31] S. Glasstone and A. Sesonske. *Nuclear Reactor Engineering*. D. Van Nostrand Company Inc., 1963.

[32] G. I. Bell and S. Glasstone. *Nuclear Reactor Theory*. New York: Van Nostrand Reinhold, 1970.

[33] R. J. J. Stammler and M. J. Abbate. *Methods of Steady-State Reactor Physics in Nuclear Design*. Academic Press Inc., 1983.

[34] J. Lewins. *Importamce: the adjoint function. The physical basis of variational and perturbation theory in transport and diffusion problems*. 1965.

[35] E. E. Lewis and W. F. Miller. *Computational methods of neutron transport*. Wiley, Jan. 1984. URL: https://www.osti.gov/biblio/5538794.

[36] S. Ahn et al. *Methodologies for Assessing the Induced Activation Source Term for Use in Decommissioning Applications*. Tech. rep. 95. IAEA, 2019. URL: https://www-pub.iaea.org/MTCD/Publications/PDF/P1823_web.pdf.

[37] I. Lux and L. Koblinger. *Monte Carlo Particle Transport Methods : Neutron and Photon Calculations*. CRC Press, 1991. ISBN: 0849360749.

[38] E. F. Love, K. A. Pauley, and B. D. Reid. "Use of MCNP for characterization of reactor vessel internals waste from decommissioned nuclear reactors". In: *Idaho National Engineering Laboratory* (1995).

[39] L. Schlömer, P. W. Phlippen, and B. Lukas. "Activation calculation for the dismantling and decommissioning of a light water reactor using MCNP™ with ADVANTG and ORIGEN-S". In: *EPJ Web of Conferences* 153 (2017). DOI: 10.1051/epjconf/201715305020.

[40] P. W. Phlippen et al. "Numeric determination and validation of neutron-induced radioactive nuclide inventories for decommissioning and dismantling of light water reactors". In: *Nuclear Technology* 201.1 (2018), pp. 66–79. ISSN: 00295450. DOI: 10.1080/00295450.2017.1399039. URL: https://doi.org/10.1080/00295450.2017.1399039.

[41] M. Šnírer et al. "Validation of Monte Carlo activation calculation for V1 NPP reactor concrete shaft". In: *Annals of Nuclear Energy* 163 (2021). ISSN: 18732100. DOI: 10.1016/j.anucene.2021.108556.

[42] Y. Zheng. "7 - The discrete ordinate method". In: *Deterministic Numerical Methods for Unstructured-Mesh Neutron Transport Calculation*. Ed. by Liangzhi Cao and Hongchun Wu. Woodhead Publishing Series in Energy. Woodhead Publishing, 2021, pp. 167–213. ISBN: 978-0-12-818221-5. DOI: https://doi.org/10.1016/B978-0-12-818221-5.00009-X.

[43] B. G. Carlson. "A Method of Characteristics and Other Improvements in Solution Methods for the Transport Equation". In: *Nuclear Science and Engineering* 61.3 (1976), pp. 408–425. DOI: 10.13182/NSE76-A26927.

[44] J. R. Askew. *A characteristics formulation of the neutron transport equation in complicated geometries*. Tech. rep. United Kingdom Atomic Energy Authority, 1972.

[45] S. Santandrea and P Mosca. "Linear surface characteristic scheme for the neutron transport equation in unstructured geometries". In: *PHYSOR 2006*. Sept. 2006.

[46] Z. Liu. "5 - The method of characteristics". In: *Deterministic Numerical Methods for Unstructured-Mesh Neutron Transport Calculation*. Ed. by Liangzhi Cao and Hongchun Wu. Woodhead Publishing Series in Energy. Woodhead Publishing, 2021, pp. 73–108. ISBN: 978-0-12-818221-5.

[47] I. Zmijarevic et al. "Use of 2D whole core reactor models for PWR analysis with APOLLO2". In: *PHYSOR 2008*. Vol. 2. Sept. 2008, pp. 1353–1360.

[48] J. Leppänen et al. "The Serpent Monte Carlo code : Status, development and applications in 2013". In: *Annals of Nuclear Energy* 82 (2015), pp. 142–150. DOI: 10.1016/j.anucene.2014.08.024.

[49] S. Mosher. "A New Version of the ADVANTG Variance Reduction Generator". In: *RPSD 2010 Topical Meeting* (2010).

[50] J. C. Wagner and A. Haghighat. "Automated variance reduction of Monte Carlo shielding calculations using the discrete ordinates adjoint function". In: *Nuclear Science and Engineering* 128.2 (1998), pp. 186–208. ISSN: 00295639. DOI: 10.13182/NSE98-2.

[51] R. R. Coveyou, V. R. Cain, and K. J. Yost. "Adjoint and Importance in Monte Carlo Application". In: *Nuclear Science and Engineering* 27.2 (1967), pp. 219–234. ISSN: 0029-5639. DOI: 10.13182/nse67-a18262.

[52] X. Fan, G. Zhang, and K. Wang. "Development of new variance reduction methods based on weight window technique in RMC code". In: *Progress in Nuclear Energy* 90 (2016), pp. 197–203. ISSN: 0149-1970. DOI: https://doi.org/10.1016/j.pnucene.2016.03.023. URL: https://www.sciencedirect.com/science/article/pii/S0149197016300695.

[53] K. A. Van Riper et al. *Avatar – Automatic Variance Reduction in Monte Carlo Calculations*. Tech. rep. 836. Los Alamos National Laboratory, 1997.

[54] J. A. Kulesza et al. *MCNP® Code Version 6.3.0 Theory & User Manual*. Tech. rep. LA-UR-22-30006, Rev. 1. Los Alamos National Laboratory, 2022.

[55] J. Leppänen. “Response Matrix Method–Based Importance Solver and Variance Reduction Scheme in the Serpent 2 Monte Carlo Code”. In: *Nuclear Technology* 205.11 (2019), pp. 1416–1432. ISSN: 19437471. DOI: 10.1080/00295450.2019.1603710. URL: https://doi.org/10.1080/00295450.2019.1603710.

[56] J. C. Wagner, E. D. Blakeman, and D. E. Peplow. “Forward-weighted CADIS method for global variance reduction”. In: *Transactions of the American Nuclear Society* 97 (2007), pp. 630–633. ISSN: 0003018X.

[57] J. Leppänen, T. Viitanen, and O. Hyvönen. “Development of a Variance Reduction Scheme in the Serpent 2 Monte Carlo Code”. In: *M&C 2017*. September. 2017.

[58] A. G. Croff. “ORIGEN2: A versatile computer code for calculating the nuclide compositions and characteristics of nuclear materials”. In: *Nuclear Technology* 62:3 (Sept. 1983). URL: https://www.osti.gov/biblio/5421763.

[59] J. C. Sublet et al. “FISPACT-II: An Advanced Simulation System for Activation, Transmutation and Material Modelling”. In: *Nuclear Data Sheets* 139 (2017), pp. 77–137. ISSN: 00903752. DOI: 10.1016/j.nds.2017.01.002. URL: http://dx.doi.org/10.1016/j.nds.2017.01.002.

[60] UKAEA. *The FISPACT-II User Manual*. 2018. URL: https://fispact.ukaea.uk/_documentation/UKAEA-R18001.pdf.

[61] L. W. Packer and J. C. Sublet. *The European Activation File: EAF-2010 decay data library*. Tech. rep. Culham Centre for Fusion Energy, 2010.

[62] Eastwood, J. W. and Guy Morgan, J. *Pathways and Uncertainty Prediction in FISPACT-II*. Ed. by Array. 2014. DOI: 10.1051/snamc/201402403. URL: https://fispact.ukaea.uk/wp-content/uploads/2016/07/snamc2013_02403.pdf.

[63] S. Janski. “Using Green’s Functions to Compute 3 Dimensional Neutron Flux Maps”. In: *WM2016 Conference* (2016), pp. 1–14.

[64] S. Janski. “First step in validating the radiological inventories of the current French nuclear fleet”. In: *WM2019 Conference* (2019), pp. 1–8.

[65] M. Culioli et al. “State of the art of Monte Carlo techniques for reliable activated waste evaluations”. In: *Predec 2016* (2016), pp. 2–10.

[66] M. Pantelias Garcés and B. Volmert. “Activation neutronics for a Swiss pressurized water reactor”. In: *Nuclear Technology* 192.3 (2015), pp. 278–285. ISSN: 00295450. DOI: 10.13182/NT15-13.

[67] A. Santamarina et al. *The JEFF-3.1.1 Nuclear Data Library*. 2009.

[68] Sogin. *Misure di attività specifica su un campione del rivestimento interno del recipiente a pressione della centrale elettronucleare di Trino - Valutazione dei flussi neutronici*. Tech. rep. Sogin, 1977.

[69] PSI. *TENDL-2017*. https://tendl.web.psi.ch/tendl_2017/tendl2017.html [Accessed: (05/02/2024)].

[70] IAEA. *Nuclear Data Services*. https://www-nds.iaea.org/ [Accessed: (05/02/2024)].

[71] K. I. Tanaka, J. Ueno, and S. Chiba. "Estimation of a boundary to distinguish between radioactive materials and non-radioactive materials around a Main Steam line and a Feed Water line in a Biological Shielding Wall of a BWR for decommissioning". In: *Progress in Nuclear Energy* 93 (2016), pp. 371–385. ISSN: 01491970. DOI: 10.1016/j.pnucene.2016.08.021. URL: http://dx.doi.org/10.1016/j.pnucene.2016.08.021.

[72] K. I. Tanaka and J. Ueno. "Development of a reliable estimation procedure of radioactivity inventory in a BWR plant due to neutron irradiation for decommissioning". In: *EPJ Web of Conferences* 05019.153 (2017), pp. 1–6.

[73] ENEL S.p.a. *Caratterizzazione radiologica dell'impianto: analisi radiochimiche e radiometriche di componenti attivati*. Tech. rep. ENEL, 1993.

[74] PSI. *TENDL-2019*. https://tendl.web.psi.ch/tendl_2019/tendl2019.html [Accessed: (05/02/2024)].

[75] *ARPA Piemonte*. https://www.arpa.piemonte.it/approfondimenti/temi-ambientali/radioattivita/reti-monitoraggio/copy_of_MedieGeiger2015.pdf [Accessed: (05/02/2024)].

[76] IEA. *Global Electricity Generation Mix*. https://www.iea.org/data-and-statistics/charts/global-electricity-generation-mix-2010-2020 [Accessed: (05/02/2024)].

[77] M. Laraia. *Nuclear decommissioning: Planning, execution and international experience*. Woodhead P. Woodhead Publishing Limited, 2012. ISBN: 9781845695019.

[78] P. E. O. Lainetti. "Cutting Techniques for Facilities Dismantling in Decommissioning Projects". In: *Journal of Energy and Power Engineering* 10.9 (2016). ISSN: 19348975. DOI: 10.17265/1934-8975/2016.09.001.

[79] J. M. Oddo, J. Harrington, and D. Kowalski. *Yankee Rowe Decommissioning Experience Record – Volume 1*. Tech. rep. Yankee Atomic Electric Company, 1997.

[80] K. S. Jeong et al. "Structures and elements for the decommissioning cost estimations of nuclear research reactors". In: *Annals of Nuclear Energy* 34.4 (2007), pp. 326–332. ISSN: 03064549. DOI: 10.1016/j.anucene.2007.01.005.

[81] M. Cole, S. Martin, and S. Adams. "Use of remote equipment in reactor decommissioning". In: *Proceedings of the International Conference on Radioactive Waste Management and Environmental Remediation, ICEM* 2 (2009), pp. 101–106. DOI: 10.1115/ICEM2009-16326.

[82] S. Yanagihara, S. Ashida, and H. Usui. "Dismantling of JPDR internals using underwater plasma arc cutting technique operated by robotic manipulator". In: *Journal of Nuclear Science and Technology* 25.11 (1988), pp. 891–894. ISSN: 00223131. DOI: 10.3327/jnst.25.891.

[83] R. Versemann. “Decommissioning nuclear plants: Experiences in Germany”. In: *Proceedings of Institution of Civil Engineers: Energy* 161.3 (2008), pp. 101–113. ISSN: 17514231. DOI: 10.1680/ener.2008.161.3.101.

[84] D. Krajcarz. “Comparison metal water jet cutting with laser and plasma cutting”. In: *Procedia Engineering* 69 (2014), pp. 838–843. ISSN: 18777058. DOI: 10.1016/j.proeng.2014.03.061.

[85] K. Jeong et al. “Cutting Technology for Decommissioning of the Reactor Pressure Vessels in Nuclear Power Plants”. In: *Transactions of the Korean Nuclear Society Spring Meeting* (2012), pp. 17–18.

[86] H. Bienia. “Thermal cutting technologies for decommissioning of nuclear facilities”. In: *Proceedings of the International Conference on Radioactive Waste Management and Environmental Remediation, ICEM* 2 (2009), pp. 353–360. DOI: 10.1115/ICEM2009-16297.

[87] P. Hilton and A. Khan. “The Potential of Laser Cutting and Snake Arm Robots in Aspects of Nuclear Decommissioning”. In: *The Review of Laser Engineering* 41.11 (2013), p. 911. ISSN: 0387-0200. DOI: 10.2184/lsj.41.11_911.

[88] J. S. Shin et al. “High-speed fiber laser cutting of thick stainless steel for dismantling tasks”. In: *Optics and Laser Technology* 94 (2017), pp. 244–247. ISSN: 00303992. DOI: 10.1016/j.optlastec.2017.03.040.

[89] J. S. Shin et al. “Underwater cutting of 50 and 60 mm thick stainless steel plates using a 6-kW fiber laser for dismantling nuclear facilities”. In: *Optics and Laser Technology* 115 (2019), pp. 1–8. ISSN: 00303992. DOI: 10.1016/j.optlastec.2019.02.005.

[90] K. H. Ho and S. T. Newman. “State of the art electrical discharge machining (EDM)”. In: *International Journal of Machine Tools and Manufacture* 43.13 (2003), pp. 1287–1300. ISSN: 08906955. DOI: 10.1016/S0890-6955(03)00162-7.

[91] A. Watanabe and H. Yokoi. “Aerosol, Gas, and Swarf Production during Underwater Cutting of Reactor Core Internals Using Electron Discharge Machining”. In: *Journal of Nuclear Science and Technology* 44.10 (2007), pp. 1317–1323. ISSN: 0022-3131. DOI: 10.1080/18811248.2007.9711377.

[92] M. Ishikawa, M. Kawasaki, and M. Yokota. “JPDR decommissioning program—plan and experience”. In: *Nuclear Engineering and Design* (1990).

[93] G. R. Lee et al. “Selection methodology of the optimal cutting technology for dismantling of components in nuclear power plants”. In: *Annals of Nuclear Energy* 166 (2022). ISSN: 18732100. DOI: 10.1016/j.anucene.2021.108808.

[94] D. Y. Mun and Y. T. Cho. “A Short Review on the Mechanical and Thermal Processes for Underwater Cutting of Metal Structures”. In: *Journal of the Korean Society of Manufacturing Process Engineers* 19.1 (2020), pp. 121–133. ISSN: 1598-6721. DOI: 10.14775/ksmpe.2020.19.01.121.

[95] G. R. Lee, B. J. Lim, and C. D. Park. “Evaluation of metal cutting technologies for decommissioning of nuclear power plants.” In: *Transactions of the Korean Nuclear Society* (2019). URL: https://www.kns.org/files/pre_paper/41/19S-510-%EC%9D%B4%EA%B0%80%EB%9E%8C.pdf.

[96] European Commission’s Research and Technological Development. *Dismantling Techniques , Decontamination Techniques , Dissemination of Best Practice , Experience and Know-how*. 2009.

[97] L. Bonavigo and M. De Salve. “Issues for Nuclear Power Plants Steam Generators”. In: *Steam Generator Systems: Operational Reliability and Efficiency* (2011). DOI: 10.5772/14853.

[98] L. Cao et al. “Research on underwater diamond wire saw”. In: *2006 IEEE International Conference on Mechatronics and Automation, ICMA 2006* 2006 (2006), pp. 1695–1700. DOI: 10.1109/ICMA.2006.257452.

[99] J. S. Shin et al. “Underwater laser cutting of stainless steel up to 100 mm thick for dismantling application in nuclear power plants”. In: *Annals of Nuclear Energy* 147 (2020). ISSN: 18732100. DOI: 10.1016/j.anucene.2020.107655.

[100] M. Tezuka. “Lessons-learned from ongoing decommissioning project of Fugen NPS”. In: *Proceedings of the Workshop on Current and Emerging methods for Optimising Safety and Efficiency in Nuclear Decommissioning* (2017).

[101] A. Khan and P. Hilton. “Optimisation of underwater laser cutting for decommissioning purposes”. In: *International Congress on Applications of Lasers & Electro-Optics* (2014), pp. 294–302. DOI: 10.2351/1.5063072.

[102] IAEA. *Decommissioning of nuclear installations at CIEMAT*. https://inis.iaea.org/collection/NCLCollectionStore/_Public/33/020/33020082.pdf [Accessed: (05/02/2024)].

[103] M. Laraia. “Nuclear Decommissioning: Its History, Development, and Current Status”. In: *Concrete (London)*. Vol. 24. Springer, 2018, p. 127. ISBN: 9783319759159.

[104] R. Borchardt et al. “Remote handling techniques in decommissioning - A report of the NEA Co-operative Programme on Decommissioning (CPD) project”. In: *Nea-Rwm-R–2011-2* (2011).

[105] K. Tamura, R. Ishigami, and R. Yamagishi. “Laser cutting of thick steel plates and simulated steel components using a 30 kW fiber laser”. In: *Journal of Nuclear Science and Technology* 53.6 (2016), pp. 916–920. ISSN: 00223131. DOI: 10.1080/00223131.2015.1080633.

Appendix A

Development of a methodology to select the best cutting technique considering site specific requirements

This activity has been performed in collaboration with M. Troise, from the Department of Mechanical and Aerospace Engineering (DIMEAS).

A.1 Introduction

As previously discussed in this Thesis, nuclear energy constitutes a significant contributor to low-carbon power generation, accounting for approximately 10% of global electricity supply [76]. Presently, there are 413 operational nuclear power reactors, with a substantial proportion (approximately 65%) constructed prior to 1990 [2]. Around 200 reactors are permanently decommissioned [2], and numerous reactors are approaching the conclusion of their operational lifespan. This aging phenomenon highlights the need to address decommissioning activities, particularly in nations that embraced early investments in nuclear power and are currently managing older reactor facilities, such as Italy itself.

With specific reference to the prevalent PWRs, dismantling efforts are confronted by significant challenges, notably in disassembling complex components of the primary cooling circuit and the reactor itself. These components encompass the

RPV, RVI, bioshield, steam generators, pumps, pressurizer, and connecting pipes. While radioactive contamination potentially extends across all these components, structural material activation is confined to the RPV, RVIs, and the concrete bioshield around the core. The dismantling of these elements is particularly intricate due to a combination of factors, including robust steel/concrete structures and the presence of hazardous radioactive environments necessitating the application of remote technologies. The restricted working space, specially in the reactor pit, further adds to these challenges.

Two principal strategies for dismantling are conventionally considered: dry cutting, involving component segmentation in a dry environment, typically air; and wet cutting, entailing underwater segmentation. Dry cutting is generally faster but less effective in controlling radiation spreading aerosols and managing secondary waste. Conversely, wet cutting, though comparatively slower and necessitating more complex setups such as a flooded reactor pool and remote handling of cutting tools, offers advantages in contamination control and radiation exposure mitigation, due to water's efficacy as a gamma-ray shield. Both strategies, coupled with thermal and mechanical cutting technologies, have demonstrated effectiveness in various applications [77], [78].

Several cutting techniques, predominantly relying on mechanical forces or localized energy concentration, such as saws, grinding tools, flame, or plasma cutting, have been successfully deployed in nuclear plant decommissioning. Each technique presents distinct advantages and drawbacks. Mechanical tools like bandsaws and disc saws, while cost-effective and suitable to remote and underwater operation, exhibit limitations in cutting speed and necessitate periodic maintenance. Conversely, flame and plasma cutting are faster but pose challenges in underwater application due to contamination control and shielding issues. Section A.2 will delve deeper into the details of these cutting technologies.

To select the most suitable cutting technology for a given decommissioning project, a comprehensive evaluation incorporating multiple parameters is indispensable. A trade-off matrix, assigning scores based on individual characteristics (e.g., cutting speed, secondary waste production), facilitates a direct comparison between technologies. However, this approach alone is not sufficient, as it neglects site-specific requirements, which frequently serve as primary constraints.

Nuclear plants exhibit considerable heterogeneity. Even considering LWRs alone there could be significant differences, in particular because at the beginning of the civilian nuclear era reactor designs were not standardized. Variations in nuclear island layouts significantly impact decommissioning planning, influencing, for example, the availability of working space for cutting stations and part movement. Notable instances, such as the decommissioning of the José Cabrera NPP in Spain [17], which required the controlled demolition of a concrete wall to allow segmentation procedures to be performed in the spent fuel pool, highlight the significance of evaluating working space when selecting a cutting technology.

Moreover, plant-specific factors, including material composition and maximum thickness, influence the choice of cutting technology. For instance, variations in nominal power impact the size and thickness of RPVs, affecting the feasibility of cutting. Material composition, particularly the concentration of ^{59}Co in steel, is crucial, as its transmutation into the gamma-emitting ^{60}Co significantly influences steel activation, as extensively discussed in Chapters 3 and 4. The resultant gamma radiation field dictates the necessity for remote or underwater activities, aligning with the ALARA principle, which requires all exposure to workers to be as low as reasonably achievable. The best cutting technology depends on the overall activation distribution as well, which itself depends on the operating history of the reactor, another site-specific parameter.

Additional considerations encompass the regulatory framework and overall cost, contingent on both cutting tools and dismantling strategy. Regulatory constraints play a significant role in shaping the decommissioning approach, as exemplified by the removal of entire RPVs in the decommissioning of reactors like Big Rock Point and Yankee Rowe in the United States [77], [79]. The choice between single-piece removal and segmentation depends on regulatory approval and the availability of a suitable radioactive waste repository, which is able to receive the waste package.

These particular local conditions underscore the inherent multiparameter nature of selecting a cutting technique for decommissioning. A trade-off analysis must encompass technology attributes, local regulations, plant-specific characteristics, and the interplay of these factors in developing an effective decommissioning strategy. Consequently, the identification of a singular optimal cutting technology and a standardized dismantling plan applicable to all NPPs proves exceedingly challenging, if not practically unattainable.

A.2 Cutting procedures

Decommissioning activities necessitate a diverse array of dismantling tasks performed through various techniques. Central to the dimsantling of nuclear reactors is the segmentation of metal components, including reactor vessels, tanks, piping, and other parts. Segmentation operations, constituting 64% of the dismantling timeline [80], are conducted through mechanical and thermal cutting methodologies. Mechanical cutting often involves the utilization of grinders, saws and drilling machines to progressively remove metal chips from the segmented component until it separates in two. Other tools, such as shears and cutters, operate on thin metal slabs similarly to a pair of scissor on a piece of paper, separating the component. Thermal cutting technologies instead use high temperatures to melt the material and blow it away from the part being cut, and are powered either by flammable gases (e.g. oxy-fuel torch), by electrical power (e.g. plasma torch, laser) or in some rare cases by a chemical reaction (e.g. thermal lance). Techniques based on the generation of an electric arc (e.g. contact arc metal cutting) are usually referred to separately as electrical cutting techniques. The careful selection of the most suitable method is contingent upon specific application requirements, demanding a detailed consideration of various factors in the decision-making process.

A prevalent approach involves the adaptation of industrial manufacturing techniques to meet the distinctive demands of decommissioning nuclear installations, including aspects such as remote applicability, enhanced process safety, emissions reduction, and underwater applicability. Nevertheless, unique site-specific requirements may need the development of specialized cutting techniques [81]. Several techniques can be employed independently or in conjunction, tailored to the specific demands of the decommissioning project. However, it is noteworthy that fumes and bubbles produced by thermal processes can compromise the shielding effectiveness provided by water, if wet cutting is the chosen methodology.

This study identifies eleven cutting technologies, categorized into mechanical, thermal and electrical, as methodologies that proved effective in decommissioning activities. The considered cutting technologies are listed in Table A.1. Given the diverse nature of target objects and operational conditions, the cutting processes for NPPs often necessitate a suitable combination of multiple cutting technologies. The segmentation strategy must account for waste package volume, payload, and radioactivity limits, with the aim of selecting an optimal cutting size that minimizes

Mechanical cutting	Thermal cutting	Electrical cutting
Saws	Plasma	CAMC[1]
Shears	Oxy-fuel	EDM[2]
Nibbles	Laser	ASC[3]
DW[4]		
AWJ[5]		

Table A.1 Cutting techniques for the decommissioning of NPPs.

both overall costs and cutting duration. Additionally, the spatial requirements for technical equipment must be considered, as previously mentioned.

The implementation of cutting technologies mandates the adoption of stringent safety measures and precautions, considering the inherent dangers associated with decommissioning a nuclear power plant, involving the handling of hazardous materials and the utilization of specialized equipment. Rigorous adherence to proper training and safety protocols is important to ensure the well-being of workers and the broader public. The subsequent Sections delve into a comprehensive examination of the advantages and drawbacks associated with the technologies outlined in Table A.1.

A.2.1 Mechanical cutting technologies

Mechanical cutting techniques employ specialized tools with the required mechanical strength and hardness to facilitate the segmentation of objects. In the context of decommissioning projects, shears, nibblers, saws, diamond wire, and abrasive water jets are commonly employed for mechanical cutting. These methods involve the separation of objects into distinct parts, achieved through mechanisms such as shearing or the gradual removal of metal fragments using saws, abrasive wires, or pressurized water jets. Unlike thermal techniques, mechanical methods generate substantial reaction forces throughout the segmentation process, needing robust support structures to control vibrations. Additionally, owing to their reliance on phys-

---

[1] Contact Arc Metal Cutting
[2] Electrical Discharge Machine
[3] Arc Saw Cutting
[4] Diamond Wire
[5] Abrasive Water Jet

ical contact, it is necessary to consider that possibly the cutting tool will encounter obstructions or break during operations, and maintenance has therefore a significant role in allowing cutting procedures to proceed smoothly.

Mechanical nibblers are employed for cutting metal slabs and tanks, they are light and capable of cutting 5 mm thick stainless steel at a speed of 1 m/min [78], with the generation of minimal aerosols. Shears, functioning through shear force, are useful in cutting metal sheets, with hydraulic variants capable of cutting piping up to 300 mm in diameter and 5 mm wall thickness. Saws, utilizing mechanical friction through rotational or reciprocating motion, find effective application in decommissioning, especially large stationary saws that can cut metal up to a thickness of 60 cm, achieving a maximum cutting speed of approximately 100 cm^2/min [78]. Diamond wire saws offer a viable cutting method as well, but demand significant working space. Due to their weight, these cutting machines necessitate mounting on a guide for support, and the dust generated during abrasive cutting is mitigated by water, preventing the dispersion of contaminants. The versatility of the diamond wire is demonstrated in applications such as offshore endeavors (e.g. oil and gas industry) up to 60 meters of water depth and in murky water conditions [80]. This technology is suitable for both metal and concrete cutting, and proved effective at handling structures with substantial thickness.

Abrasive Water Jet (AWJ) cutting involves the acceleration of abrasive particles by water, which carries them to the material that has to be cut. The generation mechanisms of abrasive suspension jets and the influence of key parameters on cutting efficiency are available in literature, such as in [81]. Originating from the steel industry, AWJ technology has been adapted for decommissioning applications, with early underwater internals reactor segmentation applications performed at the Elk River Reactor in Minnesota [77].

A.2.2 Thermal cutting technologies

Primary thermal cutting technologies employed for decommissioning purposes include plasma cutting, oxy-fuel cutting, and laser cutting. These techniques take advantage of concentrated thermal energy to cut a workpiece without direct contact with the tool. The absence of reaction forces facilitates the segmentation of components with considerable thickness, such as the RPV. Thermal cutting involves the removal of material by melting it at high temperatures and subsequently removing it from the working zone with a high-pressure gas stream. This process results in the generation of aerosol particles, dust, and fumes, which require the implementation of suitable filter systems to safeguard workers. Nevertheless, when thermal cutting is performed underwater, the airborne particle generation diminishes significantly, by at least three orders of magnitude [77]. It is worth noting that while the presence of water reduces airborne particles, water turbidity increases, preventing a clear view of the cutting process.

Plasma cutting has demonstrated successful applications in decommissioning projects [82], particularly for the segmentation of reactor internals in NPPs [83] with thickness ranging from 50 mm to 150 mm [84]. For any reader interested in more details about this technology, a comprehensive overview of typical gas emissions is provided in [85], and the required equipment is detailed in [86].

Laser cutting, a well-established industrial technology, is witnessing a growing trend in its application within the framework of NPP decommissioning [87]. Numerous studies have analysed the characteristics of laser technology in terms of power, laser type, materials and thickness to be cut [88], [89]. However, despite its industrial familiarity, further development is required to effectively apply laser technology in decommissioning operations, as many process parameters still need further research.

Oxy-fuel cutting, versatile for use in both dry and underwater conditions, is characterised high cutting speed. Widely adopted in various industries, this well-known technology features relatively small and economical tools when compared to alternative cutting techniques [85]. However, it is noteworthy to acknowledge that oxy-fuel cutting produces more dross than plasma and laser technologies and requires to work with flammable gases.

A.2.3 Electrical cutting technologies

Electrical cutting technologies involve establishing an electric arc between the cutting tool and the workpiece, the cutting object has therefore to be composed of conductive material. Notably, the non-contact cutting action between the electrode and the workpiece permits the segmentation of hard materials. The primary electrical cutting technologies encompass Electrical Discharge Machining (EDM), Contact Arc Metal Cutting (CAMC), and Arc Saw Cutting (ASC). To a certain extent, plasma cutting could be considered an electrical cutting technology as well, although it is typically grouped with the thermal ones, since it has been employed for much longer and more extensively than the others which are somehow newer.

CAMC employs an irregularly occurring arc between an electrode and the workpiece to perform the cut. Operating at low voltage and high current, this process is limited to cutting electrically conductive materials, but can be employed underwater. Successfully applied in decommissioning projects, CAMC technology enables to cut components up to 260 mm in thickness [83] using appropriate equipment [86].

EDM, as an electrical cutting process, has found extensive application in non-conventional materials removal processes. For any interested reader, an in depth discussion on the state-of-the-art of EDM is presented in [90]. EDM exhibits a slower cutting speed compared to mechanical and thermal technologies, with a material removal rate typically ranging from 2 to 400 mm^3/min. For this reason, it is typically used for small, precise cuts rather than for complete segmentation of massive components. It generates aerosols and particulate during operations [91].

ASC closely resembles CAMC, differing primarily in the electrode, which is a rotating metal disc rather than a fixed blade. With blade speeds ranging between 300 and 1800 rpm, this technique facilitates the removal of molten metal and electrode cooling. The blade diameter influences the maximum cutting thickness, with a 1 m blade capable of cutting through 30 cm of metal. ASC has proven successful in the segmentation of the Japan Power Demonstration Reactor [92].

A.3 Selection methodology

Comparing cutting technologies for the decommissioning of NPPs is a multiparameter process that relies on collecting data dispersed across various sources. Additionally, the selection of the optimal cutting technology for a decommissioning project has to consider several key factors:

- **Safety**: The decommissioning of a NPP necessitates cutting technologies that minimize the risk of accidents, injuries and radiation exposure to workers;
- **Efficiency**: Optimal cutting technologies should accelerate the decommissioning process, minimizing costs and downtime;

- **Accuracy**: To ensure the safe and effective execution of the dismantling process, the chosen cutting technology must be sufficiently precise;
- **Environmental Impact**: Consideration should be given to the environmental impact of the cutting technology, encompassing potential emissions or waste byproducts that may be generated (known secondary waste);
- **Cost**: The cost of the cutting technology is a significant factor, as decommissioning a NPP is inherently an expensive undertaking.

A comprehensive evaluation of the advantages and drawbacks of each option, coupled with an analysis of site-specific requirements, is necessary to determine the optimal cutting technology tailored to the unique demands of a specific decommissioning project.

A.3.1 Comparison model for the cutting technology

Numerous works have tried to extract performance data on cutting technologies from literature [83], [84]. However, the approach of most of these works to these data is limited, with some merely comparing few parameters, such as workable thickness and material, cutting speed, and secondary waste generation [93]. This study, in contrast, provides a more comprehensive comparison of cutting technologies, considering more key performance data including safety, cutting speed, quality of cut plane, remote control capability, underwater operation performance, cost, ease of work, and secondary waste generation. Additionally, site-specific requirements like thickness, material, and working space are introduced and discussed.

The performance data gathered from literature for each group of cutting technology are presented in Tables A.2, A.3 and A.4. These data, however, are qualitative in nature, using definitions such as "high", "average (mid)", "good" or "low", making direct comparisons challenging. To address this, an in depth analysis of the literature was undertaken, drawing insights from various works comparing cutting technologies [77], [86], [94]. The qualitative performance data were then converted into quantitative values, quantified on a ten-point scale, and reported in Tables A.5, A.6 and A.7.

To facilitate the comparison, cutting technologies were assessed by assigning weights to each performance factor. These project-specific weights are determined by

	Safety	Underwater operation	Speed	Cut quality
Shears	High	Yes (High)	Mid	Good
Nibbler	High	Yes (High)	Mid	Good
Saws	Good	Yes (High)	Good	Good
DW	Mid	Yes (Mid)	Mid	Mid
AWJ	Mid	Yes (Mid)	Mid	High
	Remote control	Secondary waste	Cost	Ease of use
Shears	High	Low	Low	High
Nibbler	Good/High	Low	Low	High
Saws	High	Low	Mid/Low	High
DW	Good/High	Mid	High	Low
AWJ	Good	High	High	Mid/Low

Table A.2 Qualitative performance data for mechanical cutting techniques. Data from [78], [95], [96], [84], [97], [98].

	Safety	Underwater operation	Speed	Cut quality
Plasma	Good	Yes (Good)	High	Good
Laser	Good	Yes (Mid)	High	High
Oxy-fuel	Mid	Yes (Good)	High	Low
	Remote control	Secondary waste	Cost	Ease of use
Plasma	High	Mid	Mid	Good
Laser	Good	Low/Mid	High	Good
Oxy-fuel	Good/High	Mid	Mid	Mid

Table A.3 Qualitative performance data for thermal cutting techniques. Data from [86], [99], [93], [100], [77], [101], [96].

an expert team based on site and project requirements, encompassing considerations such as safety laws and available time. After assigning values to all technologies across performance factors, the weighted scores were calculated by multiplying the assigned ratings by their respective weights and summing them up. The mathematical model for selecting optimal cutting technologies is therefore expressed through the following equations:

$$\mathbf{T} = (t_{i,j}) \,\Big|_{\substack{i=1:n \\ j=1:m}} \tag{A.1}$$

	Safety	Underwater operation	Speed	Cut quality
CAMC	Good	Yes (Only)	Good	Mid
EDM	Good	Yes (Mid)	Low	High
ASC	Good	Yes (Mid)	Good	High
	Remote control	**Secondary waste**	**Cost**	**Ease of use**
CAMC	Good/High	Mid	Mid/High	Mid
EDM	Good	Mid	Mid/High	Low
ASC	Good	Mid	Mid/High	Mid

Table A.4 Qualitative performance data for electrical cutting techniques. Data from [86], [102], [94], [103], [95], [104].

	Safety	Underwater operation	Speed	Cut quality
Shears	10	8	6	8
Nibbler	10	8	6	8
Saws	8	8	7	7
DW	6	5	4	5
AWJ	6	5	3	8
	Remote control	**Secondary waste**	**Cost**	**Ease of use**
Shears	10	10	10	10
Nibbler	9	10	10	10
Saws	10	8	8	10
DW	8	6	3	4
AWJ	7	2	2	5

Table A.5 Quantitative performance data for mechanical cutting techniques.

$$w = \{w_1, \dots, w_i, \dots, w_n\}^T \tag{A.2}$$

$$\mathbf{T} \cdot w = p \tag{A.3}$$

$$p = \{p_1, \dots, p_i, \dots, p_n\}^T \tag{A.4}$$

where $t_(i, j)$ represents the value assigned to a specific cutting technology for a particular evaluation parameter. The values were then gathered into a matrix

	Safety	Underwater operation	Speed	Cut quality	Remote control	Secondary waste	Cost	Ease of use
Plasma	8	7	9	8	10	6	6	8
Laser	8	5	10	10	8	8	4	8
Oxy-fuel	6	7	8	4	9	4	7	6

Table A.6 Quantitative performance data for thermal cutting techniques.

	Safety	Underwater operation	Speed	Cut quality	Remote control	Secondary waste	Cost	Ease of use
CAMC	8	10	7	7	9	4	5	6
EDM	8	6	2	9	8	4	5	9
ASC	8	6	7	10	8	7	5	6

Table A.7 Quantitative performance data for electrical cutting techniques.

named **T**. Here, n denotes the number of cutting technologies, m is the number of performance parameters, w is the weights vector of performance factors for cutting technologies, and the p_i elements of vector p represents the weighted average values of the cutting technologies.

This methodology aligns with approaches described in previous works [93] but incorporates a more extensive range of performance factors, thereby enabling a more accurate and comprehensive comparison. Utilizing this approach allows the derivation of a ranking for cutting technologies.

A.3.2 Site-specific requirements

The identification of the most suitable cutting technology for NPP decommissioning must incorporate site-specific requirements and constraints. Additionally, the overall cost of each potential technology should align with the planned budget. The chosen parameters for evaluating site constraints and project requirements include workable materials and thickness, commercialization readiness, and required space, with typical values provided in Table A.8.

	Thickness [mm]	Readiness	Material	Volume required
Shears	<10	Yes	Metal	Low
Nibbler	<5	Yes	Metal	Low
Saws	<300	Yes	Metal	Mid
DW (metal)	<300	Yes	Metal	High
DW (concrete)	<950	Yes	Concrete	High
AWJ (metal)	<300	Yes	Metal	Low
AWJ (concrete)	<500	Yes	Concrete	Low
Plasma (air)	<160	Yes	Metal	Mid
Plasma (UW)	<100	Yes	Metal	Mid
Laser (air)	<300	No	Metal	Low
Laser (UW)	<100	No	Metal	Low
Oxy-fuel	25-350	Yes	Carbon steel	Low
CAMC	<300	Yes	Metal	Low
EDM	<50	No	Metal	Mid
ASC	<300	Yes	Metal	Mid

Table A.8 Parameters for the evaluation of site-specific requirements. UW stands for "Under Water". Data from [78], [86], [105], [99], [77].

Determining overall costs requires a detailed analysis, and for this reason it is beyond the scope of this work. In this case as well, given the lack of detailed volume descriptions in decommissioning projects, qualitative values have been employed from the state-of-the-art to facilitate technology comparisons. These qualitative values suggest the volume required in the proximity of the target structure.

In the second part of the mathematical model, values of 1 and 0 are assigned to each technology based on their adherence to site requirements: 1 if they comply, 0 if they do not. Cost is treated slightly differently, as a value of 0.5 is assigned when overall costs exceed the budget, recognizing the potential for budget adjustments. This step essentially generates a set of applicability factors for each cutting technology: either they comply and can be used or not (e.g. there would be no point in trying to cut concrete with an oxy-fuel torch). This factor therefore determines the technology's applicability to specific decommissioning projects, and the technology can be deemed suitable if the value is either 1 or 0.5. However, in the latter case, an increase in the overall budget is necessary.

The following equations outline this selection process:

$$\mathbf{S} = (s_{i,j}) \mid_{\substack{i=1:n \\ j=1:m}} \tag{A.5}$$

$$a_i = \prod_{j=1}^{m} s_{i,j} \tag{A.6}$$

$$\mathbf{A} = diag(a_1, \ldots, a_n) \tag{A.7}$$

where $s_(i,j)$ represents the mathematical value of each parameter, m is the number of parameters considered, n is the number of cutting technologies, a_i is the applicability factor and **A** is the applicability matrix of all cutting technologies (a diagonal matrix). Finally, the weighted average values of cutting technologies in the vector p, obtained from the comparison methodology, are multiplied by their applicability factor, excluding technologies with zero scores.

$$\mathbf{A} \cdot p = \tau \tag{A.8}$$

$$\tau_i = a_i \cdot p_i \tag{A.9}$$

τ is the score vector of cutting technologies, considering both their performances and site requirements.

A.3.3 Case study: segmentation of an RPV

The optimal cutting technology for RPV with a thickness range of 200-250 mm and an internal stainless steel thickness of 10 mm can be determined using the methodology outlined in Subsections A.3.1 and A.3.2. In this specific case, the cutting process will be conducted underwater. The performance factors considered include safety, cutting speed, cut quality, remote control capability, underwater operation performance, cost, ease of work, and secondary waste generation. The weightings assigned to these performance factors are 0.1, 0.1, 0.02, 0.18, 0.18, 0.04, 0.18, and 0.2, respectively, highlighting the typical greater importance of parameters such as capability of working underwater remotely and secondary waste production.

In this example, the available space around the RPV is constrained, and the cost of technologies adheres to the assumed budget. Subsequently, the weighted average values of cutting technologies are multiplied by their applicability factors, and the resulting scores represent the remaining technologies, as outlined in Table A.9.

Cutting techniques	Weighted scores	Applicability factors	Final scores
Shears	9.36	0	0
Nibbler	9.18	0	0
Saws	8.56	1	8.56
DW	5.10	1	5.10
AWJ	5.30	1	5.30
Plasma	7.84	0	0
Laser	7.38	0	0
Oxy-fuel	6.42	1	6.42
CAMC	7.08	1	7.08
EDM	7.36	0	0
ASC	7.16	1	7.16

Table A.9 Weighted and final scores of selected cutting techniques.

It is necessary to note that these results are contingent on the chosen weights for performance factors, and different weight selections may yield varied conclusions. However, the current results indicate that saws, ASC, CAMC and oxy-fuel are valid solutions, with saws emerging as the most favorable choice based on these weight factors. The final scores of the considered techniques can sometimes be quite close: this is essentially due to the fact that all of them proved effective and are therefore valid choices, although maybe not optimal.

A.4 Results and discussion

The applicability of a technology concerning site-specific parameters serves as a significant limiting factor in determining the optimal choice. For instance, hydraulic shears may initially seem to be the preferred technique for several reasons: they are cheap, quick, user-friendly, applicable remotely and underwater, generate minimal secondary waste, and pose no safety hazards related to flames, fumes, or intense electrical currents. However, their applicability is severely constrained by the maximum thickness they can cut. Clearly, using shears for cutting the wall of a RPV or even the few centimeters of core plates or primary circuit pipes, is unfeasible. Consequently, they are limited to specific operations, such as the segmentation of guide tubes and relatively thin components. If other tools are necessary for more challenging tasks, like RPV segmentation with a disk saw, installing an additional cutting tool may not be practical or economical, especially if the saw can also handle thin components. Minimizing the number of tools required for dismantling is an industry best practice, reducing the final cost of the decommissioning project by requiring fewer machinery, resulting in less tool decontamination and material movement in and out of the containment building.

The available working space, in particular, can significantly curtail the applicability of certain technologies, as some machinery may be large and heavy or necessitate complex configurations. For instance, if the reactor pool is too small for a stationary cutting station, cutting tools might need installation directly inside the RPV in the reactor pit. However, this might rule out oxy-fuel cutting, as the RPV's internal liner, typically made of stainless steel, cannot be directly cut by flame due to its low iron content compared to carbon steel. While oxy-fuel cutting from the outside is generally feasible, it might not be possible if space constraints prevent the RPV from being moved from the pit.

External factors also play a role in the final choice. If a company has significant operational experience with a specific technology, such as bandsaws, it is likely to opt for that technology over others, even if they might score higher. This preference is especially true if the results of the comparisons are closely aligned, which is often the case. Both thermal and mechanical techniques have proven effective in dismantling operations, and their drawbacks are often compensated by their advantages. For instance, controlling contamination is more challenging with flame or plasma cutting, both in air and underwater. However, their faster operation might be preferred if time is a critical factor due to regulatory deadlines. Conversely, if worker safety takes precedence, saws may be favored due to their excellent radiation shielding underwater, even if progress is significantly slower.

A.5 Conclusions and perspective

An engineering-oriented approach has been employed to formulate and refine a systematic procedure for comparing technologies applicable to the decommissioning of NPPs. This methodology can be effectively employed in specific test cases of interest, considering the specific attributes of the NPP site under investigation to enhance the decision-making process for dismantling operations. It enables the integration of technology characteristics with strict applicability criteria, contingent on the analyzed NPP. The methodology is designed to account for the cost of various options, although this work refrains from conducting a detailed economic analysis as the cost depends on the specific NPP under consideration.

In essence, the methodology serves as a supportive tool for stakeholders involved in developing a decommissioning plan. The ultimate determination of weight performance factors for the decommissioning of a specific NPP is also influenced by regulations or the operational experience of potential contractors with a particular technology. All stakeholders are therefore involved in the decision process.

Future works include expanding this topic further, particularly through the application of this methodology to real-world test case scenarios. Additionally, discussions will explore the feasibility of segmenting the RPV from both inside and outside, contingent on the available working space in close proximity to the reactor.

Appendix B

AISI 304 composition

In this Appendix the detailed reference composition of the AISI 304 stainless steel used in the framework of this Thesis is reported. This data was provided by Sogin [27]. The unit of measurement of the concentrations is mg/kg (ppm), except for some trace elements, flagged with *, that are expressed in μg/kg (ppb). Source for the data is a combination of activation analysis (A), material certifications from the producer (C) and literature review (L). (D) is only used for iron the dominant element.

Table B.1 AISI 304 detailed composition [27]. Unit is mg/kg (ppm) unless flagged with *, in that case unit is μg/kg (ppb).

Element	Concentration	Source	Element	Concentration	Source
Ag*	10.7	A	Na	4.0	L
Al	200.0	L	Nb	6.0	L
As	120.0	A	Nd*	5.9	A
Au*	2.1	A	Ni	95000.0	C
Ba	10.0	A	Os*	8.8	A
Br	1.4	L	P	245.0	C
C	528.0	C	Pb	118.0	L
Ce*	11.4	A	Pt*	45.8	A
Cl	60.0	L	Rb	65.8	A
Co	614.4	A	S	100.0	C
Cr	213300.0	A	Sb	32.5	A
Cs	7.3	A	Sc	0.2	A
Cu	987.0	A	Se	0.2	A

Table B.1 AISI 304 detailed composition [27]. Unit is mg/kg (ppm) unless flagged with *, in that case unit is μg/kg (ppb).

Element	Concentration	Source	Element	Concentration	Source
Eu*	0.9	A	Si	452.5	C
Fe	666217.2	D	Sm	0.3	A
Ga	74.0	L	Sn	524.0	A
Gd	0.2	A	Ta	23.4	A
Hf	11.9	A	Tb*	51.2	A
Ho*	1.0	A	Th*	32.5	A
Ir*	20.1	A	Ti	1000.0	L
K	678.0	A	U	1.2	A
La*	6.2	A	V	280.0	L
Li	0.1	L	W	11.2	A
Lu*	2.0	A	Yb	0.3	A
Mn	15450.0	C	Zn	256.0	A
Mo	21.3	A	Zr	3400.0	A